Ab initio description of transport in nanostructures including electron-phonon coupling

Ab initio Beschreibung von Transport in Nanostrukturen unter Berücksichtigung der Elektron-Phonon-Wechselwirkung

Dissertation

submitted for the degree of

Doctor rerum naturalium
Doktor der Naturwissenschaften

by

Carsten Eberhard Mahr

Supervisor: Prof. Dr. Christian Heiliger
AG Theoretische Festkörperphysik

JUSTUS-LIEBIG-
UNIVERSITÄT
GIESSEN

Institut für Theoretische Physik
Justus-Liebig-Universität Gießen

Gießen, February 2018

Contents

1. Introduction **1**

2. Theory **5**

2.1. Electronic Structure 6

2.1.1. Green's Functions 7

2.1.2. Korringa-Kohn-Rostoker Formalism 12

2.2. Electronic Transport 16

2.2.1. Non-equilibrium Green's Function Formalism 16

2.2.2. Phase-breaking Scattering Events 19

2.2.3. KKR Representation 22

2.3. Electron-phonon Coupling 29

2.3.1. Lattice Dynamics 29

2.3.2. Self-energy Formulae 30

2.3.3. Evaluation from First Principles 39

2.3.4. Wave-vector Averaging 42

2.4. Thermal Expansion 44

2.4.1. Equation of State 44

2.4.2. True Coefficient of Thermal Expansion 46

2.4.3. Evaluation in the Debye Model 47

3. Calculations **49**

3.1. Resistivity of Copper 50

3.1.1. Thermal Expansion 50

3.1.2. Electronic Structure 51

3.1.3. Phonon Dispersion 56

3.1.4. Electron Linewidth 57

3.1.5. Transmission and Resistivity 61

3.2. Resistivity of Aluminum 67

3.2.1. Thermal Expansion 67

3.2.2. Electronic Structure 67

3.2.3. Phonon Dispersion 70

3.2.4. Electron Linewidth 71

3.2.5. Temperature-dependent Resistivity 73

3.3. Temperature Characteristics of Fe/MgO Double Barrier Structures . 78

3.3.1. Fe/MgO Interface and Single Barrier Structure 79

3.3.2. Resonant Tunneling in Fe/MgO Double Barriers 82

3.3.3. Electron-phonon Self-energy Approximation 87
3.3.4. Effects of Temperature on the Electronic Transport 90

4. Summary and Outlook **97**

A. Theoretical Supplementary **101**
A.1. Sum Rule for the Spherical Bessel Function 101
A.2. Lippmann-Schwinger Equation for Self-Energies 102
A.3. Numerical Evaluation of the Transition Operator 103
A.4. Resistance in the Limit of Vanishing Bias Voltage 104
A.5. NEGF in a Multiple Terminal Setup 106
A.6. Derivation of Effective Transmission Formulae 107

Bibliography **111**

List of Publications **121**

Acknowledgements **123**

1. Introduction

Since the rise of integrated circuits, the number of transistors per chip has roughly doubled every two years. This observation was coined by Moore [1] in 1975, revising his even more optimistic prediction expressed ten years earlier [2]. It is exactly this exponential behavior that has driven the tremendous advance of all kinds of electronic devices in our everyday lives, as this miniaturization process does not only increase the performance, but simultaneously reduces the power consumption of computer chips.[1] Modern central processing units (CPUs) nowadays rely on a 14 nm technology,[2] and extrapolating the history of transistor shrinkage[3] it is reasonable to assume that another innovation may lead to even smaller devices.

Besides miniaturization, the capabilities of modern electronic devices have been even further improved by the exploitation of previously neglected degrees of freedom, most notably the electronic spin. A very intriguing feature displayed by ferromagnet/insulator magnetic tunnel junctions (MTJs) is the so-called tunnel magnetoresistance (TMR) [3–5]: Depending on whether the magnetic moments in the ferromagnetic electrodes are aligned parallel (p) or antiparallel (ap), the MTJ exhibits very different conductances $G_{\mathrm{ap/p}}$, which may be interpreted as the values 0 and 1 answering to one bit of data. Consequently, such MTJs lend themselves for interesting applications like read/write heads of modern hard drives or magnetic random access memories (MRAMs) [6, 7]. For high efficiencies of such devices it proves essential that the TMR ratio

$$\mathrm{TMR} = \frac{G_{\mathrm{p}} - G_{\mathrm{ap}}}{G_{\mathrm{ap}}} \tag{1.1}$$

is as high as possible, and hence Fe/MgO (double barrier) MTJs have been of great interest [7–9].

In order to assist the ongoing endeavor to improve electronic and spintronic appliances, the main objective of this work is to implement a numerical scheme making theoretical, predictive nanoscale device modeling affordable. This goal is quite challenging, because the aforementioned tendency toward miniaturization requires a quantum-mechanical treatment to account for tunneling and quantum interference effects. Realistic devices do, however, produce waste heat, which induces counteracting phase-breaking scattering events. Most importantly, electrons interact

[1] `https://www.intel.com/content/www/us/en/silicon-innovations/intel-14nm-technology.html?wapkw=intel+14nm+technology`

[2] See footnote 1.

[3] `https://www.intel.com/content/www/us/en/silicon-innovations/standards-22-nanometers-technology-backgrounder.html`

with temperature-induced harmonic lattice vibrations, so-called phonons, which leads to a plethora of physical phenomena ranging from electrical over thermal resistivity to superconductivity [10, 11]. At even higher temperatures, anharmonic lattice vibrations introduce thermal expansion [12]. Finally, being predictive requires the use of parameter-free *ab initio* calculations. To paraphrase, we aim for a quantum-mechanical *ab initio* method suited to describe phase-breaking scattering events in complex transport systems.

Various efforts to describe electronic transport including the effects of lattice vibrations have been made in the past. However, most of those reported methods do fall short of at least one of the aforementioned requirements. While, e.g., the Holstein transport equation provides a quantum-mechanics-based calculation scheme capable of accounting for electron-phonon interactions since the early 1960s, its applications have been restricted to rather simplistic situations [13, 14]. In the studies of more realistic systems, the semi-classical Boltzmann formalism is extensively used, which is essentially because it shows quite good results for simple metals, especially if *ab initio* phonon calculations are used to model the vibrational degrees of freedom [10, 15–17]. The reason for this success may be based on the observation that if the one-phonon approximation to the self-energy is used in conjunction with the quasiparticle approximation to the spectral function, then the Kadanoff-Baym formalism may be related to the results proposed by Holstein [13], which, in the DC limit, further reduces to the Boltzmann transport equation [18].

To overcome such restrictions and to meet the expressed requirements, the most promising approach is to extend a purely quantum-mechanical method capable of handling realistic systems by the ability to account for phase-breaking scattering events. At the time of writing, density-functional theory (DFT) has emerged as the *de facto* standard for complex *ab initio* solid state calculations [19]. Among the various formulations of this theory, two important "philosophical schools" may be identified: Either the eigensolutions of the Kohn-Sham Hamiltonian are obtained directly [20, 21], or the corresponding Green's function is calculated [22, 23]. Both formulations may further be categorized by the applied basis set. Although plane waves are an overwhelmingly popular basis set [24–26], a physically very appealing notion is to consider a solid as the superposition of isolated atoms and to use multiple scattering theory to solve for the full system. This is exactly the idea of the Korringa-Kohn-Rostoker (KKR) method, and the natural choice of basis is given by an angular momentum expansion [23, 27].

From a technical point of view, however, DFT does not lend itself to a straightforward extension to finite temperatures, because its mathematical derivation only allows for the evaluation of the electronic ground-state density [19, 21, 28]. Even though there is no rigorous justification, experience nevertheless proves this theory to be a valid starting point to treat a multitude of different scattering mechanisms. Hence, one possibility to extend DFT is to model any phase-breaking scattering events as an effective chemical disorder. Within this so-called alloy analogy it proves very important to average over many different possible configurations [14]. In case of electron-phonon interactions, these different configurations are possible lattice

displacements, and the averaging could therefore be done either using supercell methods [29], or, alternatively, the so-called coherent potential approximation (CPA) [14, 30–32].

Another extremely powerful approach to introduce phase-breaking scattering, which, simultaneously, focuses on the description of electronic transport, is the previously mentioned Kadanoff-Baym or Keldysh formulation of the non-equilibrium Green's function formalism (NEGF). The effective transmission may be calculated in the Landauer-Büttiker framework, where the electron-phonon interaction is modeled by means of fictitious terminals – so-called Büttiker probes – giving rise to additional self-energies [33–35]. Not only is this method numerically more stable in comparison to linear-response formulations [36], it further allows for the self-consistent calculation of transport under applied bias voltage [37], which is an outstanding feature.

Regardless of the particular choice, all previously discussed methods must of course rely on an accurate description of the vibrational degrees of freedom if the phase-breaking scattering shall model the electron-phonon coupling. A physically appealing calculation technique is given by the frozen-phonon approach [38–40]: For every wave vector $\underline{q}$ of interest, the corresponding phonon displacement patterns are imposed on suitable supercells. Based thereupon, the change in the effective potential and eigenenergies is calculated self-consistently. While this method might in principle account for anharmonic effects in the lattice vibrations, the wavelength and hence the necessary supercells become forbiddingly large for small $\|\underline{q}\|$. An accurate sampling of the Brillouin zone near the Γ point is hence computationally very demanding. With the advent of density-functional perturbation theory (DFPT), however, this issue was overcome, because any changes in the effective potential may now be calculated as the response to atomic-displacement-induced perturbations of the lattice [20, 41, 42].

Although the monochromatic nature of DFPT allows for a trivial parallelization algorithm, still a fully self-consistent calculation is necessary per phonon mode. The computational effort thus severely limits the achievable accuracy of wave-vector-integrated quantities like e.g. the imaginary part of the electron-phonon self-energy (2.141), because the corresponding integrands often contain energy-conserving delta distributions. Pending further theoretical progress or access to improved computational facilities, interpolation techniques exploiting the localization of both electronic wave function and phonon perturbation to date depict the physically most sound remedy [17, 43, 44]. As maximally localized Wannier functions (MLWFs) [45, 46] fulfill these desired properties by construction, they are the basis of choice in the employed third party code EPW [17, 43].

Given these considerations, in order to fulfill the projected main objectives, the outline of this work is as follows: In chapter 2 and – in case of in-detail discussions of selected theoretical issues – appendix A, an as of yet missing thorough mathematical and physical discussion of the possibilities to incorporate phase-breaking scattering events by means of suitable self-energies in the NEGF formalism as implemented in the Gießen KKR code is provided. This is, to the best of our knowledge, the first implementation of the Büttiker probe technique within a KKR Green's function code.

We further introduce a calculational scheme to obtain the necessary self-energies by means of a wave-vector averaging of results obtained using well established third party codes in the case of nonmagnetic metals. Additionally, the quasi-harmonic approximation and the Debye-Grüneisen theory to account for thermal expansion are discussed. The chapter 3 is devoted to the verification of the implementation and the physical validity of the proposed method by first studying the bulk-like nonmagnetic metallic test systems copper and aluminum in comparison to Boltzmann results. Subsequently, after providing an in-depth description of the relevant transport mechanisms accountable for the resonant behavior of Fe/MgO double barrier magnetic tunnel junctions, we advance a fitting procedure to obtain a suitable self-energy approximation in case of magnetic metals from spin-resolved *ab initio* resistivity data. These results allow to analyze the at the time of writing barely investigated effects of temperature on the resonant electronic transport and yield the foundations for additional studies regarding the dependence of TMR and other spin caloritronic properties on electron-phonon scattering.[4] Finally, we summarize in chapter 4 the main results of this work and give an outlook on future work.

[4] Please note, that although all technicalities are solved within this work, the necessary calculations with antiparallel aligned magnetic moments in the electrodes will double the computational cost. This subsequent step is hence beyond the scope of this work, but work in progress.

2. Theory

One of the main tasks of modern condensed matter theory is to describe the statics and dynamics of both the electrons and the nuclei constituting a solid. Neglecting any relativistic effects or external perturbations, this requires solving for the eigenstates and -energies of the Hamiltonian [47]

$$\begin{aligned}\tilde{H} = &-\sum_{i=1}^{N_e} \nabla_{\underline{r}_i}^2 - \sum_{n=1}^{N_n} \frac{1}{M_n} \nabla_{\underline{R}_n}^2 + \sum_{i,j=1}^{N_e}{}' \frac{1}{\|\underline{r}_i - \underline{r}_j\|} - \sum_{i=1}^{N_e}\sum_{n=1}^{N_n} \frac{2Z_n}{\|\underline{r}_i - \underline{R}_n\|} \\ &+ \sum_{n,m=1}^{N_n}{}' \frac{Z_n Z_m}{\|\underline{R}_n - \underline{R}_m\|}\end{aligned} \tag{2.1}$$

composed of the kinetic energies of both species as well as their mutual interactions governed by Coulomb's law. In this equation N_e and N_n denote the number of electrons and nuclei, respectively. Similarly, $\{\underline{r}\}$ and $\{\underline{R}\}$ are the corresponding spatial degrees of freedom, and $\{Z\}$ the charge numbers. Here and in the following Rydberg atomic units, i.e., $\hbar = 1, m_e = \frac{1}{2}, e = \sqrt{2}$, and $\epsilon_0 = \frac{1}{4\pi}$, have been used to simplify the notation.

Although the Hamiltonian (2.1) seems elementary, it describes a differential equation in both electronic and ionic degrees of freedom, which proves to be an exquisite problem to solve. However, given that the ratio of electron to nucleus mass $\frac{1}{M} < 10^{-4}$ is rather small, the kinetic energy term of the nuclei may – in lowest order perturbation theory – be neglected. This idea is commonly referred to as Born-Oppenheimer approximation [20, 47–49] and promotes the following solution strategy: In a first step, the electronic system with *fixed* nuclei positions

$$H_{\mathrm{BO}}^{\{\underline{R}\}} = -\sum_{i=1}^{N_e} \nabla_{\underline{r}_i}^2 + \sum_{i,j=1}^{N_e}{}' \frac{1}{\|\underline{r}_i - \underline{r}_j\|} - \sum_{i=1}^{N_e}\sum_{n=1}^{N_n} \frac{2Z_n}{\|\underline{r}_i - \underline{R}_n\|} + \sum_{n,m=1}^{N_n}{}' \frac{Z_n Z_m}{\|\underline{R}_n - \underline{R}_m\|} \tag{2.2}$$

is solved for the electronic eigenstates and eigenenergies

$$H_{\mathrm{BO}}^{\{\underline{R}\}} \left|\phi_\alpha(\{\underline{R}\})\right\rangle = E_\alpha(\{\underline{R}\}) \left|\phi_\alpha(\{\underline{R}\})\right\rangle . \tag{2.3}$$

Then, exploiting that these states form a complete and orthonormal set for each choice of $\{\underline{R}\}$, the wave function of the general condensed matter Hamiltonian (2.1) is expanded in terms of these solutions. Inserting this expression in the stationary Schrödinger equation of the full wave function $\tilde{H}\left|\psi\right\rangle = \mathcal{E}\left|\psi\right\rangle$ yields a system of coupled differential equations for the expansion coefficients $\chi_\alpha(\{\underline{R}\})$ [47]

$$\left(-\sum_{n=1}^{N_n} \frac{1}{M_n} \nabla_{\underline{R}_n}^2 + E_\alpha(\{\underline{R}\})\right) \chi_\alpha(\{\underline{R}\}) + \sum_\beta A_{\alpha,\beta}(\{\underline{R}\}) \chi_\beta(\{\underline{R}\}) = \mathcal{E}\chi_\alpha(\{\underline{R}\}), \tag{2.4}$$

i.e., for the wave functions of the nuclei. The Born-Oppenheimer approximation is now to neglect the transition matrix elements $A_{\alpha,\beta}(\{\underline{R}\})$ depicting the interactions of electrons and nuclei [47, 49], thus leaving the ions to move in an effective potential $E_\alpha(\{\underline{R}\})$, the so-called Born-Oppenheimer energy surface [20], given by the eigenenergies of the electronic system.

While the analysis of the thereby artificially decoupled electronic structure – discussed in more detail in the next section 2.1 – often provides reasonably accurate results in the low-temperature regime, it failes to reproduce the correct temperature dependence of various material properties [11, 12]. A rather prominent example is the electrical resistivity of metallic systems, which is strongly influenced or even dominated by additional phase-breaking interactions of the electrons with the temperature-induced vibrations of the nuclei [10, 11, 14, 16]. As this particular work is mainly concerned with transport phenomena (see section 2.2 for a theoretical treatment), the renormalization of the electronic structure due to vibrations must therefore be taken into account. A systematic way to do so is the perturbative quantum-field-theoretical approach to electron-phonon coupling in the Keldysh formulation of the non-equilibrium Green's function formalism [50, 51] as illustrated in section 2.3. However, even in the simplest metallic systems it is not sufficient to regard the ionic movement in the Born-Oppenheimer energy surface $E_\alpha(\{\underline{R}\})$ as perfectly harmonic, especially if one is interested in an accurate description of the temperature dependence of the resistivity above room temperature [10, 16]. As a preliminary remedy, we will propose in section 2.4 to treat such effects in the so-called quasi-harmonic approximation, i.e., we will assume that the effective potential $E_\alpha(\{\underline{R}\})$ may still be considered harmonic if the centers $\{\underline{R}^0\}$ of the series expansion are chosen to mimic the thermal expansion of the system.

2.1. Electronic Structure

As discussed above, the first step in the approximate solution of the Hamiltonian (2.1) is to obtain the eigensolutions of the Born-Oppenheimer Hamiltonian (2.2). Although already a simplified problem, the motion of an electron is still coupled to the dynamics of all other electrons by means of the Coulomb interaction. Hence, the electronic many-particle wave function will depend on roughly 10^{23} three-dimensional coordinates in a non-trivial way, and therefore cannot be evaluated in general.

The remedy is called density-functional theory (DFT) and consists of two major insights: First, Hohenberg and Kohn [28] showed that the (non-degenerate) ground-state density uniquely[1] determines the external potential. Additionally, this density minimizes the total energy functional [19, 20, 28]

$$E[n] = F[n] + \int \mathrm{d}^3 r \; n(\underline{r}) V_{\mathrm{ext}}^{\{\underline{R}\}}(\underline{r}), \tag{2.5}$$

where the functional F is independent of the external potential, but otherwise not explicitly known. If, however, the electron-electron interaction vanishes, then F

[1] I.e., up to a constant value.

describes the ground-state kinetic energy T_0 of a system of non-interacting particles, which motivates the ansatz [19–21]

$$F[n] = T_0[n] + \int \mathrm{d}^3 r \int \mathrm{d}^3 r' \, \frac{n(\underline{r}) n(\underline{r}')}{|\underline{r} - \underline{r}'|} + E_{\mathrm{xc}}[n]. \tag{2.6}$$

In this equation, the second term describes the classical self-interaction, and any unknown portions of F are gathered in the yet again unknown "exchange-correlation functional" E_{xc}. Variation of the total energy functional (2.5) with respect to the density while ensuring the constraint of a fixed electron count by means of Lagrange multipliers yields the second major insight of DFT: The ground-state density of the interacting system coincides with the ground-state density of non-interacting "Kohn-Sham quasiparticles" moving in the effective potential [19–21]

$$V_{\mathrm{eff}}^{\{\underline{R}\}}(\underline{r}) = V_{\mathrm{ext}}^{\{\underline{R}\}}(\underline{r}) + 2 \int \mathrm{d}^3 r' \, \frac{n(\underline{r}')}{|\underline{r} - \underline{r}'|} + \frac{\delta E_{\mathrm{xc}}[n]}{\delta n(\underline{r})}, \tag{2.7}$$

i.e., instead of solving the Born-Oppenheimer Hamiltonian one could equally well obtain the ground-state density corresponding to the Kohn-Sham Hamiltonian [20]

$$H_{\mathrm{KS}}^{\{\underline{R}\}} = -\sum_{i=1}^{N_e} \nabla_{\underline{r}_i}^2 + \sum_{i=1}^{N_e} V_{\mathrm{eff}}^{\{\underline{R}\}}(\underline{r}_i) \tag{2.8}$$

if the exchange-correlation potential were known. In practice, there exist multiple kinds of approximations which often depict the physics of the system under consideration sufficiently well. Given that the effective potential depends on the density as well as determining this quantity via Poisson's equation, the solution of the eigenvalue problem (2.8) has to be performed iteratively until convergence is achieved [21].

There are at least two possible ways to solve the Kohn-Sham Hamiltonian in each step of the iteration: Either the eigenstates or "Kohn-Sham orbitals" are expanded in a suitable basis set (e.g., plane waves [20, 21]), or the eigenvalue problem is rewritten in terms of Green's functions. While the first approach is used in the evaluation of the electron-phonon self-energy as described in section 2.3, all other calculations presented in this work are performed in the latter framework discussed in the next section. In order to reflect the general applicability of the Green's function technique, the notations $\mathcal{H}_{\mathrm{KS}}^{\{\underline{R}\}}$ and $\mathcal{V}_{\mathrm{eff}}^{\{\underline{R}\}}$ are replaced by $\mathcal{H}$ and $\mathcal{V}$, respectively.

2.1.1. Green's Functions

From a mathematical point of view, the definition of the Green's operator – in the following colloquially called Green's function – arises naturally from the study of inhomogeneous differential equations

$$\mathcal{L} \, |y\rangle = |f\rangle \, , \tag{2.9}$$

where $\mathcal{L}$ denotes a linear differential operator on a suitable function space [52]. If the (left) inverse operator $\mathcal{G}$ of $\mathcal{L}$ exists, the solution $|y\rangle$ may be formally obtained by multiplying with this inverse from the left, i.e.,

$$|y\rangle = \mathcal{G}\mathcal{L}\,|y\rangle = \mathcal{G}\,|f\rangle\,. \tag{2.10}$$

Hence, if $\mathcal{G}$ is known, then the differential equation (2.9) may be solved for *arbitrary* inhomogeneities $|f\rangle$, presuming $\mathcal{G}\,|f\rangle$ exists and can be computed.

In the context of density-functional theory, the differential equation under consideration is usually the (stationary) Schrödinger equation of a Kohn-Sham quasiparticle. The parametric dependence on the quasiparticle energy E may be accounted for by the definition of an energy-dependent differential operator $\mathcal{L}(E)$:

$$\mathcal{H}\,|\psi(E)\rangle = E\,|\psi(E)\rangle \quad \Leftrightarrow \quad \underbrace{(E\mathbb{1} - \mathcal{H})}_{\equiv\mathcal{L}(E)}\,|\psi(E)\rangle = \underbrace{0}_{\equiv|f\rangle}. \tag{2.11}$$

Given that equation (2.11) is the eigenvalue problem of a Hamiltonian $\mathcal{H}$ the kernel of $\mathcal{L}(E)$ is non-trivial at the corresponding eigenenergies, and therefore the associated Green's function $\mathcal{G}(E) \equiv \mathcal{L}^{-1}(E)$ will be singular at these energy values.

Many physical observables[2] may be evaluated by integrating the Green's function in the energy domain. Hence, singularities constitute severe challenges both analytically, as the existence of such integrals has to be ensured, and numerically, because very dense meshes would be required to accurately sample the highly structured integrands. Such issues may be circumvented by studying the Green's function [22]

$$\mathcal{G}(z) \equiv (z\mathbb{1} - \mathcal{H})^{-1}\,, \quad z = E + i\eta, \quad E, \eta \in \mathbb{R}, \tag{2.12}$$

in complex energy space: Firstly, complex analysis provides puissant theoretical results to deal with singularities, and secondly the poles of the Green's function will be broadened to Lorentz distributions for nonvanishing imaginary parts,[3] thus drastically reducing the necessary sampling in numerical calculations.

Lippmann-Schwinger Equation and Dyson's Equation

One of the biggest advantages of Green's functions is the possibility to exactly relate a system characterized by a Hamiltonian $\mathcal{H} = \mathring{\mathcal{H}} + \Delta\mathcal{V}$ to a "reference" system $\mathring{\mathcal{H}}$ by means of the "reference Green's function" $\mathring{\mathcal{G}}(z) = \left(z\mathbb{1} - \mathring{\mathcal{H}}\right)^{-1}$ and the corresponding difference in potentials $\Delta\mathcal{V}$: Starting from the stationary Schrödinger equation for the Hamiltonian $\mathcal{H}$ we may prove[4] the Lippmann-Schwinger equation, an integral equation for the corresponding eigenfunctions, i.e.,

$$\left(z\mathbb{1} - \mathring{\mathcal{H}}\right)|\psi(z)\rangle = \Delta\mathcal{V}\,|\psi(z)\rangle \quad \Leftrightarrow \quad |\psi(z)\rangle = |\mathring{\psi}(z)\rangle + \mathring{\mathcal{G}}(z)\Delta\mathcal{V}\,|\psi(z)\rangle\,, \tag{2.13}$$

[2] A prominent example in DFT calculations constitutes the charge density, see equation (2.28).

[3] This may be seen by analyzing the spectral representation (2.20) for complex energy arguments $z = E + i\eta$ in the vicinity of an eigenenergy E_α.

[4] A detailed discussion of the necessary considerations in case of possibly complex, energy-dependent potentials or "self-energies" is given in appendix A.2.

where $|\mathring{\psi}(z)\rangle \in \ker\left(z\mathbb{1} - \mathring{\mathcal{H}}\right)$ is an arbitrary solution of the reference Hamiltonian. For example, in real space representation – assuming the potential difference is diagonal in its spacial variables – this relation would reduce to a Fredholm equation of the second kind

$$\begin{aligned}\psi(\underline{r}, z) &= \left\langle r \,\middle|\, \mathring{\psi}(z) \right\rangle + \int \mathrm{d}^3 r' \int \mathrm{d}^3 r'' \left\langle r \,\middle|\, \mathring{\mathcal{G}}(z) \,\middle|\, r' \right\rangle \langle r' \,|\, \Delta\mathcal{V} \,|\, r'' \rangle \langle r'' \,|\, \psi(z) \rangle \\ &= \mathring{\psi}(\underline{r}, z) + \int \mathrm{d}^3 r' \, \mathring{G}(\underline{r}, \underline{r}', z) \Delta V(\underline{r}') \psi(\underline{r}', z).\end{aligned} \tag{2.14}$$

Besides the eigenstates it is also possible to calculate the Green's function of the new system from the reference Green's function and the potential difference [22]: Rearranging the defining equation (2.12)

$$\begin{aligned}&\left(z\mathbb{1} - \mathring{\mathcal{H}} - \Delta\mathcal{V}\right)\mathcal{G}(z) = \mathbb{1} \\ \Leftrightarrow &\left(z\mathbb{1} - \mathring{\mathcal{H}}\right)\mathcal{G}(z) = \mathbb{1} + \Delta\mathcal{V}\mathcal{G}(z)\end{aligned} \tag{2.15}$$

and multiplying with $\mathring{\mathcal{G}}(z)$ from the left yields Dyson's equation

$$\mathcal{G}(z) = \mathring{\mathcal{G}}(z) + \mathring{\mathcal{G}}(z)\Delta\mathcal{V}\mathcal{G}(z), \tag{2.16}$$

which may be formally solved as

$$\mathcal{G}(z) = \left(\mathbb{1} - \mathring{\mathcal{G}}(z)\Delta\mathcal{V}\right)^{-1} \mathring{\mathcal{G}}(z). \tag{2.17}$$

To paraphrase, if we have access to *any* Green's function $\mathring{\mathcal{G}}(z)$ and if the inverse of $\left(\mathbb{1} - \mathring{\mathcal{G}}(z)\Delta\mathcal{V}\right)$ exists and can be evaluated, then it is possible to calculate the Green's function of the new system. Hence, in the next section we will derive the real space representation of the Green's function of a free particle.

Reference Green's Function

A powerful tool for working with Green's functions is the so-called spectral representation, which will be discussed preliminarily to deriving the free Green's function. Let $\{|\alpha\rangle\}$ be the eigenbasis of a Hamiltonian $\mathcal{H}$, i.e., $\mathcal{H}\,|\alpha\rangle = E_\alpha\,|\alpha\rangle$. Starting once again from the defining equation (2.12) it is seen that

$$\begin{aligned}&(z\mathbb{1} - \mathcal{H})\mathcal{G}(z) = \mathbb{1} \\ \Rightarrow &\int \mathrm{d}\alpha'' \, \langle \alpha \,|\, (z\mathbb{1} - \mathcal{H}) \,|\, \alpha'' \rangle \langle \alpha'' \,|\, \mathcal{G}(z) \,|\, \alpha' \rangle = \langle \alpha \,|\, \alpha' \rangle \\ \Leftrightarrow &\int \mathrm{d}\alpha'' \, (z - E_{\alpha''}) \delta(\alpha - \alpha'') \langle \alpha'' \,|\, \mathcal{G}(z) \,|\, \alpha' \rangle = \delta(\alpha - \alpha') \\ \Leftrightarrow &\langle \alpha \,|\, \mathcal{G}(z) \,|\, \alpha' \rangle = \frac{\delta(\alpha - \alpha')}{z - E_\alpha}, \quad z \neq E_\alpha.\end{aligned} \tag{2.18}$$

These conversions make use of the fact that the eigenvectors of the Hamiltonian form a Hilbert basis, i.e., they constitute a complete and orthonormal set:

$$\int \mathrm{d}\alpha \; |\alpha\rangle \langle\alpha| = \mathbb{1}, \quad \text{and} \quad \langle\alpha \,|\, \alpha'\rangle = \delta(\alpha - \alpha'). \tag{2.19}$$

In summary, the Green's function is a diagonal operator when expressed in the eigenbasis of the corresponding Hamiltonian. This is to be expected, because $\mathcal{H}$ is diagonal in its eigenbasis, so is $z\mathbb{1} - \mathcal{H}$, and as the inverse of a diagonal matrix is again diagonal consisting of the inverse diagonal elements the observation follows. Employing once more the completeness of the eigenbasis, we arrive at the spectral representation of the Green's function [22]

$$\mathcal{G}(z) = \int \mathrm{d}\alpha \int \mathrm{d}\alpha' \; |\alpha\rangle \langle\alpha \,|\, \mathcal{G}(z) \,|\, \alpha'\rangle \langle\alpha'| = \int \mathrm{d}\alpha \; \frac{|\alpha\rangle \langle\alpha|}{z - E_\alpha}. \tag{2.20}$$

Considering the Hamiltonian $\mathring{\mathcal{H}} = -\nabla^2$ of a free electron it is well known that the plane waves $\langle r \,|\, k\rangle = \mathrm{e}^{i\underline{k}\cdot\underline{r}}$ form a complete orthogonal set of eigenfunctions, and therefore we may write the free Green's function in real space as

$$\mathring{G}(\underline{r}, \underline{r}', z) = \left\langle r \,\middle|\, \mathring{\mathcal{G}}(z) \,\middle|\, r' \right\rangle = \int \frac{\mathrm{d}^3 k}{(2\pi)^3} \; \frac{\mathrm{e}^{i\underline{k}\cdot(\underline{r}-\underline{r}')}}{z - k^2}. \tag{2.21}$$

Here and in the following we have chosen Rydberg atomic units, i.e., $\hbar = 1$, $m_\mathrm{e} = \frac{1}{2}$, and therefore $E(\underline{k}) = k^2$. Using spherical coordinates as well as Cauchy's residue theorem, this integral may readily be evaluated as [53, A1.3]

$$\mathring{G}(\underline{r}, \underline{r}', z) = -\frac{1}{4\pi} \frac{\mathrm{e}^{i\sqrt{z}|\underline{r}-\underline{r}'|}}{|\underline{r} - \underline{r}'|}. \tag{2.22}$$

As expected from a physical point of view, the Green's function of a free particle is not dependent on both spacial variables $\underline{r}$ and $\underline{r}'$, but only on their difference:

$$\mathring{G}(\underline{r}, \underline{r}', z) = \mathring{G}(\underline{r} - \underline{r}', z). \tag{2.23}$$

Density Operator

It is known from courses on basic quantum mechanics, that the expectation value of any observable $\mathcal{O}$ of a system in thermal equilibrium may be calculated from the density operator $n(E)$ as [54]

$$\langle \mathcal{O}(E) \rangle = \mathrm{Tr}\left[\mathcal{O}(E) n(E)\right]. \tag{2.24}$$

Taking a closer look at the spectral representation (2.20) it is seen that the Green's function does not only contain information about the eigenvalues of the system, but also of the eigenstates. Thus, it should be possible to relate the density operator

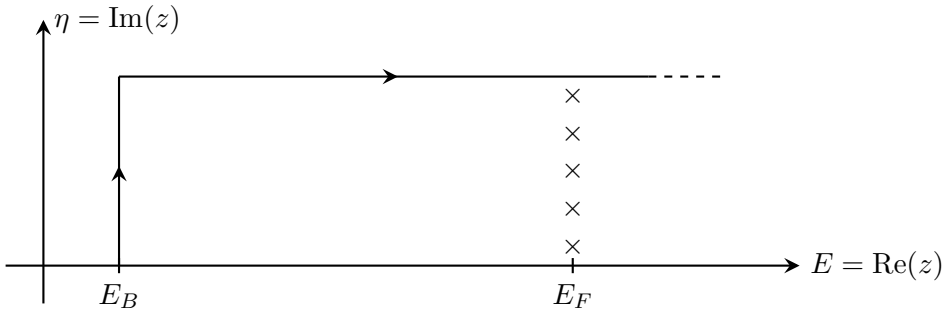

Figure 2.1.: Path used in the complex-energy contour integration (2.29) of the charge density. If a separate solver for the core density is used, E_B is chosen as a lower bound for the conduction band, otherwise as an energy below all electronic states. E_F denotes the Fermi energy, and the crosses indicate the location of the Matsubara poles (2.31).

to the Green's function, which may be achieved by exploiting its different limiting behavior for vanishing imaginary parts of the energy argument [55]

$$\begin{aligned}\lim_{\mathrm{Im}\, z\downarrow 0}\Big(\mathcal{G}(z)-\mathcal{G}^\dagger(z)\Big) &= \lim_{\mathrm{Im}\, z\downarrow 0}\int \mathrm{d}\alpha\, \left(\frac{|\alpha\rangle\langle\alpha|}{z-E_\alpha}-\frac{|\alpha\rangle\langle\alpha|}{z^*-E_\alpha}\right)\\ &= \lim_{\eta\downarrow 0}\int \mathrm{d}\alpha\ |\alpha\rangle\left(\frac{1}{E+i\eta-E_\alpha}-\frac{1}{E-i\eta-E_\alpha}\right)\langle\alpha|\,.\end{aligned} \tag{2.25}$$

With the Sokhotski–Plemelj[5] theorem [56]

$$\lim_{\eta\downarrow 0}\int \mathrm{d}\alpha\ \frac{|\alpha\rangle\langle\alpha|}{E-E_\alpha\pm i\eta} = \mp i\pi\int \mathrm{d}\alpha\ |\alpha\rangle\,\delta(E-E_\alpha)\,\langle\alpha| + \mathcal{P}\int \mathrm{d}\alpha\frac{|\alpha\rangle\langle\alpha|}{E-E_\alpha} \tag{2.26}$$

we see that the density operator may be written as [56]

$$n(E)\equiv\int \mathrm{d}\alpha\ |\alpha\rangle\,\delta(E-E_\alpha)\,\langle\alpha| = \frac{i}{2\pi}\lim_{\mathrm{Im}\, z\downarrow 0}\Big(\mathcal{G}(z)-\mathcal{G}^\dagger(z)\Big)\,. \tag{2.27}$$

Hence, if the Green's function of a system is known, it is possible to calculate *any* quantity of interest, e.g. the charge density of a particle having charge q [56]

$$\rho(\underline{r}) = \int_{-\infty}^{E_F}\mathrm{d}E\ \rho(\underline{r},E) = \int_{-\infty}^{E_F}\mathrm{d}E\ q\,\langle r\,|\,n(E)\,|\,r\rangle = -\frac{q}{\pi}\int_{-\infty}^{E_F}\mathrm{d}E\ \mathrm{Im}\,G(\underline{r},\underline{r},E). \tag{2.28}$$

Revisiting that the definition of the Green's function for complex energies (2.12) was motivated by the poles at its eigenenergies, it is obvious that the numerical evaluation of equation (2.28) would be inefficient. Instead, a contour integration along the complex energy path depicted in figure 2.1 may be used: [55, 57]

$$\rho(\underline{r}) = -\frac{q}{\pi}\,\mathrm{Im}\int_{\mathcal{C}}\mathrm{d}z\ G(\underline{r},\underline{r},z)f(z,E_F,T) - 2qk_BT\,\mathrm{Re}\sum_j G(\underline{r},\underline{r},z_j). \tag{2.29}$$

[5] In physics, this relation is better known as the so-called Dirac identity.

Note that the introduction of the Fermi-Dirac distribution

$$f(z,\mu,T) = \left(\exp\left[\frac{z-\mu}{k_B \cdot T}\right] + 1\right)^{-1} \tag{2.30}$$

is justified by finite-temperature density-functional theory [58], which further gives rise to a second addend necessary to correct for any so-called Matsubara poles

$$z_j = E_F + i\pi(2j-1)k_B T, \quad j \in \mathbb{N}, \tag{2.31}$$

of the Fermi-Dirac distribution enclosed by the energy contour $\mathcal{C}$. In these formulae, E_F denotes the Fermi energy, and k_B is Boltzmann's constant. Due to the Lorentzian broadening of the poles it is usually sufficient to sample the Green's function on 30 points along contour $\mathcal{C}$, whereas the energy integration along the real axis would require several thousands of points for a similar accuracy [57, 59].

2.1.2. Korringa-Kohn-Rostoker Formalism

Except for any explicit real space projections and the spectral representation of the Green's function, everything stated in the previous subsection 2.1.1 is independent of a special choice of basis set and hence to be considered a general property of the Green's operator. These relations therefore constitute the essence of most non-time-resolved Green's function methods.

In accordance with its origins, i.e., multiple scattering theory [60], the specialty of the Korringa-Kohn-Rostoker (KKR) formalism is the use of an angular momentum basis, which arises naturally when employing the so-called muffin-tin approximation: It is assumed that all atoms are centered at positions $\underline{R}_n$, and that the atomic potentials $V^n_{\mathrm{atom}}(\underline{r})$ are confined to spheres[6] $V^n_{\mathrm{MT}} \equiv \{\underline{r} \in \mathbb{R}^3 : \|\underline{r} - \underline{R}_n\| \leq R^n_{\mathrm{MT}}\}$ of the muffin-tin radii R^n_{MT}. Further, within these spheres the potentials are supposed to be spherically symmetric and hence a function of $r \equiv \|\underline{r}\|$ only. The total potential of the whole system is then given by the superposition [22, 53]

$$V(\underline{r}) = \sum_n V^n(\underline{r}), \quad V^n(\underline{r}) = \begin{cases} V^n_{\mathrm{atom}}(r) & \text{if } r \leq R^n_{\mathrm{MT}} \\ V_0 & \text{if } r > R^n_{\mathrm{MT}} \end{cases}, \tag{2.32}$$

where V_0 is a constant carefully chosen to minimize any discontinuities at the muffin-tin boundaries.[7] These assumptions justify a product ansatz

$$\psi_L(\underline{r}, z) = R_l(r, z) \cdot Y_L(\hat{r}), \quad L = (l, m), \tag{2.33}$$

for the solutions of the stationary Schrödinger equation in regions of constant potential, leading to a differential equation for the radial part

$$\left(\partial_r^2 + z - \frac{l(l+1)}{r^2}\right) u_l(r, z) = 0, \quad R_l(r, z) = \frac{u_l(r, z)}{r}. \tag{2.34}$$

[6] Following a widespread habit of the KKR community, we use "sphere" in the meaning of "ball".

[7] Of course it is then possible to shift the total potential V downwards by this very constant V_0, thus forcing the potential to vanish outside of the muffin-tin spheres [23]. This gauge is assumed within the remainder of this section.

The solutions are well known: The spherical Bessel functions $j_l(\sqrt{z}r)$ are regular at the origin, while the spherical Neumann functions $n_l(\sqrt{z}r)$ diverge [53].

Instead of following Korringa [27], i.e., writing the incoming and outgoing waves in terms of these regular and irregular solutions and relating them by means of multiple scattering theory, we will build upon the work of Kohn and Rostoker [23] and expand the Green's function. For this purpose we introduce the concise yet powerful vector notation [22]

$$\underline{f}(\underline{r}, z) \equiv \begin{pmatrix} f_{(0,0)}(\underline{r}, z) & f_{(1,-1)}(\underline{r}, z) & f_{(1,0)}(\underline{r}, z) & \dots \end{pmatrix} \tag{2.35}$$

with the components

$$f_L(\underline{r}, z) \equiv f_l(\sqrt{z}r) \cdot Y_L(\hat{r}), \quad f_l \in \{j_l, n_l, h_l^{\pm}\}, \quad h_l^{\pm} \equiv j_l \pm i n_l, \tag{2.36}$$

as well as its column vector counterpart

$$\underline{f}(\underline{r}, z)^{\times} \equiv \begin{pmatrix} f_{(0,0)}(\underline{r}, z)^{\times} \\ f_{(1,-1)}(\underline{r}, z)^{\times} \\ f_{(1,0)}(\underline{r}, z)^{\times} \\ \dots \end{pmatrix}, \tag{2.37}$$

where we have defined

$$f_L(\underline{r}, z)^{\times} \equiv f_l(\sqrt{z}r) \cdot Y_L(\hat{r})^*. \tag{2.38}$$

Reference Green's Function

According to reference [22] the spherical Bessel functions form an orthogonal set of eigenfunctions of the Hamiltonian. Thus, the spectral representation (2.20) yields

$$\mathring{g}(\underline{r}, \underline{r}', z) = \int_{\mathbb{R}^+} \mathrm{d}E \sum_L \frac{\sqrt{E}}{\pi} \frac{j_L(\underline{r}, E) j_L(\underline{r}', E)^*}{z - E}. \tag{2.39}$$

This integral may be solved by first substituting $k \equiv \sqrt{E}$, transforming to spherical coordinates and employing Cauchy's residue theorem on suitable contours (see ref. [22, p. 19] for details) as

$$\mathring{g}(\underline{r}, \underline{r}', z) = -i\sqrt{z}\underline{j}(\wedge(\underline{r}, \underline{r}'), z)\underline{h}^+(\vee(\underline{r}, \underline{r}'), z)^{\times}, \tag{2.40}$$

where $\wedge(\underline{r}, \underline{r}')$ denotes the vector having the smaller norm; $\vee(\underline{r}, \underline{r}')$ analogous.

In case $\underline{r}$ and $\underline{r}'$ represent positions in different muffin-tin spheres it is possible to further rewrite the above representation using the transformation to so-called cell-centered coordinates $\underline{r}^{(\prime)} \to \underline{r}^{(\prime)} + \underline{R}_{n^{(\prime)}}$:

$$\begin{aligned} \mathring{G}(\underline{r} + \underline{R}_n, \underline{r}' + \underline{R}_{n'}, z) &= \mathring{G}(\underline{r} - \underline{r}', \underline{R}_{n'} - \underline{R}_n, z) \\ &= -i\sqrt{z}\underline{j}(\underline{r} - \underline{r}', z)\underline{h}^+(\underline{R}_{n'} - \underline{R}_n, z)^{\times}. \end{aligned} \tag{2.41}$$

Here, the first equality is a result of the translational invariance of the free Green's function (2.23) and the latter of $\|\underline{r}-\underline{r}'\| \leq \|\underline{R}_{n'}-\underline{R}_n\|$ for $n \neq n'$. With the sum rule (for a proof see appendix A.1)

$$j_L(\underline{r}-\underline{r}',z) = 4\pi i^{-l} \sum_{L'L''} i^{l'-l''} C_{LL''}^{L'} j_{L'}(\underline{r},z) j_{L''}(\underline{r}',z)^{\times} \tag{2.42}$$

this relation may be written as [22]

$$\mathring{G}(\underline{r}+\underline{R}_n,\underline{r}'+\underline{R}_{n'},z) = \underline{j}(\underline{r},z)\underline{\underline{\mathring{G}}}^{nn'}(z)\underline{j}(\underline{r}',z)^{\times}, \quad n \neq n', \tag{2.43}$$

where we have defined the so-called structure constants of the free Green's function

$$\mathring{G}_{LL'}^{nn'}(z) \equiv -i4\pi\sqrt{z}(1-\delta_{nn'}) \sum_{L''} i^{l-l'+l''} C_{L'L''}^{L} h_{L''}^{+}(\underline{R}_n-\underline{R}_{n'},z)^{\times} \tag{2.44}$$

as well as the Gaunt coefficients

$$C_{L'L''}^{L} \equiv \int \mathrm{d}\hat{r}\; Y_L(\hat{r})^* Y_{L'}(\hat{r}) Y_{L''}(\hat{r}). \tag{2.45}$$

In summary, the Green's function of the free particle in angular momentum representation reads

$$\mathring{G}(\underline{r}+\underline{R}_n,\underline{r}'+\underline{R}_{n'},z) = \delta_{nn'}\mathring{g}(\underline{r},\underline{r}',z) + \underline{j}(\underline{r},z)\underline{\underline{\mathring{G}}}^{nn'}(z)\underline{j}(\underline{r}',z)^{\times}. \tag{2.46}$$

Dyson's Equation

In order to calculate the Green's function of a system described by the Hamiltonian $\mathcal{H} = \mathring{\mathcal{H}} + \mathcal{V}$, the ansatz [53]

$$G(\underline{r}+\underline{R}_n,\underline{r}'+\underline{R}_{n'},z) = \delta_{nn'} g^n(\underline{r},\underline{r}',z) + \underline{R}^n(\underline{r},z)\underline{\underline{G}}^{nn'}(z)\underline{R}^{n'}(\underline{r}',z)^{\times} \tag{2.47}$$

is made, i.e., instead of an expansion in terms of the spherical Bessel and Hankel functions, the regular solutions

$$\underline{R}^n(\underline{r},z) = \underline{j}(\underline{r},z) + \int_{V_{\mathrm{MT}}^n} \mathrm{d}^3x\; \mathring{g}(\underline{r},\underline{x},z) V^n(\underline{x}) \underline{R}^n(\underline{x},z) \tag{2.48}$$

of the isolated muffin-tin potential V^n are used. Inserting this ansatz as well as the free Green's function (2.46) in Dyson's equation (2.16) yields the relation [53]

$$\begin{aligned}
&\delta_{nn'} g^n(\underline{r},\underline{r}',z) + \underline{j}(\underline{r},z)\underline{\underline{G}}^{nn'}(z)\underline{R}^{n'}(\underline{r}',z)^{\times} \\
=&\delta_{nn'}\left(\mathring{g}(\underline{r},\underline{r}',z) + \int_{V_{\mathrm{MT}}^n} \mathrm{d}^3x\; \mathring{g}(\underline{r},\underline{x},z) V^n(\underline{x}) g^n(\underline{x},\underline{r}',z)\right) \\
&+ \underline{j}(\underline{r},z)\underline{\underline{\mathring{G}}}^{nn'}(z)\left(\underline{j}(\underline{r}',z)^{\times} + \int_{V_{\mathrm{MT}}^{n'}} \mathrm{d}^3x\; \underline{j}(\underline{x},z)^{\times} V^{n'}(\underline{x}) g^{n'}(\underline{x},\underline{r}',z)\right) \\
&+ \underline{j}(\underline{r},z) \sum_m \underline{\underline{\mathring{G}}}^{nm}(z)\underline{\underline{t}}^m(z)\underline{\underline{G}}^{mn'}(z)\underline{R}^{n'}(\underline{r}',z)^{\times},
\end{aligned} \tag{2.49}$$

where the Lippmann-Schwinger equation (2.48) was utilized to simplify the left hand side and the angular momentum representation of the transition operator [53]

$$\underline{\underline{t}}^n(z) = \int_{V^n_{\mathrm{MT}}} \mathrm{d}^3x \; \underline{j}(\underline{x}, z)^{\times} V^n(\underline{x}) \underline{R}^n(\underline{x}, z) \tag{2.50}$$

has been introduced. Employing rather elaborate mathematical results concerning Fredholm integral equations [61–63] it is possible to prove that

$$g^n(\underline{r}, \underline{r}', z) = -i\sqrt{z}\underline{R}^n(\wedge(\underline{r}, \underline{r}'), z)\underline{H}^n(\vee(\underline{r}, \underline{r}'), z)^{\times}, \tag{2.51}$$

$\underline{H}^n$ denoting the irregular scattering solutions of the isolated muffin-tin potential V^n relatable to the spherical Hankel functions $\underline{h}^+$, solves the integral equation

$$g^n(\underline{r}, \underline{r}', z) = \mathring{g}(\underline{r}, \underline{r}', z) + \int_{V^n_{\mathrm{MT}}} \mathrm{d}^3x \; \mathring{g}(\underline{r}, \underline{x}, z) V^n(\underline{x}) g^n(\underline{x}, \underline{r}', z). \tag{2.52}$$

Assuming muffin-tin potentials of the kind (2.32) one may further exploit the semi-separability of g^n to show the validity of the Lippmann-Schwinger-like equation

$$\underline{R}^n(\underline{r}, z)^{\times} = \underline{j}(\underline{r}, z)^{\times} + \int_{V^n_{\mathrm{MT}}} \mathrm{d}^3x \; \underline{j}(\underline{x}, z)^{\times} V^n(\underline{x}) g^n(\underline{x}, \underline{r}, z), \tag{2.53}$$

and hence ansatz (2.47) solves Dyson's equation if the structure constants fulfill the so-called algebraic Dyson's equation [53]

$$\underline{\underline{G}}^{nn'}(z) = \mathring{\underline{\underline{G}}}^{nn'}(z) + \sum_m \mathring{\underline{\underline{G}}}^{nm}(z) \underline{\underline{t}}^m(z) \underline{\underline{G}}^{mn'}(z). \tag{2.54}$$

Although the transition operator $\underline{\underline{t}}^n(z)$ could be obtained from its defining equation (2.50) by means of numerical integration, in practice it is evaluated as[8]

$$t^n_l(z) = -\frac{i}{\sqrt{z}} \frac{\left(L^n_l(z) - {}^l\!/_{R^n_{\mathrm{MT}}}\right) j_l\left(\sqrt{z} R^n_{\mathrm{MT}}\right) + \sqrt{z}\, j_{l+1}\left(\sqrt{z} R^n_{\mathrm{MT}}\right)}{\left(L^n_l(z) - {}^l\!/_{R^n_{\mathrm{MT}}}\right) h^+_l\left(\sqrt{z} R^n_{\mathrm{MT}}\right) + \sqrt{z}\, h^+_{l+1}\left(\sqrt{z} R^n_{\mathrm{MT}}\right)}, \tag{2.55}$$

i.e., in a first step the regular scattering solutions $R^n_l(r, z)$ are calculated using elaborate numerical methods to solve the ordinate differential equation (2.11). This procedure yields the necessary logarithmic derivatives [22]

$$L^n_l(z) = \frac{\partial_r R^n_l\left(R^n_{\mathrm{MT}}, z\right)}{R^n_l\left(R^n_{\mathrm{MT}}, z\right)} \tag{2.56}$$

as a by-product, and therefore the transition operator is completely determined by the unbound eigensolutions of the muffin-tin Hamiltonian.

Revisiting the prerequisites of these results it can be seen that we may iterate the procedure, i.e., we might regard the Green's function (2.47) corresponding to the Hamiltonian $\mathcal{H} = \mathring{\mathcal{H}} + \mathcal{V}$ as a reference Green's function and calculate the

[8] See appendix A.3 for a brief derivation in case of (possibly complex) muffin-tin potentials.

Green's function $\tilde{\mathcal{G}}(z)$ of the system $\tilde{\mathcal{H}} = \mathring{\mathcal{H}} + \tilde{\mathcal{V}} = \mathcal{H} + \Delta\mathcal{V}$ by the very same means, presupposed that $\tilde{V}(\underline{r})$ – and therefore $\Delta\tilde{V}(\underline{r})$ – is a superposition of muffin-tin potentials as described in equation (2.32). This observation yields the foundation of the so-called screened KKR [22], where in a first step the Green's function of a highly repulsive reference potential $\mathcal{V}_{\text{ref}}$ is calculated from the free Green's function. This may be done rather quick, because this Green's function $\mathcal{G}_{\text{ref}}$ is exponentially decaying in real space, and hence the calculation of the structure constants may be restricted to a comparatively small "cluster." Subsequently, the Green's function of the system is evaluated based on this reference.

If the system under study shows translational invariance one may further exploit that in this case the structure constants must depend on $n - n'$ only, and therefore equation (2.54) may be lattice Fourier-transformed [22, 53]

$$\underline{\underline{G}}(\underline{k}, z) = \mathring{\underline{\underline{G}}}(\underline{k}, z) + \mathring{\underline{\underline{G}}}(\underline{k}, z)\underline{\underline{t}}(z)\underline{\underline{G}}(\underline{k}, z) \tag{2.57}$$

and solved by matrix inversion for each wave vector $\underline{k}$ separately.[9] The real space representation necessary for the calculation of, e.g., the charge density (2.29) is then restored by means of a Brillouin zone integration [53]

$$\underline{\underline{G}}^{nn'}(z) = \frac{\Omega}{(2\pi)^3} \int_{\text{BZ}} \mathrm{d}^3k \; \mathrm{e}^{i\underline{k}(\underline{R}_n - \underline{R}_{n'})} \underline{\underline{G}}(\underline{k}, z), \tag{2.58}$$

where Ω denotes the unit cell volume.

2.2. Electronic Transport

A main objective of this work is to study the effects of the coupling of electrons and phonons on transport properties in nanostructures. It is hence necessary to treat both entities as well as their mutual interactions on an equal and fully quantum-mechanical footing. The theoretical framework of choice is the (steady-state) Keldysh formulation of the non-equilibrium Green's function formalism (NEGF): It not only allows for the incorporation of phase-breaking scattering but additionally lends itself to a variety of other generalizations, most notably the possibility to account for any applied bias voltages in a self-consistent manner [37]. We start by introducing the general ideas in an idealized setup, proceed by the inclusion of scattering and complete by discussing some theoretical subtleties regarding the implementation in the KKR formalism.

2.2.1. Non-equilibrium Green's Function Formalism

The partitioning approach [32, 34, 36] certainly is one of the key ideas of the non-equilibrium Green's function formalism: Consider a "typical" transport geometry, i.e.,

[9] In case of the below discussed transport geometries the translational invariance is broken in transport direction only, and therefore an *in-plane* lattice Fourier transform is still possible. Please see (2.96) for details.

a device – or, in general terms, a middle region M – connected to two semi-infinite leads L (for left) and R (right). In order to find a suitable way to calculate the transmission probability T_{LR} from the left to the right lead, the underlying Hilbert space is formally separated into disjointly connected subsystems corresponding to the beforementioned entities. Assuming that there is no direct interaction between the leads, the original "coupled" transport system may be related to the "decoupled system" $\mathcal{H}_{\mathrm{dc}}$ by means of the following "coupling potential" $\mathcal{V}_{\mathrm{c}}$ [32, 36]

$$\mathcal{H}_{\mathrm{dc}} = \begin{pmatrix} \mathcal{H}_L & 0 & 0 \\ 0 & \mathcal{H}_M & 0 \\ 0 & 0 & \mathcal{H}_R \end{pmatrix}, \quad \mathcal{V}_{\mathrm{c}} = \begin{pmatrix} 0 & \mathcal{V}_{LM} & 0 \\ \mathcal{V}_{ML} & 0 & \mathcal{V}_{MR} \\ 0 & \mathcal{V}_{RM} & 0 \end{pmatrix}, \quad \mathcal{H}_{\mathrm{c}} = \mathcal{H}_{\mathrm{dc}} + \mathcal{V}_{\mathrm{c}}. \tag{2.59}$$

By rearranging the defining equation $\mathcal{G}_{\mathrm{c}}(z) = \left(z\mathbb{1} - \mathcal{H}_{\mathrm{c}}\right)^{-1}$ in matrix notation

$$\begin{pmatrix} \mathbb{1} & 0 & 0 \\ 0 & \mathbb{1} & 0 \\ 0 & 0 & \mathbb{1} \end{pmatrix} = \begin{pmatrix} z\mathbb{1} - \mathcal{H}_L & -\mathcal{V}_{LM} & 0 \\ -\mathcal{V}_{ML} & z\mathbb{1} - \mathcal{H}_M & -\mathcal{V}_{MR} \\ 0 & -\mathcal{V}_{RM} & z\mathbb{1} - \mathcal{H}_R \end{pmatrix} \cdot \begin{pmatrix} \mathcal{G}_{LL}(z) & \mathcal{G}_{LM}(z) & \mathcal{G}_{LR}(z) \\ \mathcal{G}_{ML}(z) & \mathcal{G}_{MM}(z) & \mathcal{G}_{MR}(z) \\ \mathcal{G}_{RL}(z) & \mathcal{G}_{RM}(z) & \mathcal{G}_{RR}(z) \end{pmatrix} \tag{2.60}$$

we obtain a system of linear equations for the middle region's Green's function of the coupled system $\mathcal{G}_{MM}(z)$:

$$0 = (z\mathbb{1} - \mathcal{H}_L)\mathcal{G}_{LM}(z) - \mathcal{V}_{LM}\mathcal{G}_{MM}(z) \tag{2.61a}$$

$$\mathbb{1} = -\mathcal{V}_{ML}\mathcal{G}_{LM}(z) + (z\mathbb{1} - \mathcal{H}_M)\mathcal{G}_{MM}(z) - \mathcal{V}_{MR}\mathcal{G}_{RM}(z) \tag{2.61b}$$

$$0 = -\mathcal{V}_{RM}\mathcal{G}_{MM}(z) + (z\mathbb{1} - \mathcal{H}_R)\mathcal{G}_{RM}(z) \tag{2.61c}$$

Presuming the existence of the Green's functions $\mathcal{G}_{L/R}(z) = \left(z\mathbb{1} - \mathcal{H}_{L/R}\right)^{-1}$ corresponding to the isolated leads, equations (2.61a) and (2.61c) may be solved for $\mathcal{G}_{LM}(z)$ and $\mathcal{G}_{RM}(z)$, respectively, and inserting these representations into equation (2.61b) yields [32, 36, 64]

$$\mathcal{G}_{MM}(z) = \left(z\mathbb{1} - \mathcal{H}_M - \Sigma_{\mathrm{leads}}(z)\right)^{-1} \tag{2.62}$$

where the so-called self-energy [32, 36]

$$\Sigma_{\mathrm{leads}}(z) = \Sigma_L(z) + \Sigma_R(z) \equiv \mathcal{V}_{ML}\mathcal{G}_L(z)\mathcal{V}_{LM} + \mathcal{V}_{MR}\mathcal{G}_R(z)\mathcal{V}_{RM} \tag{2.63}$$

has been defined. Thus, the effects of the leads on the device may be modeled by additional complex and energy-dependent "potentials," particularly one self-energy addend per lead. This important feature is readily transfered to the density operator of the connected device: From equation (2.27) we find [64]

$$\begin{aligned} n_{MM}(z) &= \frac{i}{2\pi}\left(\mathcal{G}_{MM}(z) - \mathcal{G}_{MM}(z)^\dagger\right) \\ &= \frac{i}{2\pi}\cdot\mathcal{G}_{MM}(z)\left(\mathcal{G}_{MM}^\dagger(z)^{-1} - \mathcal{G}_{MM}(z)^{-1}\right)\mathcal{G}_{MM}^\dagger(z) \\ &= \frac{i}{2\pi}\cdot\mathcal{G}_{MM}(z)\left(-i2\,\mathrm{Im}(z) + \Sigma_{\mathrm{leads}}(z) - \Sigma_{\mathrm{leads}}^\dagger(z)\right)\mathcal{G}_{MM}^\dagger(z) \\ &= \frac{1}{2\pi}\cdot\mathcal{G}_{MM}(z)\Gamma_{\mathrm{leads}}(z)\mathcal{G}_{MM}^\dagger(z) + \frac{1}{\pi}\,\mathrm{Im}(z)\cdot\mathcal{G}_{MM}(z)\mathcal{G}_{MM}^\dagger(z), \end{aligned} \tag{2.64}$$

where this time the so-called broadening functions

$$\Gamma_{\text{leads}}(z) = \Gamma_L(z) + \Gamma_R(z), \quad \Gamma_X \equiv i\left(\Sigma_X - \Sigma_X^\dagger\right), \quad X \in \{L, R\}, \tag{2.65}$$

have been introduced, which may be interpreted as the sum of particle in- and out-fluxes [34]. Dropping the index MM, as within the scope of this work $\mathcal{G}_{MM}(z)$ is the only relevant component of $\mathcal{G}_{\text{c}}(z)$, and performing the limit towards real energies, we confirm that the density operator does in fact split up in addends corresponding to the individual leads:

$$n(E) = n_L(E) + n_R(E), \quad n_X(E) = \lim_{\text{Im}\, z \downarrow 0} \frac{1}{2\pi} \mathcal{G}(z)\Gamma_X(z)\mathcal{G}^\dagger(z). \tag{2.66}$$

From a phenomenological point of view it is now obvious that the transmission probability T_{LR} of a charge carrier from the left to the right lead is proportional to the expectation value (2.24) of the net particle out-flux into the right lead Γ_R of all the charge carriers originating from the left lead (having density n_L):

$$T_{LR}(E) = \lim_{\text{Im}\, z \downarrow 0} \text{Tr}\left[\Gamma_R(z)\mathcal{G}(z)\Gamma_L(z)\mathcal{G}^\dagger(z)\right] \sim \text{Tr}\left[\Gamma_R(E) n_L(E)\right]. \tag{2.67}$$

For a thorough mathematical discussion we refer to the literature [34, 65].

The relation between transmission probability and current density[10] from one terminal L into another R is commonly attributed to Rolf Landauer [34, 66]: The electric current per energy is assumed to be proportional to the charge q of the transmitted charge carriers, their respective transmission probability $T_{LR}(E)$ as well as the difference of their distribution functions $f_{L/R}(E)$ in the leads. Therefore, the total current density j_{LR} per spin degree of freedom is given by

$$j_{LR} = \frac{q}{h} \int_{\mathbb{R}} \mathrm{d}E \; T_{LR}(E)(f_L(E) - f_R(E)). \tag{2.68}$$

In case of a non-vanishing external bias voltage drop, the energy distributions of the charge carriers in the device will not be equal to their equilibrium value, i.e., they are generally unknown. Postulating a continuous change with respect to the spatial variables, this would be true for $f_{L/R}(E)$ in the leads as well. To circumvent this issue, the leads are considered to be perfect conductors, infinitely long and, simultaneously, connected to a charge carrier reservoir in thermodynamic equilibrium. Then, deep within the lead, $f_X(E) = f(E, \mu_X, T_X)$ will be Fermi-Dirac distributions (2.30), where μ_X and $T_X, X \in \{L, R\}$, denote the electrochemical potential and the temperature of the reservoir, respectively [34].[11]

[10] Please note that the current *density* is considered instead of the current: To allow for an in-plane lattice Fourier transform, translational invariance is assumed orthogonal to the transport direction in all the calculations presented within this work. Hence, to avoid infinitely high values, the evaluated transmission probability $T_{LR}(E)$ is in fact normalized to the projection A of the unit cell area into this orthogonal subspace.

[11] Alternatively, one may assume the contacts to be "reflectionless," i.e., the charge carriers may enter the leads with vanishing probability of reflection. In this case the charge carriers in the leads will be Fermi-Dirac distributed everywhere, and hence one is not bound to measure the conductance between two planes deep within the leads [34].

From this, the electrical resistance R_{LR} per spin degree of a device having cross-section A is readily obtained as

$$R_{LR} = \frac{\Delta V_{LR}}{j_{LR} \cdot A} = \frac{2\,(\mu_L - \mu_R)}{G_0 \int_{\mathbb{R}} \mathrm{d}E\; T_{LR}(E)(f_L(E) - f_R(E)) \cdot A}, \tag{2.69}$$

where it was further assumed that the only contribution to the current is due to electrons, and hence $q = -e = -\sqrt{2}$. G_0 is the conductance quantum. Even though the device is considered free of scattering, this resistance will *not* be equal to zero, because the electrons are scattered at the interfaces connecting the device to the leads. Thus, this value is usually referred to as "contact resistance" [34].

Finally, note that – in the limit of vanishing bias voltage ΔV_{LR} – equation (2.69) may be shown to reduce to

$$R_{LR} = \frac{2}{G_0 \cdot T_{LR}(E_F) \cdot A}, \tag{2.70}$$

which is of course the widely known Landauer formula [66] rewritten from conductances to resistances and hence equivalent to the linear response formalism discussed by Datta [34]. However, a careful examination of the proof given in appendix A.4 reveals that the transmission function $T_{LR}(E)$ does *not* have to be "approximately constant over the energy range where transport occurs" [34, p. 89]. Instead, a small "curvature" in the sense of appendix A.4 is a sufficient condition for equation (2.70) to be valid. This result will be exploited in sections 3.1 and 3.2, as it allows to restrict all necessary calculations to the Fermi energy E_F only.

2.2.2. Phase-breaking Scattering Events

Charge carrier transport in condensed matter is usually *not* ballistic, i.e., free of scattering, as was assumed in the preceding chapter. In the case of paramagnetic metals, on which the exploratory focus of this work lies upon, important scattering mechanisms would be the mutual interactions of the electrons with each other,[12] the scattering on impurities and defects as well as the scattering on lattice vibrations or phonons [67, 68]. Besides a transition from the initial electronic state $|n\underline{k}\rangle$ to a new state $|m\underline{k}'\rangle$, possibly accompanied by a change in energy (the inelastic case) or not (elastic scattering), they usually induce a randomization of the phase relations of the electrons. Therefore, the electrons lose their ability to interfere, and hence one may consider the scattered electron to be unrelated to its unscattered ancestor.

It was Büttiker [33] who noted that such a phase-breaking scattering event may be regarded equivalent to the combined process of a charge carrier in state $|n\underline{k}\rangle$ leaving the device through a possibly virtual, i.e., fictitious, terminal, and, simultaneously, another electron having state $|m\underline{k}'\rangle$ entering the system by means of this very same

[12] On the DFT level, both the classical self-interaction of the electrons as well as the quantum-mechanical exchange-correlation contribution are contained in the effective one-particle potential (2.7) of the non-interacting Kohn-Sham particles. Hence, we do not have to explicitly consider this effect in the following.

terminal. This idea of modeling phase-breaking scattering events using these so-called Büttiker probes has successfully been employed by several authors [34, 35, and references therein] and is particularly well suited to be implemented in the previously presented NEGF scheme, as all terminals – whether real or virtual – may be incorporated on equal footing.[13]

Notably, the charge carrier transmission between terminals remains (except for interface effects) purely ballistic in this picture, because all state transitions and hence scattering events occur within the Büttiker probes, not the device. It is thus possible to adapt the former result (2.67) to the new situation: Let $\tilde{\mathcal{G}}(z)$ be the Green's function of the device region coupled to both leads and Büttiker probes, then

$$T_{XY}(E) = \lim_{\operatorname{Im} z \downarrow 0} \operatorname{Tr}\left[\Gamma_Y(z)\tilde{\mathcal{G}}(z)\Gamma_X(z)\tilde{\mathcal{G}}^\dagger(z)\right] \tag{2.71}$$

yields the probability of a charge carrier to leave terminal X and enter terminal Y.

Although this relation is valid for real terminals as well as fictitious ones, in the latter case a problem arises: Given that the virtual terminals are a perfectly hypothetical construct, there is a priori no facility to compute the decoupled Green's functions $\mathcal{G}_\alpha(z)$ for any $\alpha \in \mathcal{S}$, where $\mathcal{S}$ denotes the set of all Büttiker probes or "scatterers" in the device. Therefore, the scattering self-energy obtained by means of the partitioning approach[14]

$$\Sigma_{\text{scat}}(z) = \sum_{\alpha\in\mathcal{S}} \Sigma_\alpha(z) = \sum_{\alpha\in\mathcal{S}} \mathcal{V}_{M\alpha}\mathcal{G}_\alpha(z)\mathcal{V}_{\alpha M} \tag{2.72}$$

may not be evaluated, and, subsequently, the necessary broadening functions

$$\Gamma_\alpha(z) \equiv i\left(\Sigma_\alpha(z) - \Sigma_\alpha(z)^\dagger\right), \quad \alpha \in \mathcal{S}, \tag{2.73}$$

are left undefined. This is to be expected, because the effects of the phase-breaking scattering events on the charge carrier fluctuations as modeled by the self-energy *must* depend on the scattering mechanism under consideration, and hence are problem specific. Further, the actual coupling strength will usually be influenced by the energy distribution of the charge carriers in the device, which means that the Green's function $\tilde{\mathcal{G}}(z)$ of the device should enter instead of the fictitious decoupled one. In summary, an additional way to obtain the scattering self-energy particularly suited for the problem at hand is necessary. The important case of electron-phonon interaction will be discussed in sections 2.3.2 to 2.3.4.

The transmission probabilities (2.71) between the various terminals now merely are constituents of the "effective transmission," an auxiliary construct which is used to quantify the charge carrier transition from one (real) lead into another. As is consistent with the origins of the KKR formalism, its value is computed by means of

[13] For a more thorough discussion on how this may be achieved we refer to appendix A.5.

[14] The very same reasoning also applies to the method of decoupling potentials presented in the subsection on the lead self-energy of section 2.2.3.

multiple scattering theory: A charge carrier may traverse the device without being scattered at all, or being scattered once, or twice, and so forth [35, 124]:

$$T_{LR}^{\text{eff}}(z) = T_{LR}(z) + \sum_{\alpha\in\mathcal{S}} \frac{T_{L\alpha}(z)T_{\alpha R}(z)}{S_\alpha(z)} + \sum_{\alpha,\beta\in\mathcal{S}}^{\beta\neq\alpha} \frac{T_{L\alpha}(z)T_{\alpha\beta}(z)T_{\beta R}(z)}{S_\alpha(z)S_\beta(z)} + \dots \tag{2.74}$$

In this equation, the denominator

$$S_\alpha(z) = T_{\alpha L}(z) + T_{\alpha R}(z) + \sum_{\beta\in\mathcal{S}}^{\beta\neq\alpha} T_{\alpha\beta}(z), \quad \alpha\in\mathcal{S}, \tag{2.75}$$

can be thought of as a renormalization of the probability measure ensuring charge carrier and energy conservation.[15]

While representation (2.74) could in principle be used to study the typical scattering orders in various material systems, it is "uncomfortable" in case one is only interested in the real physical situation, i.e., the limit of infinitely many allowed scattering events. Then, it is favorable to transform this equation to the equivalent[16] matrix representation

$$T_{LR}^{\text{eff}}(z) = T_{LR}(z) + \underline{T}_L(z)\left(\mathbb{1} - \underline{\underline{\tilde{T}}}(z)\right)^{-1}\underline{\tilde{T}}_R(z) \tag{2.76}$$

with the row vector $\underline{T}_L \equiv \{T_{L\alpha}\}_{\alpha\in\mathcal{S}}$, the column vector $\underline{\tilde{T}}_R \equiv \{{}^{T_{\alpha R}}\!/_{S_\alpha}\}_{\alpha\in\mathcal{S}}^{\mathrm{T}}$, as well as the matrix $\underline{\underline{\tilde{T}}} \equiv \{{}^{T_{\alpha\beta}}\!/_{S_\alpha}\}_{\alpha,\beta\in\mathcal{S}}$. A similar analysis would also yield the formula

$$\underline{f}(z) = \left(\mathbb{1} - \underline{\underline{\tilde{T}}}(z)\right)^{-1}\underline{f}^{(0)}(z), \quad f_\alpha^{(0)} \equiv \frac{T_{\alpha L}}{S_\alpha}f_L + \frac{T_{\alpha R}}{S_\alpha}f_R, \quad \alpha\in\mathcal{S}, \tag{2.77}$$

for the unknown distribution functions in the virtual terminals.

Given the effective transmission, the necessary relations for j_{LR} and R_{LR} in the case of phase-breaking scattering events in the device region are now obtained by substituting T_{LR}^{eff} for T_{LR} in all formulae derived at the end of section 2.2.1, which is true because equation (A.40) is structurally equivalent to equation (2.68). To accentuate this point and for future reference this is exemplified by

$$R_{LR} = \frac{2\,(\mu_L - \mu_R)}{G_0 \int_{\mathbb{R}} \mathrm{d}E\; T_{LR}^{\text{eff}}(E)\big(f_L(E) - f_R(E)\big)\cdot A} \tag{2.78a}$$

$$\xrightarrow[\kappa\left(T_{LR}^{\text{eff}}\right)\to 0]{\Delta\mu\to 0} \frac{2}{G_0\cdot T_{LR}^{\text{eff}}(E_F)\cdot A}, \tag{2.78b}$$

where the "curvature" κ of $T_{LR}^{\text{eff}}(E)$ is yet again used in the sense of appendix A.4.

[15] See appendix A.6 for a more detailed discussion.

[16] Please note that $T_{\alpha\alpha}(z) \equiv 0, \alpha\in\mathcal{S}$, has been chosen to simplify notation. For a more detailed derivation of equation (2.76) see the closing part of appendix A.6.

2.2.3. KKR Representation

Similarly to the approach used in section 2.1 on the electronic structure, the introduction to the NEGF formalism given in the subsections 2.2.1 and 2.2.2 is independent of a special choice of basis set. In the following, the peculiarities appearing whilst implementing these equations in an angular momentum representation, specifically into a KKR Green's function code, are discussed.

Lead Self-energy

In contrast to other methods it is, within the KKR formalism, possible to solve the Green's function of the coupled Hamiltonian $\mathcal{H}_\mathrm{c}$ by means of the so-called decimation technique [22]. A problem, on the other hand, pose the isolated subsystems, because the previously defined coupling potentials $\mathcal{V}_\mathrm{c}$ are in fact not accessible [32, 36, 64, 69]. Instead, "*de*coupling potentials" in the sense of references [70] and [71], i.e., strongly repulsive localized potentials, are introduced:

$$\mathcal{V}_\mathrm{dc} = \begin{pmatrix} \mathcal{V}_L & 0 & 0 \\ 0 & \mathcal{V}_M & 0 \\ 0 & 0 & \mathcal{V}_R \end{pmatrix}. \tag{2.79}$$

Assuming there exists a $\mathcal{V}_\mathrm{dc}$ such that $\mathcal{H}_\mathrm{dc} = \mathcal{H}_\mathrm{c} + \mathcal{V}_\mathrm{dc}$, then a Dyson's equation $\mathcal{G}_\mathrm{c} = \mathcal{G}_\mathrm{dc} - \mathcal{G}_\mathrm{dc}\mathcal{V}_\mathrm{dc}\mathcal{G}_\mathrm{c}$ is valid, and with $\mathcal{G}_\mathrm{dc}(z) = (z\mathbb{1} - \mathcal{H}_\mathrm{dc})^{-1}$ this yields[17]

$$\begin{pmatrix} \mathcal{G}_{LL} & \mathcal{G}_{LM} & \mathcal{G}_{LR} \\ \mathcal{G}_{ML} & \mathcal{G}_{MM} & \mathcal{G}_{MR} \\ \mathcal{G}_{RL} & \mathcal{G}_{RM} & \mathcal{G}_{RR} \end{pmatrix} = \begin{pmatrix} \mathcal{G}_L - \mathcal{G}_L\mathcal{V}_L\mathcal{G}_{LL} & -\mathcal{G}_L\mathcal{V}_L\mathcal{G}_{LM} & -\mathcal{G}_L\mathcal{V}_L\mathcal{G}_{LR} \\ -\mathcal{G}_M\mathcal{V}_M\mathcal{G}_{ML} & \mathcal{G}_M - \mathcal{G}_M\mathcal{V}_M\mathcal{G}_{MM} & -\mathcal{G}_M\mathcal{V}_M\mathcal{G}_{MR} \\ -\mathcal{G}_R\mathcal{V}_R\mathcal{G}_{RL} & -\mathcal{G}_R\mathcal{V}_R\mathcal{G}_{RM} & \mathcal{G}_R - \mathcal{G}_R\mathcal{V}_R\mathcal{G}_{RR} \end{pmatrix}. \tag{2.80}$$

Obviously, for *arbitrary* Green's functions $\mathcal{G}_\mathrm{c}(z)$ there is no such $\mathcal{V}_\mathrm{dc}$, but as long as only the correct $\mathcal{G}_{MM}(z)$ is necessary for the calculations, as in the present case, the only condition on $\mathcal{V}_\mathrm{dc}$ is to fulfill Dyson's equation

$$\begin{aligned} \mathcal{G}_{MM}(z) &= \mathcal{G}_M(z) - \mathcal{G}_M(z)\mathcal{V}_M\mathcal{G}_{MM}(z) \\ &= \mathcal{G}_M(z) - \mathcal{G}_M(z)\mathcal{V}_M\mathcal{G}_M(z) + \mathcal{G}_M(z)\mathcal{V}_M\mathcal{G}_M(z)\mathcal{V}_M\mathcal{G}_{MM}(z) \\ &= \mathcal{G}_M(z) + \mathcal{G}_M(z)\big(\Sigma_L(z) + \Sigma_R(z)\big)\mathcal{G}_{MM}(z), \end{aligned} \tag{2.81}$$

where the second equation is obtained by iterating once, and the third is a consequence of equation (2.62). Particularly, $\mathcal{V}_L$ and $\mathcal{V}_R$ remain arbitrary in the sense that they do not affect $\mathcal{G}_{MM}(z)$ at all. Now, if $\mathcal{V}_M \equiv \mathcal{V}_{M_L} + \mathcal{V}_{M_R}$ is chosen in such a manner that it exhibits the properties (written schematically) [69]

$$\text{(I)} \quad \mathbb{1} \ll \mathcal{V}_M\mathcal{G}_{MM}(z), \tag{2.82a}$$

$$\text{(II)} \quad \mathcal{V}_{M_L}\mathcal{G}_M\mathcal{V}_{M_R} + \mathcal{V}_{M_R}\mathcal{G}_M\mathcal{V}_{M_L} \ll \mathcal{V}_{M_L}\mathcal{G}_M\mathcal{V}_{M_L} + \mathcal{V}_{M_R}\mathcal{G}_M\mathcal{V}_{M_R}, \tag{2.82b}$$

then Dyson's equation (2.81) is valid with the self-energy definition

$$\Sigma_X(z) \equiv \mathcal{V}_{M_X}\mathcal{G}_M(z)\mathcal{V}_{M_X}, \quad X \in \{L, R\}. \tag{2.83}$$

[17] For the sake of readability, the parametric energy dependence has been dropped here.

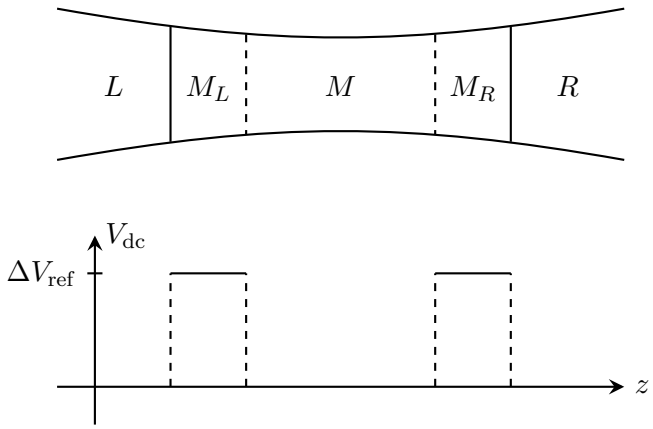

Figure 2.2.: Partitioning of the system in middle region M as well as left and right leads L and R, respectively. The artificial separation is realized by using the difference to the reference potential ΔV_{ref} as a decoupling potential in the self-energy regions $M_X, X \in \{L, R\}$.

The physical reasoning behind these assumptions is to make sure that there are no direct interactions between the leads, which means that the self-energies are additive. While inequality (I) is certainly granted if the decoupling potentials are chosen appropriately high, the second condition may be guaranteed if the overlap of $\mathcal{V}_{M_L}$ and $\mathcal{V}_{M_R}$ is negligible and, in addition, both are wide enough [32, 69].

Notably, the difference $\Delta\mathcal{V}_{\mathrm{ref}}$ of the device potential to the repulsive reference potential used in the screened KKR formalism is a valid decoupling potential if the transport geometry is divided as depicted in figure 2.2. Given that the structure constants of the reference Green's function $\mathcal{G}_{\mathrm{ref}}(z)$ decay exponentially in space, it is sufficient to restrict both M_L and M_R to a rather small amount of boundary layers. To simplify notation the lead subsystems L and R are in the following redefined to coincide with these device regions. Thus, within this work the lead self-energies are assumed to be

$$\Sigma_X(z) = \Delta\mathcal{V}_{\mathrm{ref}}\mathcal{G}_{\mathrm{ref}}(z)\Delta\mathcal{V}_{\mathrm{ref}} \cdot \mathbb{1}_X, \quad X \in \{L, R\}. \tag{2.84}$$

While the above equations are concerned with the decoupling a system M free of scattering, the same procedure is valid in the case of phase-breaking interactions in the device as well. Following the closing remarks of appendix A.5, the system would be separated in the disjoint subsystems L, R and $\tilde{M}$, and one would assume that there exists a decoupling potential analogous to (2.79) such that $\tilde{\mathcal{H}}_{\mathrm{dc}} = \tilde{\mathcal{H}}_{\mathrm{c}} + \tilde{\mathcal{V}}_{\mathrm{dc}}$, where

$$\tilde{\mathcal{V}}_{\mathrm{dc}} = \begin{pmatrix} \mathcal{V}_L & 0 & 0 \\ 0 & \mathcal{V}_{\tilde{M}} & 0 \\ 0 & 0 & \mathcal{V}_R \end{pmatrix}, \quad \tilde{\mathcal{H}}_{\mathrm{dc}} = \begin{pmatrix} \mathcal{H}_L & 0 & 0 \\ 0 & \mathcal{H}_{\tilde{M}} & 0 \\ 0 & 0 & \mathcal{H}_R \end{pmatrix}. \tag{2.85}$$

Proceeding similarly to the previous case and comparing the analog of equation (2.81) with (A.34b) demonstrates that the self-energy once again takes the shape of

(2.84). However, care must be taken to ensure that the scattering region $\mathcal{S} \subset \tilde{M}$ is well separated from $X \equiv \tilde{M}_X$. This is true because (a subset of) the charge moments in X are perpetuated to yield the charge moments in the leads, and given that the leads are considered to be free of scattering, these entities should not contain any effects of the Büttiker probes connected to the device.

Green's Function Including Phase-breaking Scattering Events

As discussed in section 2.2.2, if phase-breaking scattering events shall be considered in the transport calculations, then the coupled Green's function of the device has to take the effects of scattering into account. It is elucidated in appendix A.5 that this may be done by an additional scattering self-energy $\Sigma_{\text{scat}}(z)$, formally originating from the virtual Büttiker probes. Now it will be shown why, even though the traditional KKR formalism was concerned with real atomic potentials only, the beforementioned calculational scheme is suited to (approximately) handle such self-energies.

Obviously, both the free Green's function as well as the screened reference Green's function may be calculated regardless of the self-energy, as these systems are to be considered free of scattering. In accordance with the origins of the KKR formalism, i.e., multiple scattering theory, every atom is reckoned to be a scattering center for all phase-breaking scattering events under consideration, and hence each atom $n \in \mathcal{S}$ in the scattering region is "connected" to exactly one Büttiker probe associated with the self-energy $\Sigma^n_{\text{scat}}(z)$. Assuming further that this self-energy is not only site-diagonal but constant within a muffin-tin sphere, it is possible to relate the scattering-free isolated muffin-tin Hamiltonian to its "full" counterpart by $\tilde{\mathcal{H}}^n(z) = \mathcal{H}^n + \Sigma^n_{\text{scat}}(z)$ in a particularly simple manner, because then the corresponding eigenvalue problem reads

$$\mathcal{H}^n \left|\tilde{\psi}^n(z)\right\rangle = \left(z\mathbb{1} - \Sigma^n_{\text{scat}}(z)\right) \left|\tilde{\psi}^n(z)\right\rangle . \tag{2.86}$$

Comparing this to the eigenvalue problem of the unperturbed system $\mathcal{H}^n$ thus reveals that the scattering solutions including phase-breaking scattering events exist and may be calculated by a complex energy shift [124]

$$\underline{\tilde{X}}^n(r,z) = \begin{cases} \underline{X}^n(r, z - \Sigma^n_{\text{scat}}(z)) & \text{if } n \in \mathcal{S}, \\ \underline{X}^n(r,z) & \text{otherwise} \end{cases} \quad \text{for } X \in \{R, H\}. \tag{2.87}$$

The remaining task is to ensure the validity of the algebraic and single-site Dyson's equations (2.54) and (2.52), respectively. Studying the proof of the latter reveals no restrictions to purely real potentials [124]. Hence,

$$\tilde{g}^n(\underline{r}, \underline{r}', z) = -i\sqrt{z}\underline{\tilde{R}}^n(\wedge(\underline{r}, \underline{r}'), z)\underline{\tilde{H}}^n(\vee(\underline{r}, \underline{r}'), z)^{\times}. \tag{2.88}$$

The validity of the algebraic Dyson's equation is granted by noting that

1. the Lippmann-Schwinger equation for the isolated muffin-tin potential (2.48) is a special case of the general Lippmann-Schwinger equation discussed in appendix A.2, which is valid for self-energies as above, and that

2. the proof of the Lippmann-Schwinger-like equation (2.53) only requires the semi-separability of g^n as well as a spherically symmetric potential.[18]

Finally, the formula for the transition operator components (2.55) is valid if the logarithmic derivatives of the "full" scattering solutions are used. Therefore, the coupled Green's function of the device including phase-breaking scattering [124]

$$\tilde{G}(\underline{r}+\underline{R}_n,\underline{r}'+\underline{R}_{n'},z)=\delta_{nn'}\tilde{g}^n(\underline{r},\underline{r}',z)+\underline{\tilde{R}}^n(\underline{r},z)\underline{\underline{\tilde{G}}}^{nn'}(z)\underline{\tilde{R}}^{n'}(\underline{r}',z)^{\times} \tag{2.89}$$

may be calculated in the usual manner.

Please note, that the described procedure is a so-called "one-shot approximation:" To accurately mimic the physical situation, the coupled Green's function containing phase-breaking scattering would have to be calculated self-consistently with the scattering self-energy, because the scattering processes will lead to a renormalization of the electronic structure, which in turn will influence the mutual interactions of the particles [34, 72, 73]. This effect was, however, not considered in the calculations reported within this work, i.e., the self-consistency was performed in an equilibrium situation using supercells without any scattering self-energy contribution. This path was taken for several reasons:

First, the calculations presented within this work address the electron-phonon coupling as sole[19] phase-breaking scattering event. Given that the phonon eigenenergies are of the order of several 10 meV and hence much smaller than the corresponding electronic eigenenergies, the renormalization is assumed to be rather small. In fact, Migdal's theorem [72, 74] proves that the renormalization is of the order $M^{-1/2}$, with M being the ion mass.

Second, although it is possible to calculate the Green's function including a self-energy, the charge density necessary for the self-consistent DFT cycle is generally not calculable using equation (2.29): As the Hamiltonian fails to be hermitian, the eigenenergies won't be purely real, and hence the Cauchy principal value will not cancel in equation (2.25). In contrast, the non-equilibrium density formula (2.66) would still be valid if all additional terms corresponding to the scattering self-energy were added. Given, on the other hand, that this relation is only valid in the limit of real energy arguments, a very dense mesh would be necessary to accurately sample the highly structured integrand in the energy integration for the charge density.[20] Considering that the renormalization is small this computationally demanding task is assumed dispensable.

Last, the electron-phonon self-energy used in the presented calculations is not calculated within the KKR code itself, but employing third party codes. Hence, there is no mechanism to update the self-energy using the "full" Green's function

[18] For hints on whether it is possible to generalize to "full-potential" calculations, please see the discussion in the outlook (chapter 4).

[19] The electron-electron interaction is treated on the DFT level, i.e., we are considering the "Kohn-Sham-quasiparticle-phonon coupling," actually. Further, the scattering at the device boundaries is contained in the lead self-energies and is hence not considered, either.

[20] See equation (2.20) as well as the discussion regarding the benefits of equation (2.29).

$\tilde{\mathcal{G}}(z)$, which would introduce another inconsistency in the self-consistency cycle. As there is no obvious reason why this approximation should be superior to completely neglecting the phonon renormalizations, we refrain from doing so.

Transmission Formulae

The KKR representation of the general transmission formula (2.71) is obtained in great similarity to what is described by Franz, Czerner, and Heiliger [32] in the case of coherent transport: Projecting the operator identity to real space yields[21]

$$\begin{aligned} T_{XY}(z) = \int_Y \mathrm{d}^3 r_1 \int_Y \mathrm{d}^3 r_2 \int_X \mathrm{d}^3 r_3 \int_X \mathrm{d}^3 r_4 \; \Gamma_Y(\underline{r}_1, \underline{r}_2, z) \tilde{G}(\underline{r}_2, \underline{r}_3, z) \cdot \\ \cdot \, \Gamma_X(\underline{r}_3, \underline{r}_4, z) \tilde{G}(\underline{r}_1, \underline{r}_4, z)^*, \end{aligned} \tag{2.90}$$

where $X \equiv \tilde{M}_X$ in the sense of the subsection on the lead self-energy of section 2.2.3 denotes the domain defined by $\Gamma_X(z)$ being nonzero upon; Y analogously. Segmenting the spatial degrees of freedom in muffin-tin spheres V_{MT} and inserting the coupled Green's function (2.89) of the device including phase-breaking scattering leads to

$$\begin{aligned} T_{XY}(z) = \sum_{\substack{nn' \in Y \\ mm' \in X}} \int_{V^n_{\mathrm{MT}}} \mathrm{d}^3 r_1 \int_{V^{n'}_{\mathrm{MT}}} \mathrm{d}^3 r_2 \int_{V^m_{\mathrm{MT}}} \mathrm{d}^3 r_3 \int_{V^{m'}_{\mathrm{MT}}} \mathrm{d}^3 r_4 \; \Gamma_Y^{nn'}(\underline{r}_1, \underline{r}_2, z) \underline{\tilde{R}}^{n'}(\underline{r}_2, z) \underline{\underline{\tilde{G}}}^{n'm}(z) \cdot \\ \cdot \, \underline{\tilde{R}}^{m}(\underline{r}_3, z)^{\times} \Gamma_X^{mm'}(\underline{r}_3, \underline{r}_4, z) \underline{\tilde{R}}^{n}(\underline{r}_1, z)^* \underline{\underline{\tilde{G}}}^{nm'}(z)^* \underline{\tilde{R}}^{m'}(\underline{r}_4, z)^{\times *}. \end{aligned} \tag{2.91}$$

Here it was exploited that $X \cap Y = \varnothing$, i.e., that the overlap of both domains vanishes, which allows for the neglect of the "single-scattering contribution" $\delta_{nn'} \tilde{g}^n(\underline{r}, \underline{r}', z)$ to the Green's function. For the domains L and R of the real leads broadening functions this is true by construction of the corresponding self-energies (2.84), in the case of Büttiker probes this condition will be enforced by a suitable choice of the scattering region $\mathcal{S} \subset \tilde{M}$. Note, however, that this assumption explicitly rules out the incorporation of scattering events in the leads.

One of the most prominent features of the "multi-scattering contribution" to the Green's function, namely that the spatial variables are separated, allows to further simplify this relation: With the definition of the broadening matrix of the first kind

$$\underset{=X}{\overrightarrow{\gamma}}^{nn'}(z) \equiv \int_{V^n_{\mathrm{MT}}} \mathrm{d}^3 r \int_{V^{n'}_{\mathrm{MT}}} \mathrm{d}^3 r' \; \underline{\tilde{R}}^{n}(\underline{r}, z)^{\times} \Gamma_X^{nn'}(\underline{r}, \underline{r}', z) \underline{\tilde{R}}^{n'}(\underline{r}', z)^{-}, \tag{2.92}$$

where the superscript notation $- \equiv \times * \mathrm{T} = \times \dagger$ was introduced, it is seen that[22]

$$\begin{aligned} T_{XY}(z) = \sum_{\substack{nn' \in Y \\ mm' \in X}} \int_{V^n_{\mathrm{MT}}} \mathrm{d}^3 r_1 \int_{V^{n'}_{\mathrm{MT}}} \mathrm{d}^3 r_2 \; \Gamma_Y^{nn'}(\underline{r}_1, \underline{r}_2, z) \underline{\tilde{R}}^{n'}(\underline{r}_2, z) \underline{\underline{\tilde{G}}}^{n'm}(z) \cdot \\ \cdot \, \underset{=X}{\overrightarrow{\gamma}}^{mm'}(z) \underline{\underline{\tilde{G}}}^{mm'}(z)^{\dagger} \underline{\tilde{R}}^{n}(\underline{r}_1, z)^{\dagger}. \end{aligned} \tag{2.93}$$

[21] To simplify the notation, the limit towards real energy arguments has been temporarily omitted.

[22] The last three factors of this matrix-vector product have been substituted by their transposed equivalent in order to use this definition.

Finally, because of $\underline{a} \cdot \underline{\underline{M}} \cdot \underline{b}^\dagger = \mathrm{Tr}\left[\underline{b}^\dagger \underline{a} \cdot \underline{\underline{M}}\right]$ for arbitrary vectors $\underline{a}, \underline{b}$ and matrices $\underline{\underline{M}}$ having suitable dimensions, we find for the transmission probability from terminal X to Y that

$$T_{XY}(E) = \lim_{\mathrm{Im}\, z \downarrow 0} \sum_{\substack{nn' \in Y \\ mm' \in X}} \mathrm{Tr}\left[\overleftarrow{\underline{\underline{\gamma}}}_{Y}^{nn'}(z) \underline{\underline{\tilde{G}}}^{n'm}(z) \overrightarrow{\underline{\underline{\gamma}}}_{X}^{mm'}(z) \underline{\underline{\tilde{G}}}^{mm'}(z)^\dagger\right] \tag{2.94}$$

with the broadening matrix of the second kind

$$\overleftarrow{\underline{\underline{\gamma}}}_{X}^{nn'}(z) \equiv \int_{V_{\mathrm{MT}}^n} \mathrm{d}^3 r \int_{V_{\mathrm{MT}}^{n'}} \mathrm{d}^3 r' \; \underline{\underline{\tilde{R}}}^{n}(\underline{r}, z)^\dagger \Gamma_X^{nn'}(\underline{r}, \underline{r}', z) \underline{\underline{\tilde{R}}}^{n'}(\underline{r}', z). \tag{2.95}$$

The coherent part of the transmission, i.e., the probability of a charge carrier to transmit from the left lead to the right lead without being scattered, may now be obtained using equation (2.94) after the broadening matrices (2.92) and (2.95) have been calculated. Revisiting that the domains L and R must not contain any Büttiker probes for equation (2.91) to be valid, it is seen from (2.87) that the corresponding scattering solutions $\underline{\underline{\tilde{R}}}$ reduce to their "free" counterpart $\underline{\underline{R}}$, and hence these matrices are exactly the same as those defined in reference [32]. Therefore, all considerations regarding an efficient evaluation of these quantities given there apply.

Nevertheless, the transmission probability is reduced compared to the case free of scattering, because the structure constants $\underline{\underline{\tilde{G}}}^{nn'}(z)$ containing the effects of the Büttiker probes enter in the calculations instead of $\underline{\underline{G}}^{nn'}(z)$. The physical analog to this mathematical reasoning is the intuitive expectation, that the probability of an electron to remain unscattered while transmitting from left to right becomes smaller if either device length or scattering rate (or both) increase. The coherent contribution to the effective transmision will consequently be important especially in short systems at low temperatures.

As all systems considered within this work show translational invariance orthogonal to the transport direction, this is true for the broadening matrices as well as the structure constants. To exploit this feature in the calculations, the multi-index n numerating the muffin-tin volumes V_{MT} is split into an in-plane component, yet again denoted n, and an out-of-plane index ν. Then, a lattice Fourier transform

$$f_{nn'}^{\nu\nu'}(z) = \frac{\Omega}{(2\pi)^2} \int_{\mathrm{SBZ}} \mathrm{d}^2 k \; \mathrm{e}^{i\underline{k}\left(\underline{R}_n - \underline{R}_{n'}\right)} f^{\nu\nu'}(\underline{k}, z) \tag{2.96}$$

of equation (2.94) with respect to the in-plane difference $n - n'$ yields

$$T_{LR}(E) = \lim_{\mathrm{Im}\, z \downarrow 0} \int_{\mathrm{SBZ}} \mathrm{d}^2 k \sum_{\substack{\nu\nu' \in R \\ \mu\mu' \in L}} \mathrm{Tr}\left[\overleftarrow{\underline{\underline{\gamma}}}_{R}^{\nu\nu'}(\underline{k}, z) \underline{\underline{\tilde{G}}}^{\nu'\mu}(\underline{k}, z) \overrightarrow{\underline{\underline{\gamma}}}_{L}^{\mu\mu'}(\underline{k}, z) \underline{\underline{\tilde{G}}}^{\nu\mu'}(\underline{k}, z)^\dagger\right]. \tag{2.97}$$

The incoherent part of the transmission consists of all those charge carrier transitions that were subject to phase-breaking scattering events in the device, and

according to equation (2.74) this contribution is the weighted sum of all those scattering paths originating in the left lead and terminating in the right which were taking a detour over at least one virtual terminal. To calculate these transmission probabilities, the broadening matrices of all Büttiker probes $\alpha \in \mathcal{S}$ must be evaluated first, and in conformance with the considerations in the subsection on the Green's function including phase-breaking scattering events of section 2.2.3 we will assume that the corresponding self-energy takes the form[23]

$$\Sigma^{\nu\nu'}_{\mathrm{scat},nn'}(\underline{r},\underline{r}',z) = \sum_{\alpha\in\mathcal{S}} \Sigma^{\nu\nu'}_{\alpha,nn'}(\underline{r},\underline{r}',z) = \sum_{\alpha\in\mathcal{S}} \delta_{nn'}\delta_{\nu\nu'}\delta(\underline{r}-\underline{r}')\delta_{\nu\alpha}\Sigma^{\alpha}_{\mathrm{scat}}(z). \tag{2.98}$$

The broadening functions as defined by (2.73) may then be inserted in the general definitions (2.92) and (2.95), respectively, thus proving that both kinds of broadening matrices are equal for self-energies constant[24] in a muffin-tin sphere:

$$\begin{aligned}
\overleftarrow{\underline{\underline{\gamma}}}^{\nu\nu'}_{\alpha,nn'}(z) &= \int_{V^{\nu}_{\mathrm{MT}}} \mathrm{d}^3 r \int_{V^{\nu'}_{\mathrm{MT}}} \mathrm{d}^3 r' \; \underline{\tilde{R}}^{\nu}(\underline{r},z)^{\dagger}\delta_{nn'}\delta_{\nu\nu'}\delta(\underline{r}-\underline{r}')\delta_{\nu\alpha}\Gamma^{\alpha}_{\mathrm{scat}}(z)\underline{\tilde{R}}^{\nu'}(\underline{r}',z) \\
&= \delta_{nn'}\delta_{\nu\nu'}\delta_{\nu\alpha} \int_{V^{\alpha}_{\mathrm{MT}}} \mathrm{d}^3 r \; \underline{\tilde{R}}^{\alpha}(\underline{r},z)^{\dagger}\Gamma^{\alpha}_{\mathrm{scat}}(z)\underline{\tilde{R}}^{\alpha}(\underline{r},z) \\
&= \delta_{nn'}\delta_{\nu\nu'}\delta_{\nu\alpha} \int_{V^{\alpha}_{\mathrm{MT}}} \mathrm{d}^3 r \; \underline{\tilde{R}}^{\alpha}(\underline{r},z)^{\times}\Gamma^{\alpha}_{\mathrm{scat}}(z)\underline{\tilde{R}}^{\alpha}(\underline{r},z)^{-} \\
&= \overrightarrow{\underline{\underline{\gamma}}}^{\nu\nu'}_{\alpha,nn'}(z).
\end{aligned} \tag{2.99}$$

Given that the self-energy as defined above preserves the in-plane translational invariance of the system under consideration, the net current flow will be in transport direction only. This quasi-one-dimensional transmission situation may therefore be modeled by gathering all virtual terminals in each plane in a kind of "super-terminal," and subsequently calculating the transmission probabilities between these planes. As for the coherent contribution, this idea is formally equivalent to perform an in-plane lattice Fourier transform. Hence, for all super-terminals $\alpha, \beta \in \mathcal{S}$ we find

$$T_{L\alpha}(E) = \lim_{\mathrm{Im}\, z\downarrow 0} \int_{\mathrm{SBZ}} \mathrm{d}^2 k \sum_{\mu\mu'\in L} \mathrm{Tr}\left[\underline{\underline{\gamma}}^{\alpha}_{\mathrm{scat}}(z)\underline{\underline{\tilde{G}}}^{\alpha\mu}(\underline{k},z)\overrightarrow{\underline{\underline{\gamma}}}^{\mu\mu'}_{L}(\underline{k},z)\underline{\underline{\tilde{G}}}^{\alpha\mu'}(\underline{k},z)^{\dagger}\right], \tag{2.100a}$$

$$T_{\alpha R}(E) = \lim_{\mathrm{Im}\, z\downarrow 0} \int_{\mathrm{SBZ}} \mathrm{d}^2 k \sum_{\nu\nu'\in R} \mathrm{Tr}\left[\overleftarrow{\underline{\underline{\gamma}}}^{\nu\nu'}_{R}(\underline{k},z)\underline{\underline{\tilde{G}}}^{\nu'\alpha}(\underline{k},z)\underline{\underline{\gamma}}^{\alpha}_{\mathrm{scat}}(z)\underline{\underline{\tilde{G}}}^{\nu\alpha}(\underline{k},z)^{\dagger}\right], \tag{2.100b}$$

$$T_{\alpha\beta}(E) = \lim_{\mathrm{Im}\, z\downarrow 0} \int_{\mathrm{SBZ}} \mathrm{d}^2 k \;\; \mathrm{Tr}\left[\underline{\underline{\gamma}}^{\beta}_{\mathrm{scat}}(z)\underline{\underline{\tilde{G}}}^{\beta\alpha}(\underline{k},z)\underline{\underline{\gamma}}^{\alpha}_{\mathrm{scat}}(z)\underline{\underline{\tilde{G}}}^{\beta\alpha}(\underline{k},z)^{\dagger}\right], \tag{2.100c}$$

[23] Notably, the transport formalism would allow for an $\underline{r}$-dependent self-energy (in particular, the lead self-energies are dependent on both $\underline{r}$ and $\underline{r}'$), but in this case the relation (2.87) would not be valid, and hence the scattering solutions including the self-energy contribution would have to be solved otherwise. For simplicity, we will specialize here to the case relevant for the presented calculations.

[24] Slightly more general, a purely radial dependence on the spatial variable is sufficient.

where the broadening matrix

$$\underline{\underline{\gamma}}^{\alpha}_{\mathrm{scat}}(z) \equiv \int_{V^{\alpha}_{\mathrm{MT}}} \mathrm{d}^3 r \; \underline{\tilde{R}}^{\alpha}(\underline{r}, z)^{\dagger} \Gamma^{\alpha}_{\mathrm{scat}}(z) \underline{\tilde{R}}^{\alpha}(\underline{r}, z) = \left\{ \delta_{LL'} \Gamma^{\alpha}_{\mathrm{scat}}(z) \left\| |\tilde{R}^{\alpha}_{L}(z)\rangle \right\|^2 \right\}_{LL'} \tag{2.101}$$

has been defined. After these quantities have been evaluated, the effective transmission is readily obtained by means of equation (2.76).

2.3. Electron-phonon Coupling

In order to employ the theoretical results of the last section, the electron-phonon self-energy (2.72) has to be obtained in the purely energy-dependent representation (2.98) suitable to incorporate in the proposed KKR implementation. After a preliminary discussion of lattice dynamics, the derivation and evaluation of the self-energy formula are elucidated. Finally, a way to average this quantity over all contributing states to arrive at the desired representation is exemplified.

2.3.1. Lattice Dynamics

As discussed in the introduction to this chapter, after having solved equation (2.3) for the eigenenergies $E_{\alpha}(\{\underline{R}\})$ of the electronic system with fixed atom positions, the movement of the nuclei in Born-Oppenheimer approximation is given by the stationary Schrödinger-like equation [compare equation (2.4)]

$$\left(-\sum_{n=1}^{N_n} \frac{1}{M_n} \nabla^2_{\underline{R}_n} + E(\{\underline{R}\}) \right) \chi_{\alpha}(\{\underline{R}\}) = \mathcal{E} \chi_{\alpha}(\{\underline{R}\}), \tag{2.102}$$

where the effective potential $E(\{\underline{R}\})$ is taken to be the ground-state energy of the electronic subsystem in practice [20, 49]. In general this Born-Oppenheimer energy surface will depend on the atomic positions in a complicated manner. Nevertheless, if the system under consideration is stable, i.e., has a positive binding energy, there exists a set of equilibrium positions $\{\underline{R}^0\}$ such that $E(\{\underline{R}^0\})$ is minimal, and hence for small displacements $\{\underline{u}\}$ a harmonic approximation

$$E(\{\underline{R}^0 + \underline{u}\}) \approx E(\{\underline{R}^0\}) + \frac{1}{2} \sum_{nn'} \underline{u}^{\mathrm{T}}_n \cdot \left(\nabla_{\underline{R}_n} \nabla^{\mathrm{T}}_{\underline{R}_{n'}} E(\{\underline{R}\}) \right) \Big|_{\{\underline{R}^0\}} \cdot \underline{u}_{n'} \tag{2.103}$$

is valid. The vanishing of the gradient $\underline{F}_n = -\nabla_{\underline{R}_n} E(\{\underline{R}^0\})$ at the critical point is, from a physical point of view, just the notion that in equilibrium all forces on the nuclei must be zero [20, 49]. Using Newton's second law $\underline{F}_n = M_n \underline{a}_n$ therefore yields the equation of motion [47]

$$M_n \ddot{\underline{u}}_n = -\nabla_{\underline{u}_n} E(\{\underline{R}^0 + \underline{u}\}) = -\sum_{n'} \left(\nabla_{\underline{R}_n} \nabla^{\mathrm{T}}_{\underline{R}_{n'}} E(\{\underline{R}\}) \right) \Big|_{\{\underline{R}^0\}} \cdot \underline{u}_{n'}. \tag{2.104}$$

This is the reason that the components of the Hessian matrix of the Born-Oppenheimer energy surface $E(\{\underline{R}^0\})$ are often termed "harmonic force constants" [20, 47, 49].

If further translational invariance with respect to some lattice vectors $\underline{R}_l^0$ may be assumed, it is beneficial to rewrite the positions of the nuclei as [20]

$$\underline{R}_n \to \underline{R}_{l\kappa} \equiv \underline{R}_{l\kappa}^0 + \underline{u}_{l\kappa} \equiv \underline{R}_l^0 + \underline{\tau}_\kappa + \underline{u}_{l\kappa}, \tag{2.105}$$

where $\underline{\tau}_\kappa$ is the basis vector of the κ-th atom in the unit cell. Then the ansatz [47]

$$\underline{u}_{l\kappa}(t) = \frac{1}{\sqrt{M_\kappa}}\, \underline{e}_\kappa(\underline{q}) \cdot \mathrm{e}^{i\left(\underline{q}\cdot\underline{R}_{l\kappa}^0 - \omega_{\underline{q}} t\right)} \tag{2.106}$$

produces the phonon eigenvalue equation [47, 49]

$$\sum_{\kappa'\alpha'} D_{\kappa\alpha,\kappa'\alpha'}(\underline{q}) e^\nu_{\kappa'\alpha'}(\underline{q}) = \omega^2_{\underline{q}\nu} e^\nu_{\kappa\alpha}(\underline{q}) \tag{2.107}$$

for the squared eigenfrequencies $\omega^2_{\underline{q}\nu}$ and polarization vectors $\underline{e}^\nu_\kappa(\underline{q})$ of a phonon mode ν having wave vector $\underline{q}$. In this relation the lattice Fourier transform of the mass-scaled harmonic force constants [20, 47, 49]

$$D_{\kappa\alpha,\kappa'\alpha'}(\underline{q}) = \frac{1}{\sqrt{M_\kappa M_{\kappa'}}} \sum_l \left.\frac{\partial^2 E(\{\underline{R}\})}{\partial R_{l\kappa\alpha}\partial R_{0\kappa'\alpha'}}\right|_{\{\underline{R}^0\}} \mathrm{e}^{-i\underline{q}\left(\underline{R}_{l\kappa}^0 - \underline{R}_{0\kappa'}^0\right)}, \tag{2.108}$$

i.e., the elements of the so-called dynamical matrix, emerges. The dimensions of the dynamical matrix depend only[25] on the number of basis atoms and are, in particular, independent of the macroscopic system size. Hence, equation (2.107) is a convenient way to obtain the phonon dispersion of a periodic solid necessary for the evaluation of the electron-phonon self-energy (2.139) derived in the next section.

2.3.2. Self-energy Formulae

In the following an expression for the scattering self-energy (2.72) formally originating from the Büttiker probes will be derived in the case of electron-phonon interactions. A systematic way to perform this task is the perturbative approach based on the Keldysh formulation of the non-equilibrium Green's function formalism in the context of quantum field theory [50, 51]. Hence, in a first step, an appropriate approximation to the non-relativistic condensed matter Hamiltonian (2.1) in second quantization is established, which will subsequently be used to state the non-equilibrium electron-phonon problem in terms of a contour-ordered Green's function. This quantity lends itself to an expansion in terms of the non-interacting electron and phonon Green's functions, leading to a Dyson's equation with a suitable self-energy approximation. Finally, the contour-time is transformed to energy domain, bringing forth a self-energy formula suitable to be evaluated using, e.g., (pseudopotential) plane-wave codes.

[25] It is assumed that the system and hence any displacement vector $\underline{u}$ is three-dimensional.

Condensed Matter Hamiltonian in Second Quantization

In accordance with the considerations of Born and Oppenheimer [48] it is assumed that the electronic system with *fixed* equilibrium nuclei positions $\{\underline{R}^0\}$ has been self-consistently solved in the framework of DFT, i.e., the effective potential

$$V_{\text{eff}}^{\{\underline{R}^0\}}(\underline{r}) = \sum_{l\kappa} V_{\text{eff}}^{\kappa}(\underline{r} - \underline{R}_{l\kappa}^0) \tag{2.109}$$

of the Kohn-Sham Hamiltonian (2.8) has been obtained as a superposition of the screened nuclei potentials [47, 75]. Now, if the lattice vibrations may be modeled as phonons, i.e., for small displacements $\{\underline{u}\}$ from the equilibrium positions $\{\underline{R}^0\}$, the effective potential with displaced nuclei may be written as [47, 75]

$$V_{\text{eff}}^{\{\underline{R}^0+\underline{u}\}}(\underline{r}) \approx V_{\text{eff}}^{\{\underline{R}^0\}}(\underline{r}) - \sum_{l\kappa} \nabla^{\mathrm{T}} V_{\text{eff}}^{\kappa}(\underline{r} - \underline{R}_{l\kappa}^0) \cdot \underline{u}_{l\kappa}. \tag{2.110}$$

Within these two approximations, the Hamiltonian of the electronic system accounting for electron-phonon coupling hence becomes [47]

$$\tilde{H}_{\text{e}} = H_{\text{KS}}^{\{\underline{R}^0\}} + \sum_{i=1}^{N_e} H_{\text{eph}}(\underline{r}_i). \tag{2.111}$$

Let $c_{n\underline{k}}^{(\dagger)}$ be the creation (annihilation) operator of a Kohn-Sham quasi-particle in state $|n\underline{k}\rangle$ of the phonon-free system, then the first term is diagonal. H_{eph}, on the other hand, has non-diagonal elements describing scattering between states[26] [47, 75]

$$\tilde{\mathcal{H}}_{\text{e}} = \sum_{n\underline{k}} \varepsilon_{n\underline{k}} c_{n\underline{k}}^{\dagger} c_{n\underline{k}} + \sum_{nm} \sum_{\underline{k}\underline{k}'} \langle m\underline{k}' \,|\, \mathcal{H}_{\text{eph}} \,|\, n\underline{k}\rangle \, c_{m\underline{k}'}^{\dagger} c_{n\underline{k}}, \tag{2.112}$$

where the matrix element in real-space representation may be expressed with the Kohn-Sham orbitals $\phi_{n\underline{k}}(\underline{r})$ as [47]

$$\langle m\underline{k}' \,|\, \mathcal{H}_{\text{eph}} \,|\, n\underline{k}\rangle = -\int \mathrm{d}^3 r \; \phi_{m\underline{k}'}^*(\underline{r}) \sum_{l\kappa} \nabla^{\mathrm{T}} V_{\text{eff}}^{\kappa}(\underline{r} - \underline{R}_{l\kappa}^0) \underline{u}_{l\kappa} \phi_{n\underline{k}}(\underline{r}). \tag{2.113}$$

Using the phonon creation (annihilation) operators $b_{\underline{q}\nu}^{(\dagger)}$ a generic displacement $\underline{u}_{l\kappa}$ may be written as a superposition of all possible phonon states, and in case of Born-von-Kármán boundary conditions in a system of N cells this leads to [47, 49, 75]

$$\underline{u}_{l\kappa} = \frac{1}{\sqrt{N}} \sum_{\underline{q}\nu} \sqrt{\frac{\hbar}{2M_\kappa \omega_{\underline{q}\nu}}} \left(b_{\underline{q}\nu} + b_{-\underline{q}\nu}^{\dagger} \right) \underline{e}_{\kappa}^{\nu}(\underline{q}) \mathrm{e}^{i\underline{q}\cdot\underline{R}_{l\kappa}^0}. \tag{2.114}$$

[26] Please note that in the electronic subsystem, the summation over spin indices was omitted. Neglecting the relativistic spin-orbit coupling, there is no coupling of the phonon system with the electron spin for metallic systems in normal-state [16]. For the sake of physical rigor one could, however, consider the spin-index σ included in the wave vector $\underline{\mathrm{k}}$.

Hence, by inserting this representation in equation (2.113), one arrives at [47, 49, 75]

$$\langle m\underline{k}' \,|\, \mathcal{H}_{\text{eph}} \,|\, n\underline{k}\rangle = \frac{1}{\sqrt{N}} \sum_{\underline{q}\nu} g^{\underline{q}\nu}_{m\underline{k}',n\underline{k}} \left(b_{\underline{q}\nu} + b^{\dagger}_{-\underline{q}\nu} \right) \tag{2.115}$$

with the definition of the electron-phonon vertex [47, 49, 75]

$$g^{\underline{q}\nu}_{m\underline{k}',n\underline{k}} \equiv \sum_{\kappa} \sqrt{\frac{\hbar}{2M_\kappa \omega_{\underline{q}\nu}}} \left\langle m\underline{k}' \,\middle|\, \delta^{\underline{q}\nu}_{\kappa} V^{\kappa}_{\text{eff}} \,\middle|\, n\underline{k} \right\rangle \tag{2.116}$$

and the first order variation of the effective potential of the κ-th nucleus with respect to the phonon mode ν having wave vector $\underline{q}$ [20, 49, 75]

$$\delta^{\underline{q}\nu}_{\kappa} V^{\kappa}_{\text{eff}}(\underline{r}) \equiv -\sum_{l} \nabla^{\mathrm{T}} V^{\kappa}_{\text{eff}}(\underline{r} - \underline{R}^0_{l\kappa}) \underline{e}^{\nu}_{\kappa}(\underline{q}) \mathrm{e}^{i\underline{q}\cdot\underline{R}^0_{l\kappa}}. \tag{2.117}$$

It can be shown that the electron-phonon vertex (2.116) is only non-zero if $\underline{k}' = \underline{k} + \underline{q}$, which of course ensures the conservation of momentum in the interaction of electrons and phonons [47]. Therefore, within the DFT approximation to the electron-electron interaction in conjunction with the harmonic approximation to the lattice vibrations the total Hamiltonian of the system in second quantization is given by the sum of the electric Hamiltonian (2.112) and the energy contribution $\mathcal{H}_{\text{ph}}$ of the "bare" phonons as [47, 75]

$$\begin{aligned} \tilde{\mathcal{H}} = &\sum_{n\underline{k}} \varepsilon_{n\underline{k}} c^{\dagger}_{n\underline{k}} c_{n\underline{k}} + \frac{1}{\sqrt{N}} \sum_{\underline{q}\nu} \sum_{nm\underline{k}} g^{\underline{q}\nu}_{m\underline{k}+\underline{q},n\underline{k}} \left(b_{\underline{q}\nu} + b^{\dagger}_{-\underline{q}\nu} \right) c^{\dagger}_{m\underline{k}+\underline{q}} c_{n\underline{k}} \\ &+ \sum_{\underline{q}\nu} \omega_{\underline{q}\nu} \left(b^{\dagger}_{\underline{q}\nu} b_{\underline{q}\nu} + \frac{1}{2} \right). \end{aligned} \tag{2.118}$$

Steady-state Non-equilibrium Problem

Given that the electron-phonon interaction may be considered a small perturbation, we will now describe a possible way to obtain a representation of the problem suitable for a perturbation expansion. Thus, prior to a for now arbitrary time t_0, the system is assumed to be in thermodynamic equilibrium with a reservoir having temperature T described by the Hamiltonian $\mathcal{H} = \mathcal{H}^{\{\underline{R}^0\}}_{\text{KS}} + \mathcal{H}_{\text{ph}}$, i.e., the system contains both electrons and phonons, but these species do not yet interact [see equation (2.118)]. Then, the corresponding statistical operator reads [50, 51]

$$n = \frac{\mathrm{e}^{-\beta\mathcal{H}}}{\mathrm{Tr}\left(\mathrm{e}^{-\beta\mathcal{H}}\right)}, \quad \beta \equiv \frac{1}{k_B T}, \tag{2.119}$$

where the trace is running over both electronic and phononic states.[27] At times $t > t_0$ the coupling between the electrons and phonons is "switched on," and thereafter the system is represented by the full Hamiltonian $\tilde{\mathcal{H}} = \mathcal{H} + \mathcal{H}_{\text{eph}}$.

[27] Please note the temperature dependence of the statistical operator, which is *always* present in the remainder of this section. However, due to the rather concise notation, it is usually not stated explicitly.

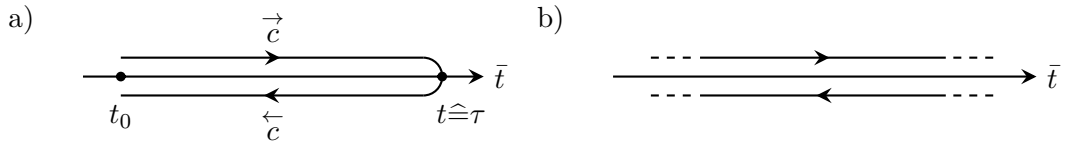

Figure 2.3.: a) Closed-time contour $c \equiv \overrightarrow{c} + \overleftarrow{c}$ and b) Schwinger-Keldysh contour K. Even though the forward and backward parts of the contours are drawn as if they were shifted into the complex time plane, they actually run on the real time axis.

Analogous to equation (2.24), the average value of an observable $\mathcal{O}$ in the Heisenberg picture with respect to the Hamiltonian $\tilde{H}$ is given by [50, 51]

$$\langle \mathcal{O}(t) \rangle = \mathrm{Tr}\left[n \mathcal{O}_{\tilde{\mathcal{H}}}(t) \right]. \tag{2.120}$$

Although a valid choice, in the following it is beneficial to use the interaction picture or, more precisely, the Heisenberg picture regarding $\mathcal{H}$, which may be related to the previously used Heisenberg picture as [50, 51]

$$\mathcal{O}_{\tilde{\mathcal{H}}}(t) = U^\dagger(t, t_0) \mathcal{O}_{\mathcal{H}}(t) U(t, t_0), \quad U(t, t') \equiv \mathcal{T}\, \mathrm{e}^{-i \int_{t'}^{t} \mathrm{d}\bar{t}\ \mathcal{H}_{\mathrm{eph}\mathcal{H}}(\bar{t})}, \tag{2.121}$$

where $\mathcal{T}$ is the conventional time-ordering operator. Considering further that [51]

$$U^\dagger(t, t') = \bar{\mathcal{T}}\, \mathrm{e}^{i \int_{t'}^{t} \mathrm{d}\bar{t}\ \mathcal{H}_{\mathrm{eph}\mathcal{H}}(\bar{t})} = \bar{\mathcal{T}}\, \mathrm{e}^{-i \int_{t}^{t'} \mathrm{d}\bar{t}\ \mathcal{H}_{\mathrm{eph}\mathcal{H}}(\bar{t})}, \tag{2.122}$$

with $\bar{\mathcal{T}}$ denoting the anti-time-ordering operator, it is seen that equation (2.121) may equally be stated as [50, 51]

$$\mathcal{O}_{\tilde{\mathcal{H}}}(t) = \mathcal{T}_c \left(\mathrm{e}^{-i \int_c \mathrm{d}\tau_1\ \mathcal{H}_{\mathrm{eph}\mathcal{H}}(\tau_1)} \mathcal{O}_{\mathcal{H}}(t) \right), \tag{2.123}$$

where the closed-time contour $c \equiv \overrightarrow{c} + \overleftarrow{c}$ depicted in figure 2.3 as well as the corresponding contour-ordering operator $\mathcal{T}_c$ have been introduced.

Using the composition of two such contours c and c' extending to t and t', respectively, it is further seen that this procedure may readily be generalized to averages over two operators. Because of the unitarity of the evolution operator, i.e., $U^\dagger(t_1, t_0) U(t_1, t_0) = \mathbb{1}$, the last part of the first contour cancels the beginning of the second, and hence this composition is equivalent to employing a contour extending to $t_m \equiv \max(t, t')$. Of course, the same argument allows for choosing $t_m \to +\infty$. Finally, as in this work we are not interested in any transient phenomena but in the steady-state only, it is further convenient to assume the initial time t_0 to reside infinitely in the past. Hence, in the following we will study the contour-ordered

Green's function[28] [51]

$$\tilde{G}_{n\underline{k}}(\tau,\tau') \equiv -i\left\langle \mathcal{T}_K \left\{ \mathrm{e}^{-i\int_K \mathrm{d}\tau_1\ \mathcal{H}_{\mathrm{eph}}(\tau_1)} c_{n\underline{k}}(\tau) c^\dagger_{n\underline{k}}(\tau') \right\} \right\rangle \tag{2.124}$$

where K is the so-called Schwinger-Keldysh contour given in figure 2.3. Please note that here and in the following, the explicit subscript $\mathcal{H}$ indicating that the time evolution is treated in the interaction picture was dropped.

The contour-ordered Green's function as defined in equation (2.124) proves to be a particularly good starting point for handling steady-state non-equilibrium phenomena in a perturbative approach: First of all, if $\tau < \tau'$ in the contour sense, then $\tilde{G}$ reduces to the so-called lesser Green's function $\tilde{G}^<$ whose diagonal elements are proportional to the density of the interacting system. Hence it contains all necessary information on the system, and therefore is a quantity worth to obtain [51].

Second, the treatment of the time evolution in the interaction picture in conjunction with the closed contour-ordering conveniently separates the Hamiltonian $\mathcal{H}_{\mathrm{eph}}$ describing the mutual coupling of both species in *one* single exponential operator. This feature allows for a systematic expansion in orders of the perturbation by means of the known series of the exponential function [51].

Third, this kind of expansion generates sums of averages over strings of field operators weighted with respect to the interaction-free statistical operator n. These products may be split up in additional sums of products of averages over tuples, which will turn out to correspond to the known Green's functions G and D of the isolated electrons and bare phonons [50, 51]. This procedure will be described in some detail in the next section and permits the definition of a self-energy determined by the free particles and their coupling vertex.

Finally, the use of the Schwinger-Keldysh contour will, after "analytical continuation," produce a real-time Dyson's equation whose integrals are taken over the whole real axis. This in combination with the fact that the system is considered to be in steady-state will make a Fourier transform to the energy domain used in the previous sections 2.1 and 2.2 possible.

Perturbation Expansion and Self-Energy

In zero-th order perturbation theory the contour-ordered Green's function (2.124) reduces to [51]

$$\tilde{G}^{(0)}_{n\underline{k}}(\tau,\tau') = -i\left\langle \mathcal{T}_K \left\{ c_{n\underline{k}}(\tau) c^\dagger_{n\underline{k}}(\tau') \right\} \right\rangle, \tag{2.125}$$

which clearly is *not* the retarded Kohn-Sham Green's function, i.e., definition (2.12) in the limit $\mathrm{Im}\, z \downarrow 0$. It may, however, be related to this quantity: Assume τ and τ'

[28] Please note that this is already an (extremely common) approximation. As seen from equation (2.118), the electron-phonon Hamiltonian introduces scattering between Kohn-Sham states, and hence it is *not* obvious why the full Green's function should be diagonal in $\{|n\underline{k}\rangle\}$. While this property may be seen for the wave vector $\underline{k}$ due to the periodicity of the lattice, interband matrix elements remain in fact possible. Hence, in the general case one is bound to study $\tilde{G}_{nn'\underline{k}}(\tau,\tau')$, leading to very similar self-energy expressions [75].

to reside on the backward branch of the Schwinger-Keldysh contour. Then

$$\tilde{G}^{(0)}_{n\underline{k}}(t,t') = -i \begin{cases} +\left\langle c_{n\underline{k}}(t) c^\dagger_{n\underline{k}}(t') \right\rangle & \text{if } t > t' \\ -\left\langle c^\dagger_{n\underline{k}}(t') c_{n\underline{k}}(t) \right\rangle & \text{if } t < t' \end{cases} \equiv \begin{cases} G^{>}_{n\underline{k}}(t,t') & \text{if } t > t' \\ G^{<}_{n\underline{k}}(t,t') & \text{if } t < t'. \end{cases} \tag{2.126}$$

If the contour times are on the forward path, the roles are skipped, meaning that we have access to both greater and lesser Green's function at all times. Employing further that the time evolution of the Kohn-Sham creation and annihilation operators is readily obtained from the Heisenberg equation of motion yields [72]

$$G^{>}_{n\underline{k}}(t,t') = -i\mathrm{e}^{-i\varepsilon_{n\underline{k}}(t-t')}(1 - f_{n\underline{k}}), \tag{2.127a}$$

$$G^{<}_{n\underline{k}}(t,t') = +i\mathrm{e}^{-i\varepsilon_{n\underline{k}}(t-t')} f_{n\underline{k}}, \tag{2.127b}$$

where $f_{n\underline{k}} = \left\langle c^\dagger_{n\underline{k}} c_{n\underline{k}} \right\rangle$ as well as the anti-commutation relation was used. Therefore, the Fourier transform of the difference for $t > t'$ [72]

$$\begin{aligned} &\lim_{\mathrm{Im}\, z \downarrow 0} \int_{\mathbb{R}} \mathrm{d}(t-t')\ \mathrm{e}^{iz(t-t')} \theta(t-t') \left[G^{>}_{n\underline{k}}(t-t') - G^{<}_{n\underline{k}}(t-t') \right] \\ &= \lim_{\mathrm{Im}\, z \downarrow 0} \frac{1}{z - \varepsilon_{n\underline{k}}} = \lim_{\mathrm{Im}\, z \downarrow 0} \langle n\underline{k} \,|\, \mathcal{G}(z) \,|\, n\underline{k} \rangle \end{aligned} \tag{2.128}$$

to energy domain turns out to be the diagonal matrix element (2.19) of the retarded Kohn-Sham Green's function in its eigenbasis. A powerful generalization of this procedure, the Langreth theorem, will be used in the next section to perform the analytical continuation of Dyson's equation. Nevertheless, we will exploit this result and simply write $G_{n\underline{k}}$ instead of $\tilde{G}^{(0)}_{n\underline{k}}$ in the following higher order expansions.

The expansion of the evolution operator to first order is given by

$$\begin{aligned} \tilde{G}^{(1)}_{n\underline{k}}(\tau,\tau') = -i \Bigg\langle \mathcal{T}_K \Bigg\{ \frac{(-i)^1}{1!} \int_K \mathrm{d}\tau_1 \frac{1}{\sqrt{N}} \sum_{\underline{q}_1 \nu_1} \sum_{n_1 m_1 \underline{k}_1} g^{\underline{q}_1 \nu_1}_{m_1 \underline{k}_1 + \underline{q}_1, n_1 \underline{k}_1} A_{\underline{q}_1 \nu_1}(\tau_1) \\ \times c^\dagger_{m_1 \underline{k}_1 + \underline{q}_1}(\tau_1) c_{n_1 \underline{k}_1}(\tau_1) c_{n\underline{k}}(\tau) c^\dagger_{n\underline{k}}(\tau') \Bigg\} \Bigg\rangle, \end{aligned} \tag{2.129}$$

which is zero because $\left\langle A_{\underline{q}\nu}(\tau) \right\rangle \equiv \left\langle b_{\underline{q}\nu}(\tau) + b^\dagger_{-\underline{q}\nu}(\tau) \right\rangle = 0$ [51]. Similarly, all odd orders of the perturbation expansion must vanish, and hence the second order of the perturbation expansion yields in fact the first order electron-phonon interaction: [51]

$$\begin{aligned} \tilde{G}^{(2)}_{n\underline{k}}(\tau,\tau') = -i \Bigg\langle \mathcal{T}_K \Bigg\{ \frac{(-i)^2}{2!} \int_K \mathrm{d}\tau_1 \int_K \mathrm{d}\tau_2 \frac{1}{N} \sum_{\substack{\underline{q}_1 \nu_1 \\ \underline{q}_2 \nu_2}} \sum_{\substack{n_1 m_1 \underline{k}_1 \\ n_2 m_2 \underline{k}_2}} g^{\underline{q}_1 \nu_1}_{m_1 \underline{k}_1 + \underline{q}_1, n_1 \underline{k}_1} \\ \times g^{\underline{q}_2 \nu_2}_{m_2 \underline{k}_2 + \underline{q}_2, n_2 \underline{k}_2} A_{\underline{q}_1 \nu_1}(\tau_1) A_{\underline{q}_2 \nu_2}(\tau_2) c^\dagger_{m_2 \underline{k}_2 + \underline{q}_2}(\tau_2) \\ \times c_{n_2 \underline{k}_2}(\tau_2) c^\dagger_{m_1 \underline{k}_1 + \underline{q}_1}(\tau_1) c_{n_1 \underline{k}_1}(\tau_1) c_{n\underline{k}}(\tau) c^\dagger_{n\underline{k}}(\tau') \Bigg\} \Bigg\rangle. \end{aligned} \tag{2.130}$$

$\Sigma^{\mathrm{F}}_{n\underline{k}}(\tau,\tau') \;\widehat{=}$  , $\qquad \Sigma^{\mathrm{H}}_{n\underline{k}}(\tau,\tau') \;\widehat{=}$ 

Figure 2.4.: Feynman diagram of the Fock-like and the Hartree-like self-energy contribution. The "wiggly" line corresponds to the bare phonon Green's function D, the solid line denotes the Kohn-Sham Green's function G of the electrons. The filled circles represent the electron-phonon vertices g.

The trace over the phonon states is non-zero only if $|\underline{q}_1\nu_1\rangle = |-\underline{q}_2\nu_2\rangle$. Further, because the averaging $\langle\bullet\rangle = \mathrm{Tr}\,[n\,\bullet\,]$ is with respect to the non-interacting system by construction, the Wick-Matsubara theorem states that the statistical average of this time-ordered product of Kohn-Sham field operators is equivalent to the sum of the averages of all possible pairs, where the sign has to reflect the necessary operator interchange count [50, 51, 72, 76]. Additionally, all disconnected[29] terms of this sum must vanish because of the contour time integration, which drastically reduces their number. All remaining terms must exist twice because of the possible interchange of the dummy integration variables, canceling the factor $\frac{1}{2!}$ originating from the expansion of the exponential [51]. In summary,

$$\begin{aligned}\tilde{G}^{(2)}_{n\underline{k}}(\tau,\tau') = &+\frac{i}{N}\sum_{m\underline{q}\nu} g^{-\underline{q}\nu}_{n\underline{k},m\underline{k}+\underline{q}} g^{\underline{q}\nu}_{m\underline{k}+\underline{q},n\underline{k}} \int_K \mathrm{d}\tau_1 \int_K \mathrm{d}\tau_2\; D_{-\underline{q}\nu}(\tau_1,\tau_2) \\ &\qquad \times G_{n\underline{k}}(\tau,\tau_1) G_{m\underline{k}+\underline{q}}(\tau_1,\tau_2) G_{n\underline{k}}(\tau_2,\tau') \\ &-\frac{i}{N}\sum_{m\underline{k}_2\nu} g^{\underline{0}\nu}_{n\underline{k},n\underline{k}} g^{\underline{0}\nu}_{m\underline{k}_2,m\underline{k}_2} \int_K \mathrm{d}\tau_1 \int_K \mathrm{d}\tau_2\; D_{\underline{0}\nu}(\tau_1,\tau_2) \\ &\qquad \times G_{n\underline{k}}(\tau,\tau_1) G_{n\underline{k}}(\tau_1,\tau') G_{m\underline{k}_2}(\tau_2,\tau_2),\end{aligned} \tag{2.131}$$

where $D_{\underline{q}\nu}(\tau,\tau') \equiv -i\left\langle \mathcal{T}_K\left\{A_{\underline{q}\nu}(\tau)A^\dagger_{\underline{q}\nu}(\tau')\right\}\right\rangle$ denotes the contour-ordered phonon Green's function [51, 72].

Although it is now possible to systematically expand the contour-ordered Green's function (2.124) to even higher orders, we will refrain from doing so and instead define the so-called Hartree- and Fock-like[30] self-energy contributions [72]

$$\Sigma^{\mathrm{F}}_{n\underline{k}}(\tau,\tau') \equiv \frac{i}{N}\sum_{m\underline{q}\nu}\left|g^{\underline{q}\nu}_{m\underline{k}+\underline{q},n\underline{k}}\right|^2 D_{\underline{q}\nu}(\tau,\tau') G_{m\underline{k}+\underline{q}}(\tau,\tau') \tag{2.132a}$$

$$\Sigma^{\mathrm{H}}_{n\underline{k}}(\tau,\tau') \equiv -\frac{i}{N}\delta(\tau-\tau')\sum_{\nu} g^{\underline{0}\nu}_{n\underline{k},n\underline{k}} \int_K \mathrm{d}\tau_1\; D_{\underline{0}\nu}(\tau,\tau_1)\,\mathrm{Tr}\left[\underline{\underline{G}}(\tau_1,\tau_1)\underline{\underline{g}}^{\underline{0}\nu}\right] \tag{2.132b}$$

[29] "Disconnected" refers to the corresponding Feynman diagram. In the simple case of the second-order expansion these are all those addends containing the Green's function $G_{n\underline{k}}(\tau,\tau')$.

[30] The connection between both electron-phonon vertices is established by exploiting that $\mathcal{H}_{\mathrm{eph}}$ is its own Hermitian adjoint. Further, the bare phonon Green's functions $D_{\underline{q}\nu}(\tau,\tau')$ and $D_{-\underline{q}\nu}(\tau,\tau')$ coincide if $\omega_{\underline{q}\nu} = \omega_{-\underline{q}\nu}$. This symmetry relation for the phonon frequencies follows for stable materials from the dynamical matrix [75].

depicted in figure 2.4. Then, with $\Sigma^{(2)}_{n\underline{k}} \equiv \Sigma^{\mathrm{F}}_{n\underline{k}} + \Sigma^{\mathrm{H}}_{n\underline{k}}$, the full Green's function may be approximated as

$$\begin{aligned}\tilde{G}_{n\underline{k}}(\tau,\tau') &\approx G_{n\underline{k}}(\tau,\tau') + \int_K \mathrm{d}\tau_1 \int_K \mathrm{d}\tau_2 \; G_{n\underline{k}}(\tau,\tau_1)\Sigma^{(2)}_{n\underline{k}}(\tau_1,\tau_2)G_{n\underline{k}}(\tau_2,\tau') \\ &\stackrel{!}{=} G_{n\underline{k}}(\tau,\tau') + \int_K \mathrm{d}\tau_1 \int_K \mathrm{d}\tau_2 \; G_{n\underline{k}}(\tau,\tau_1)\Sigma_{n\underline{k}}(\tau_1,\tau_2)\tilde{G}_{n\underline{k}}(\tau_2,\tau').\end{aligned} \tag{2.133}$$

From topological arguments it can be seen that if one defines the self-energy as the sum of all "one-particle irreducible" terms, then Dyson's equation in contour-time is valid [51]. Hence, comparison yields that $\Sigma^{\mathrm{F}}_{n\underline{k}}$ and $\Sigma^{\mathrm{H}}_{n\underline{k}}$ are a subset of all self-energy contributions, and experience proves them to be the most important ones, too. The neglect of all other contributions to the self-energy is commonly known as "First Born Approximation" and is, especially in the context of metals, also known as Migdal approximation [43, 72].

If the system under consideration further exhibits translational invariance it can be shown that the Hartree-like self-energy contribution vanishes [72]. While this is certainly true in the presented calculations on the pure metals copper and aluminum in sections 3.1 and 3.2, respectively, the premise will not be fulfilled in the case of Fe/MgO double barrier structures. Given, however, that the evaluation of the self-energy relies on third party codes not yet capable of calculating the Hartree-like part, within this work the approximation

$$\Sigma_{n\underline{k}}(\tau,\tau') \equiv \Sigma^{\mathrm{F}}_{n\underline{k}}(\tau,\tau') \tag{2.134}$$

to the electron-phonon self-energy is used. The ramifications in the case of Fe/MgO double barriers will be discussed to some extend in section 3.3.

Analytical Continuation and Transformation to Energy Domain

Now that the self-energy approximation has been obtained by means of the perturbative approach, the contour-time formalism has outlived its utility. Instead, the transmission formulae derived in section 2.2.3 rely on energy-dependent quantities. The necessary transformation process consists of two steps: First, the "analytical continuation" to conventional time arguments will be discussed. Subsequently, a Fourier transformation will yield the transition to energy domain.

Iteratively using the Langreth's theorem for the retarded operator [50, 72]

$$C^{\mathrm{R}}(t,t') = \left[\int_K \mathrm{d}\tau_1 \; A(t,\tau_1)B(\tau_1,t')\right]^{\mathrm{R}} = \int_{\mathbb{R}} \mathrm{d}t_1 \; A^{\mathrm{R}}(t,t_1)B^{\mathrm{R}}(t_1,t') \tag{2.135}$$

on equation (2.133) yields the real-time Dyson's equation

$$\tilde{G}^{\mathrm{R}}_{n\underline{k}}(t,t') = G^{\mathrm{R}}_{n\underline{k}}(t,t') + \int_{\mathbb{R}} \mathrm{d}t_1 \int_{\mathbb{R}} \mathrm{d}t_2 \; G^{\mathrm{R}}_{n\underline{k}}(t,t_1)\Sigma^{\mathrm{R}}_{n\underline{k}}(t_1,t_2)\tilde{G}^{\mathrm{R}}_{n\underline{k}}(t_2,t'). \tag{2.136}$$

The self-energy contains a product of phonon and electron Green's function being of the kind $A(\tau,\tau')B(\tau,\tau')$. This is not covered by theorem (2.135), but may be evaluated as [50, 72]

$$C^{\mathrm{R}}(t,t') = \left[A^{<}B^{\mathrm{R}} + A^{\mathrm{R}}B^{<} + A^{\mathrm{R}}B^{\mathrm{R}}\right](t,t') = \left[A^{\mathrm{R}}B^{<} + A^{>}B^{\mathrm{R}}\right](t,t'), \quad (2.137)$$

where the second equality is derived using the representation of the retarded Green's function in terms of the greater and lesser ones introduced in equation (2.128). Finally, because both electronic and phononic Green's function depend as correlation functions describing isolated systems not on t and t' but only on their difference, a Fourier transformation from time to energy domain allows to obtain Dyson's equation (2.16) with the electron-phonon self-energy as potential difference

$$\begin{aligned}\Sigma^{\mathrm{R}}_{n\underline{k}}(E) =& \frac{i}{N}\sum_{m\underline{q}\nu}\left|g^{\underline{q}\nu}_{m\underline{k}+\underline{q},n\underline{k}}\right|^2 \int_{\mathbb{R}}\frac{\mathrm{d}E'}{2\pi} \\ &\times\left(D^{\mathrm{R}}_{\underline{q}\nu}(E-E')G^{<}_{m\underline{k}+\underline{q}}(E') + D^{>}_{\underline{q}\nu}(E-E')G^{\mathrm{R}}_{m\underline{k}+\underline{q}}(E')\right).\end{aligned} \quad (2.138)$$

While this expression is convenient[31] for the evaluation using a Green's function formalism code, it may be reduced to a representation more suitable for a (pseudopotential) plane-wave code by substituting the known analytical expressions for both types of Green's functions. The integral may then be evaluated as [17, 49]

$$\begin{aligned}\Sigma^{\mathrm{R}}_{n\underline{k}}(E,T) =& \sum_{m\nu}\int_{\mathrm{BZ}}\frac{\mathrm{d}^3q}{(2\pi)^3}\ \left|g^{\underline{q}\nu}_{m\underline{k}+\underline{q},n\underline{k}}\right|^2 \\ &\times\left(\frac{n_{\underline{q}\nu}(T)+1-f_{m\underline{k}+\underline{q}}(T)}{E-\varepsilon_{m\underline{k}+\underline{q}}-\omega_{\underline{q}\nu}+i\eta} + \frac{n_{\underline{q}\nu}(T)+f_{m\underline{k}+\underline{q}}(T)}{E-\varepsilon_{m\underline{k}+\underline{q}}+\omega_{\underline{q}\nu}+i\eta}\right),\end{aligned} \quad (2.139)$$

where the sum over all possible phonon wave vectors was transformed into a Brillouin zone integration and, additionally, the temperature dependence governed by the statistical operator (2.119) has been reintroduced. In this equation [47]

$$n_{\underline{q}\nu}(T) \equiv \left\langle b^{\dagger}_{\underline{q}\nu}b_{\underline{q}\nu}\right\rangle = \left(\exp\left[\frac{\omega_{\underline{q}\nu}}{k_BT}\right]-1\right)^{-1} \quad (2.140)$$

denotes the Bose-Einstein distribution.

As was already discussed in the context of equation (2.70), in the limit of vanishing external bias voltage it is often sufficient to restrict the transmission calculations to the Fermi energy only. In this case it is sufficient to calculate the imaginary part of the self-energy, the negative of the so-called electron linewidth,[32] because in

[31] It is, actually, not convenient at all, because not only the Green's function at the energy of interest E enters, but also all those at the energies E' lying within the range $E \pm \hbar\omega_{\max}$, where $\omega_{\max}$ is a carefully chosen frequency cut-off determined by the phonon dispersion. This makes an evaluation of the self-energy computationally very demanding.

[32] Please note that this term is not used consistently throughout literature: While many authors call $-\operatorname{Im}\Sigma_{\mathrm{eph}}$ the electron linewidth, others prefer $-2\operatorname{Im}\Sigma_{\mathrm{eph}}$, or simply $\operatorname{Im}\Sigma_{\mathrm{eph}}$. Of course, a "width" should not be negative, and the sign is hence implied. Therefore, we will several times refer to equation (2.141) as "electron linewidth equation," intending to calculate $|\operatorname{Im}\Sigma_{\mathrm{eph}}|$.

accordance with Luttinger's theorem stating that the volume enclosed by the Fermi surface is not influenced by any[33] electron-electron interaction, the real part of the self-energy is known to be exactly zero at the Fermi energy [68, 75, 77]. Taking the limit $\eta \downarrow 0$ and employing once again the Dirac identity (2.26) yields [17, 43]

$$\begin{aligned}\operatorname{Im}\Sigma_{\mathrm{eph}}(n\underline{k}, E, T) = &-\pi \sum_{m\nu} \int_{\mathrm{BZ}} \frac{\mathrm{d}^3 q}{(2\pi)^3} \left| g^{\underline{q}\nu}_{m\underline{k}+\underline{q}, n\underline{k}} \right|^2 \\ &\times \Big[\big(n_{\underline{q}\nu}(T) + 1 - f_{m\underline{k}+\underline{q}}(T)\big) \delta\big(E - \varepsilon_{m\underline{k}+\underline{q}} - \omega_{\underline{q}\nu}\big) \\ &+ \big(n_{\underline{q}\nu}(T) + f_{m\underline{k}+\underline{q}}(T)\big) \delta\big(E - \varepsilon_{m\underline{k}+\underline{q}} + \omega_{\underline{q}\nu}\big) \Big] .\end{aligned} \tag{2.141}$$

This is the self-energy formula employed throughout this work. Details on how this expression is evaluated will be given in the next section.

2.3.3. Evaluation from First Principles

To evaluate equation (2.141), both the electronic and vibrational system must be solved. Because of the $\underline{q}$ integration over the whole Brillouin zone both calculations are coupled in the sense that for each wave vector $\underline{q}$ the electronic eigenstates and eigenenergies at $\underline{k} + \underline{q}$ must be known. It is hence convenient to choose both meshes "commensurate" [43], i.e., to ensure that for any two points $\underline{k}$ and $\underline{q}$ of the symmetry expanded mesh one finds another mesh point $\underline{k}'$ and possibly a reciprocal lattice vector $\underline{G}$ such that $\underline{k} + \underline{q} + \underline{G} = \underline{k}'$.

The necessary eigenenergies $\varepsilon_{m\underline{k}+\underline{q}}$ and, for the electron-phonon vertices (2.116), the eigenstates $|m\underline{k} + \underline{q}\rangle$ are obtained by solving the eigenvalue problem of the Kohn-Sham Hamiltonian (2.8) at the equilibrium positions $\{\underline{R}^0\}$. The electronic distribution functions $f_{m\underline{k}+\underline{q}}(T)$ are then given by equation (2.30). Within this work, this task is performed using the `pw.x` code of the QUANTUM ESPRESSO suite [24].

Besides the electronic system, the phonon eigenfrequencies $\omega_{\underline{q}\nu}$ and, yet again for the electron-phonon vertices (2.116), the polarization vectors $\underline{e}^{\nu}_{\kappa}(\underline{q})$ must be calculated. Similar to the previous case this is, within this work, done by employing the QUANTUM ESPRESSO suite, particularly the `ph.x` code [24]: For each wave vector $\underline{q}$ of the symmetry-reduced equidistant grid the dynamical matrix (2.108) is calculated in the framework of density-functional perturbation theory (DFPT) by evaluating the variations in both the self-consistent effective potential (2.117) and the electron density induced by several irreducible atomic displacement patterns $\{\underline{R}^0 + \underline{u}(\underline{q})\}$ [20, 49, 75]. The dynamical matrix is then diagonalized to solve the phonon eigenvalue problem (2.107), yielding the sought-after eigenfrequencies and polarization vectors. The phonon distribution functions are then given by (2.140).

Based thereupon, the electron-phonon vertices (2.116) and, subsequently, the imaginary part of the self-energy (2.141) could in principle be calculated. Nevertheless, this direct solution procedure is unfavorable for the following reasons.

[33] The scattering of Kohn-Sham quasiparticles by phonons mediates of course an effective electron-electron interaction.

First, as seen from the delta distributions in equation (2.141), the integrand proves to be extremely structured, and thus requires a very dense sampling of the Brillouin zone for the phonon wave vectors to ensure an accurate quadrature [43]. Given, however, that in the framework of DFPT several self-consistent DFT calculations are necessary to obtain the dynamical matrix at one $\underline{q}$ point, such meshes tend to be forbiddingly demanding from a computational point of view.[34]

Second, the electronic states contributing to the charge carrier transport are usually not distributed homogeneously in the whole Brillouin zone, but are confined to the vicinity of the Fermi energy [34]. Therefore, a dense and equidistant $\underline{k}$ sampling as proposed for reasons of commensurability with the phonon mesh is physically not very sound.

The solution to both issues as proposed by Giustino, Cohen, and Louie [43] is to calculate all necessary quantities on a coarse equidistant grid by first-principles methods, and then employ a generalized Fourier interpolation to very dense meshes for the evaluation of the self-energy formula (2.141). In order to have fast transformations the intermediate basis set should be chosen in such a manner that the accuracy of the inverse Fourier transform depends on a very limited number of elements, only. A promising candidate are the so-called maximally localized Wannier functions (MLWFs) [43, 45, 46]

$$|m\underline{R}_e^0\rangle = \sum_{n\underline{k}} \mathrm{e}^{-i\underline{k}\cdot\underline{R}_e^0} U_{nm}(\underline{k})\,|n\underline{k}\rangle\,, \quad |n\underline{k}\rangle = \frac{1}{N_e}\sum_{me} \mathrm{e}^{i\underline{k}\cdot\underline{R}_e^0} U^\dagger_{mn}(\underline{k})\,|m\underline{R}_e^0\rangle\,, \tag{2.142}$$

where N_e denotes the number of cells in the periodic boundary conditions imposed on the electronic calculations. In this scheme the arbitrary unitary matrices $\underline{\underline{U}}(\underline{k})$ are obtained by iteratively minimizing the spread functional [46]

$$\Omega = \sum_m \left(\left\langle m\underline{R}_0^0 \,\middle|\, \hat{r}^2 \,\middle|\, m\underline{R}_0^0 \right\rangle - \left\langle m\underline{R}_0^0 \,\middle|\, \hat{\underline{r}} \,\middle|\, m\underline{R}_0^0 \right\rangle^2 \right), \tag{2.143}$$

which ensures a small overlap of all those Wannier functions that are centered on different sites $\underline{R}_e^0$. Substituting relation (2.142) into definition (2.116) yields [43]

$$\begin{aligned} \underline{\underline{g}}^\nu(\underline{k},\underline{q}) &\equiv \left\{ g^{q\nu}_{m\underline{k}+\underline{q},n\underline{k}} \right\}_{mn} \\ &= \frac{1}{N_e}\sum_{le} \mathrm{e}^{i\left(\underline{k}\cdot\underline{R}_e^0 + \underline{q}\cdot\underline{R}_l^0\right)} \underline{\underline{U}}(\underline{k}+\underline{q}) \left(\sum_\kappa \underline{\underline{g}}_\kappa(\underline{R}_e^0, \underline{R}_l^0)\cdot \underline{u}_\kappa^\nu(\underline{q}) \right) \underline{\underline{U}}^\dagger(\underline{k}), \end{aligned} \tag{2.144}$$

where analogous to (2.116) and (2.114) the electron-phonon vertex in Wannier representation and the phonon displacement have been defined as

$$\underline{\underline{g}}_\kappa(\underline{R}_e^0, \underline{R}_l^0) \equiv \left\{ \left\langle m\underline{R}_0^0 \,\middle|\, -\nabla^{\mathrm{T}} V^\kappa_{\mathrm{eff}}(\underline{r} - \underline{R}_{l\kappa}^0) \,\middle|\, n\underline{R}_e^0 \right\rangle \right\}_{mn}, \tag{2.145a}$$

$$\underline{u}_\kappa^\nu(\underline{q}) \equiv \sqrt{\frac{\hbar}{2M_\kappa \omega_{\underline{q}\nu}}}\, \underline{e}_\kappa^\nu(\underline{q}) \mathrm{e}^{i\underline{q}\cdot\underline{\tau}_\kappa^0}. \tag{2.145b}$$

[34] This issue may cease with the advance of accessible high-performance computing facilities, as the monochromatic nature of DFPT allows for a trivial parallelization over phonon perturbations [20].

It can be shown that the first order change in the potentials $-\nabla^{\mathrm{T}} V_{\mathrm{eff}}^{\kappa}(\underline{r}-\underline{R}_{l\kappa}^{0})$ exhibits a spatial decay similar to the interatomic force constants, which are typically short-ranged at least in metals due to the efficient screening [43]. Hence, by construction of the electronic Wannier functions, the matrix element in (2.145a) will vanish whenever the distance between any of the positions $\underline{R}_{e}^{0}$, $\underline{R}_{0}^{0}$ and $\underline{R}_{l}^{0}$ is big, and therefore relatively few addends will enter the generalized inverse Fourier transform (2.144) as desired [43]. The evaluation of the electron linewidth by means of equation (2.141) with a very dense $\underline{q}$ sampling is now possible [43]:

1. As described above, calculate the electronic eigenstates $|n\underline{k}\rangle$ and eigenenergies $\varepsilon_{n\underline{k}}$ as well as the phonon polarizations $\underline{e}_{\kappa}^{\nu}(\underline{q})$, eigenfrequencies $\omega_{\underline{q}\nu}$ and first order variations of the effective potential $\delta_{\kappa}^{\underline{q}\nu} V_{\mathrm{eff}}^{\kappa}$ on coarse, equidistant and commensurate $\underline{k}$ and $\underline{q}$ meshes using QUANTUM ESPRESSO.

On the basis of these prerequisites, EPW performs the following tasks [43]:

2. Obtain maximally localized Wannier functions (2.142) of the electronic system using `wannier90`, thereby getting hold of the unitary matrices $\underline{\underline{U}}(\underline{k})$ on the coarse grid.
3. Evaluate the electron-phonon vertex (2.116) in Bloch representation on the coarse $(\underline{k},\underline{q})$ mesh.
4. Invert the generalized Fourier transform (2.144) to calculate the electron-phonon vertex (2.145a) in Wannier representation.
5. Transform the Kohn-Sham Hamiltonian $\underline{\underline{H}}_{\mathrm{KS}}^{\{\underline{R}^{0}\}}(\underline{k}) = \left\{\delta_{mn}\varepsilon_{n\underline{k}}\right\}_{mn}$ from Bloch to Wannier representation using the relations (2.142) [43]
$$\underline{\underline{H}}_{\mathrm{KS}}^{\{\underline{R}^{0}\}}(\underline{R}_{0}^{0},\underline{R}_{e}^{0}) = \sum_{\underline{k}} \mathrm{e}^{-i\underline{k}\cdot\underline{R}_{e}^{0}} \underline{\underline{U}}^{\dagger}(\underline{k}) \underline{\underline{H}}_{\mathrm{KS}}^{\{\underline{R}^{0}\}}(\underline{k}) \underline{\underline{U}}(\underline{k}). \tag{2.146}$$
6. Similarly, transform the dynamical matrix to Wannier representation.
7. Iterate over every wave vector $\underline{k}'$ at which the value of the electron linewidth shall be evaluated and every $\underline{q}'$ in the Brillouin zone.
   a) Diagonalize the Fourier-interpolated Kohn-Sham Hamiltonian [43]
   $$\underline{\underline{H}}_{\mathrm{KS}}^{\{\underline{R}^{0}\}}(\underline{k}') = \underline{\underline{U}}(\underline{k}') \left(\frac{1}{N_e} \sum_{e} \mathrm{e}^{i\underline{k}'\cdot\underline{R}_{e}^{0}} \underline{\underline{H}}_{\mathrm{KS}}^{\{\underline{R}^{0}\}}(\underline{R}_{0}^{0},\underline{R}_{e}^{0}) \right) \underline{\underline{U}}^{\dagger}(\underline{k}') \tag{2.147}$$
   to obtain $\underline{\underline{U}}^{\dagger}(\underline{k}')$ and $\underline{\underline{U}}(\underline{k}'+\underline{q}')$ as well as the eigenenergies $\varepsilon_{m\underline{k}'+\underline{q}'}$ and distribution functions $f_{m\underline{k}'+\underline{q}'}(T)$.
   b) Similarly, diagonalize the Fourier-interpolated dynamical matrix to get hold of $\underline{e}_{\kappa}^{\nu}(\underline{q}')$ as well as the eigenfrequencies $\omega_{\underline{q}'\nu}$ and the distribution functions $n_{\underline{q}'\nu}(T)$.
   c) Use equation (2.144) to interpolate the electron-phonon vertex $\underline{\underline{g}}^{\nu}(\underline{k}',\underline{q}')$ in Bloch representation.
8. Calculate the electron linewidth as the negative of equation (2.141).

2.3.4. Wave-vector Averaging

Another issue to solve is based on the fact that the implementation as described in section 2.2.3 on the calculation of the full Green's function in the KKR representation heavily relies on solving Dyson's equation by means of multiple-scattering theory. In particular, one must be able to calculate the scattering solutions of the muffin-tin potential given by equation (2.87) to make use of the ansatz (2.89). As seen from the derivation of the transmission formulae (2.97) and (2.100), any dependence of the transmission on the wave vector $\underline{k}$ is due to the lattice Fourier transform (2.96) and hence a remnant of the in-plane periodicity of the system. The scattering solutions (2.48) entering in the KKR representation of the Green's function are, however, those of the *isolated* muffin-tin potential by construction, and therefore those of a non-periodic system. Thus, a straightforward generalization using $\underline{k}$-dependent scattering solutions seems not possible. Even if this conceptual problem may be circumvented, the wave vector $\underline{k}$ entering in equation (2.141) is an element of the three-dimensional Brillouin zone, while the corresponding quantity in the transmission formulae is an element of the surface Brillouin zone arising from the in-plane periodicity. In summary, a suitable way to average over all those wave vectors contributing to the charge carrier transport is necessary in any case.

The solution proposed in this work makes use of the observation that, at least in the case of vanishing external bias voltage, the electronic states contributing to the charge carrier transport are those within the equi-energy surface[35] $S(E,T)$ of energy E and temperature T. More precisely we may restrict ourselves to the subset $S^+(E,T) \subset S(E,T)$ of the states having a positive wave vector component k_z [34]. Thus, the toolkit *fermint* has been developed, which is able to obtain both those states as well as their corresponding integration weights. The procedure of wave-vector-averaging the electronic self-energy is as follows.

In a first step, the eigenenergies of the electronic system are evaluated on an equidistant grid in reciprocal space using any first-principles calculation or interpolation method.[36] For each individual electronic band these mesh points are then interpreted as the corners of cubes as depicted in figure 2.5, where + and − indicate that the eigenenergy $\varepsilon_{n\underline{k}}$ at this $\underline{k}$-point is bigger or smaller than the reference energy E, respectively. Based on these energy values, the crossings A to G of the equi-energy surface with the cube edges are then approximated by means of a linear interpolation.[37] Depending on the arrangement of crossings and edges, the connecting surfaces – here the triangle ABC and the quadrangle $DEFG$ – may be deduced from topological arguments. In order to obtain the integrations weights, all polygons having more than three vertices are further split into suitable triangles. As of now,

[35] In case of $E = E_F$ this is the so-called Fermi surface.

[36] As of now, only the results of QUANTUM ESPRESSO and `wannier90` calculations can be used, but the code may readily be expanded to e.g. KKR calculations by implementing a suitable subclass of `AbstractDispersionReader`.

[37] As will be discussed in section 3.1.4, the accuracy of this interpolation step may be crucial for the validity of the averaged result. Therefore, a higher-order interpolation scheme specifically suited for electronic structure calculations may reduce the necessary mesh sizes to a great extend.

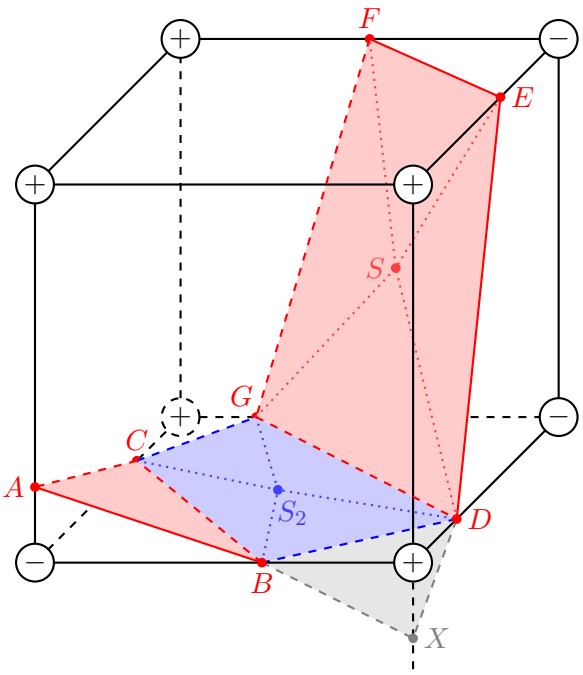

Figure 2.5.: Schematic representation of the triangulation process as implemented in *fermint*. While the polygons ABC and $DEFG$ are found by a topological intra-cell analysis, the polygon $BDGC$ is only seen to be part of the equi-energy surface through multi-cell analysis. The vertices S and S_2 are approximated as the centroids of the quadrangles.

this task is performed by simply calculating the centroid[38] S of the polygon as well as the areas of all triangles P_iSP_j, where $P_{i/j}$ are neighboring vertices of the polygon under study, and then distributing these areas to the adjacent points. In the example at hand, the area corresponding to the vertex E is thus given by $\frac{1}{2}ESD + \frac{1}{2}FSE$, plus all the contributions from the other cubes containing E.

If six or more crossings of the equi-energy surface with the cube edges are present, it may be insufficient to exclusively analyze each cube on its own: In figure 2.5 it is at first uncertain whether the polygon $BDGC$ should be considered part of the equi-energy surface or not. In this case a multi-cell analysis is performed,[39] checking whether the line segments $\overline{BD}$ and $\overline{CD}$ are contained in any of the polygons of the neighboring cube. This kind of analysis provides the information that $\overline{BD}$ is an

[38] Instead of calculating the geometric mean, it would be reasonable to use the crossings of the equi-energy surface with the cube diagonals, as this would allow for a description of the curvature of the surface. However, as the diagonals have the length $\sqrt{3}a$, with a being the edge length, the linear interpolation scheme would perform rather bad. Hence, this issue should be addressed *after* the higher-order interpolation scheme mentioned in footnote 37 has been implemented.

[39] As of now, the multi-cell analysis was only implemented for the case of 6 crossings, which proved to be sufficient for the Fermi surfaces presented in this work.

edge of the triangle BXD of the neighboring cell, and hence $BDGC$ is part of the equi-energy surface.

Once the triangulation of the equi-energy surface has been obtained, the imaginary part of the electron-phonon self-energy (2.141) is calculated at all[40] wave vectors $\underline{k} \in S^+(E,T)$. The wave-vector-averaged self-energy is subsequently given by [124]

$$\operatorname{Im}\Sigma_{\mathrm{eph}}(E,T) = \sum_{n\underline{k}\in S^+(E,T)} \frac{A_{n\underline{k}}(E,T)}{A_{S^+}(E,T)} \cdot \operatorname{Im}\Sigma_{\mathrm{eph}}(n\underline{k},E,T), \tag{2.148}$$

where $A_{n\underline{k}}$ denotes the area corresponding to each vertex, and A_{S^+} is the area of the part of the equi-energy surface having a positive k_z component. If, on the other hand, the wave vector dependence shall be preserved, a projection of S^+ to the surface Brillouin zone may be performed.[41]

2.4. Thermal Expansion

With increasing temperature the atomic displacements $\{\underline{u}\}$ may become sufficiently large for the harmonic approximation (2.103) to fail. The higher-order contributions to the effective potential (2.102) will then induce a shift of the center of the atomic oscillations in such a manner that the average distance between the moving nuclei increases, i.e., the solid will display thermal expansion [78]. Given that the systematic inclusion of anharmonic lattice vibrations in first-principles calculations is rather elaborate, we will settle in this work for what is commonly called "quasi-harmonic approximation" [79]: It will be assumed that anharmonicity is *restricted* to thermal expansion and that the oscillations hence remain harmonic. The frequencies are, however, assumed to be volume-dependent, which may conveniently be encapsulated in the so-called Grüneisen parameter γ as described below. To employ this approximation one must find a means to calculate the lattice constant $a(T)$ at any given temperature T. The phonon eigenfrequencies and polarization vectors may then be obtained in the usual manner by diagonalizing the dynamical matrix (2.108).

2.4.1. Equation of State

In order to theoretically describe the thermal expansion of a solid, a suitable equation of state must first be derived from thermodynamics. As described above, this thermal expansion is attributed to the volume dependence of the eigenstates of the lattice vibrations. Hence, assuming no further inner degrees of freedom, the internal energy U of a solid consists of the two contributions [80, 81]

$$U(V,T) = U_{\mathrm{vib}}(T) + U_{\mathrm{el}}(V), \tag{2.149}$$

i.e., the temperature-dependent vibrational energy U_{vib} as well as the volume-dependent elastic energy U_{el}. According to the first law of thermodynamics the

[40] It is, in fact, possible to reduce the necessary computational burden by exploiting symmetries.
[41] Please note that this is not (yet) implemented in *fermint*.

change in internal energy $\mathrm{d}U$ is given by the sum of heat δQ consumed by the system and the work δW done by the surroundings on this very system [81]

$$\mathrm{d}U = \delta Q + \delta W = \delta Q + \sum_i F_i \mathrm{d}q_i, \tag{2.150}$$

where, as known from any course on analytical mechanics, the work may be conveniently written in terms of the generalized coordinates q_i and generalized forces F_i. In the analysis of thermal expansion it is reasonable to assume the absence of any external circumstances hindering the enlargement of the system, and therefore the solid will only have to perform work against the external pressure, leading to the sole generalized coordinates $F = -p$ and $\mathrm{d}q = \mathrm{d}V$ [81]. Further, this process is deemed to be reversible, and hence employing the second law of thermodynamics yields [80, 81]

$$\mathrm{d}S = \frac{\mathrm{d}U + p\mathrm{d}V}{T}. \tag{2.151}$$

Of course, lattice vibrations in solids may be described by quantum-mechanical oscillators whose eigenenergies are quantized in units of $\hbar\omega$. Even though the oscillator frequency will *not* be uniform for any vibrational state, this ω is assumed to be a suitably chosen mean value. Further, in accordance with the considerations given in the introduction of this section on thermal expansion, it will depend on the volume. With this in mind one may define the dimensionless quantity [80]

$$X(V,T) \equiv \frac{U(V,T)}{\hbar\omega(V)}. \tag{2.152}$$

Then, from equation (2.151) it is seen that [80]

$$\frac{1}{T} = \left(\frac{\partial S}{\partial U}\right) = \frac{\mathrm{d}S}{\mathrm{d}X}\frac{\partial X}{\partial U} = \frac{\mathrm{d}S}{\mathrm{d}X}\frac{1}{\hbar\omega(V)} \tag{2.153a}$$

$$\frac{p}{T} = \left(\frac{\partial S}{\partial V}\right) = \frac{\mathrm{d}S}{\mathrm{d}X}\frac{\partial X}{\partial V} = \frac{\mathrm{d}S}{\mathrm{d}X}\frac{1}{\hbar\omega(V)}\left(U'_{\mathrm{el}}(V) - U(V,T)\frac{1}{\omega(V)}\frac{\partial\omega}{\partial V}\right) \tag{2.153b}$$

and therefore – by eliminating $\frac{\mathrm{d}S}{\mathrm{d}X}$ – the sought-after equation of state [12, 80]

$$pV + G(V) = \gamma(V)U(V,T) \tag{2.154}$$

is proven. To arrive at this expression, the function G and the Grüneisen parameter γ have been defined as [79]

$$G(V) \equiv -VU'_{\mathrm{el}}(V), \quad \text{and} \quad \gamma(V) \equiv -\frac{V}{\omega(V)}\frac{\partial\omega}{\partial V}. \tag{2.155}$$

To paraphrase this result, the Grüneisen parameter explicitly describes the volume dependence of the eigenfrequencies of the lattice vibrations.

2.4.2. True Coefficient of Thermal Expansion

Let $V(T)$ denote the volume the solid actually takes at temperature T in case the external pressure is negligible. Under this and all previous assumptions, the equation of state (2.154) reads [12]

$$G(V(T)) = \gamma U(T), \tag{2.156}$$

where the additional approximation $\gamma(T) = \gamma(V(T)) \approx \text{const.}$ is justified by experience [12, 79]. The system is considered stable, and hence there exists a volume V_0 characterized by

$$U'_{\text{el}}(V_0) = 0, \tag{2.157}$$

or more precisely, the elastic energy U_{el} has a minimum determined by the equilibrium positions $\{\underline{R}^0\}$ of the nuclei. Thus it is seen from the definition (2.155) that $G(V_0) = 0$, and expanding the function to second order therefore yields [12]

$$G(V(T)) \approx (V(T) - V_0)\left(G'(V_0) + \frac{G''(V_0)}{2!}(V(T) - V_0)\right). \tag{2.158}$$

Inserting this result in the specialized equation of state (2.156) allows to write [12]

$$V(T) - V_0 = \frac{\gamma U(T)}{G'(V_0) + \frac{G''(V_0)}{2}(V(T) - V_0)} \approx \frac{U(T)}{\frac{G'(V_0)}{\gamma} + \frac{G''(V_0)}{2G'(V_0)}U(T)}, \tag{2.159}$$

the last approximation being motivated by the knowledge that the change in the volume due to thermal effects is some percent in magnitude and hence quite small. With the definitions [12]

$$Q_0 \equiv \frac{V_0 G'(V_0)}{\gamma}, \quad \text{and} \quad g \equiv -\frac{V_0 G''(V_0)}{2G'(V_0)} \tag{2.160}$$

one finally arrives at [12]

$$\frac{V(T) - V_0}{V_0} = \frac{U(T)}{Q_0 - gU(T)}, \tag{2.161}$$

i.e., an equation directly relating the relative change in the volume to the internal energy and some material-dependent constants. Using the definition of the true[42] coefficient of thermal expansion [78, 79, 81]

$$\beta(T) \equiv \frac{1}{V(T)}\left(\frac{\partial V(T)}{\partial T}\right)_p \tag{2.162}$$

and its relation $\beta(T) = 3\alpha(T)$ to the true linear coefficient of thermal expansion, we may obtain [83]

$$\alpha(T) = \frac{C_V(T)}{3Q_0\left[1 - g\frac{U(T)}{Q_0}\right]^2}, \quad U(T) = \int_0^T \mathrm{d}t\; C_V(t), \tag{2.163}$$

[42] Especially experimental data tends to be normalized by $1/V(T_0)$ instead of $1/V(T)$ [82]. For the sake of clarity, we will explicitly state which kind of coefficient of thermal expansion is meant.

by differentiating equation (2.161) with respect to the temperature, where the heat capacity at constant volume is given by [81]

$$C_V(T) \equiv \left(\frac{\delta Q}{\mathrm{d}T}\right)_V = \left(\frac{\mathrm{d}U}{\mathrm{d}T}\right)_V = \frac{\mathrm{d}U_{\mathrm{vib}}(T)}{\mathrm{d}T}. \tag{2.164}$$

Please note that according to the definition of both coefficients of thermal expansion, the differentiation of the internal energy U would actually have to be performed ensuring the constraint of constant pressure – in fact, $p = 0$ as above – rather than constant volume. However, a theoretical quantification of $C_p(T)$ is much more elaborate than an appropriate relation for $C_V(T)$ as described in the next section. Rationalizing once again that the change in volume will be small we settle for the approximation $C_p(T) \approx C_V(T)$.

2.4.3. Evaluation in the Debye Model

Once the true linear coefficient of thermal expansion (2.163) as been obtained, it is possible to calculate the lattice constant $a(T)$ at arbitrary temperatures T as

$$a(T) = a_0 \exp\left(\int_{T_0}^{T} \mathrm{d}t\ \alpha(t)\right), \tag{2.165}$$

where the reference lattice constant $a_0 \equiv a(T_0)$ at any temperature T_0 serves as initial value to the corresponding differential equation. It is, however, quite nontrivial to evaluate this quantity: While the vibrational energy U_{vib} and therefore C_V may in principle be extracted as the average value of the phonon Hamiltonian [47]

$$U_{\mathrm{vib}}(T) = \langle \mathcal{H}_{\mathrm{ph}} \rangle = \sum_{\underline{q}\nu} \omega_{\underline{q}\nu} \left(n_{\underline{q}\nu}(T) + \frac{1}{2} \right), \tag{2.166}$$

where $n_{\underline{q}\nu}(T)$ is the Bose-Einstein distribution (2.140), the necessary values of g and Q_0 as defined by (2.160) require the knowledge of the elastic contribution U_{el} to the internal energy, the latter further the knowledge of the volume dependence of the phonon dispersion in terms of the Grüneisen parameter γ. The path to circumvent this issue pursued by Grüneisen was to study model potentials of the kind [12]

$$U_{\mathrm{el}}^{G}(V) = -\frac{A}{V^n} + \frac{B}{V^m}, \tag{2.167}$$

which allows to derive analytic expressions for the beforementioned quantities. Nevertheless, as he admits himself [12], the thermal expansion of solids is only correctly described if the value of g is chosen empirically. Hence, within this work, the values of g and Q_0 are determined by fitting the relation (2.163) to experimental data for the true linear coefficient of thermal expansion as proposed by Nix and MacNair [83]. Further, to reduce the computational burden of this optimization process, the vibrational energy was not obtained from the Brillouin zone integration (2.166), but

in the Debye model: Assuming the phonon dispersion is linear in the whole Brillouin zone, the heat capacity at constant volume is analytically given by [47, 83, 84]

$$C_v^D(T,\theta_D) = 9\frac{N}{V}k_B\left(\frac{T}{\theta_D}\right)^3\int_0^{\theta_D/T}\mathrm{d}x\,\frac{x^4\mathrm{e}^x}{(\mathrm{e}^x-1)^2}. \tag{2.168}$$

The unknown Debye temperature θ_D is yet again treated as a parameter in the fitting procedure.

3. Calculations

Based on the thorough discussion of the theoretical preliminaries in chapter 2, this part aims to demonstrate both the correctness of the implementations in the various computer codes as well as the physical validity of the multitude of approximations necessarily made to transform the intricate problem of electron-phonon interaction into a computationally feasible numerical procedure for calculating electronic transport properties. Although the physical motivations behind these approximations have already been discussed in as general a manner as possible, the overall quality of the results may not be appraised a priori.

Thus, in the first section 3.1, a detailed discussion of our calculations on the electron-phonon-induced temperature-dependent resistivity of copper is given as a convincing test regarding the implementations of the wave-vector-averaging of the self-energy in *fermint* and the Landauer-Büttiker formalism in the Gießen KKR code: On the one hand, the comparatively simple Fermi surface yields a valuable test system for the employed triangulation algorithms, on the other hand the resistivity of this particular metal is well studied and hence careful comparisons to experimental and theoretical data possible. This analysis, which is heavily based upon [124], will shed some light on the accuracies necessary for a valid treatment of all the different subsystems, and additionally will provide some information on whether it is sufficient to impose thermal expansion on the system to approximately account for the effects of anharmonic lattice vibrations in electronic transport calculations.

As an additional test system, aluminum is used in section 3.2 to double-check any conclusions drawn from the case of copper. Especially the strong dependence of the resistivity on the phonon structure will be further studied by contrasting a local with a generalized-gradient approximation to the exchange-correlation functional. A closing comparison to values obtained using Ziman's resistivity formula might serve as a rough "guesstimate" on the validity of a wave-vector-averaged self-energy despite aluminum having a more complicated Fermi surface.

Being convinced that the proposed calculational scheme yields a reasonable description of electron-phonon interactions in simple metallic bulk-like systems, the generalizability to iron-based magnetic tunnel junctions is investigated in section 3.3. Particularly Fe/MgO single barrier devices have been of great interest, as these systems exhibit a high tunnel magnetoresistance (TMR) ratio and hence are interesting candidates for applications such as read/write heads of modern hard disk drives (HDDs) and magnetic random access memories (MRAMs) [7–9]. Even higher TMR ratios that are, simultaneously, less dependent on the applied bias voltage may be observed in double barrier structures [6, 8]. Such devices are further believed to provide a simple tuning mechanism by exploiting the dependence of the

quantum well eigenenergies on the intermediate iron layer count [8, 85]. Due to limitations in one of the utilized third party codes, the display of magnetism will, however, make a different approach to the evaluation of the self-energy necessary. Therefore, after giving some introductory details of the interface structure as well as the physics in Fe/MgO single and double barriers, we discuss the approximate calculation technique of the self-energy. The chapter is then finalized by considering the effects of temperature-induced electron-phonon scattering on the resonant behavior of the electronic transport in Fe/MgO double barrier structures, thus providing first theoretical insights to this as of yet barely studied phenomenon.

3.1. Resistivity of Copper

Given that the intention of this section is to verify both theory and implementation, its structure obviously will mirror the organization of the previous chapter. The ordering is, however, slightly different: After modeling the thermal expansion of the solid using a Debye-Grüneisen curve, we proceed by analyzing the electronic and vibrational degrees of freedom. Subsequently, these results are combined to evaluate the electron-phonon induced electron linewidth. Based thereupon, we calculate the effective transmission probability and verify some expected physical properties of the temperature-dependent electrical resistivity.

3.1.1. Thermal Expansion

Although the available studies by Nix and MacNair [83] and Adenstedt [86] on fitting Debye-Grüneisen curves to experimental data for the true coefficient of thermal expansion of copper agree rather well on the parameters Q_0 and g [see equation (2.163) and the definitions (2.160)], they differ in the Debye temperature θ_D used in the evaluation of the heat capacity (2.168). Hence, in order to make sure the thermal expansion is well described, we perform the necessary optimization based on the data given in reference [87]. The optimal set of parameters is found to be $\theta_D \approx 322.37\,\mathrm{K}$, $Q_0 \approx 119.59 \times 10^3\,\mathrm{cal/mol}$, and $g \approx 2.96$ [124], which, except for g, coincides quite well with the corresponding values proposed by Nix and MacNair [83]. These values further prove to be insensitive with respect to the employed starting guess, hence strengthening the assumption that the optimization process was performed successfully.

A comparison of the fitted curve with the experimental data is given in figure 3.1 and shows excellent agreement [124]. For a quantitative analysis, the previously described parameterization is used to calculate the linear coefficients of expansion as reported in the references [83, 86, 88] and [89]. The relative deviations are below 2 % in the temperature range $-185.5\,^{\circ}\mathrm{C}$ to $500.1\,^{\circ}\mathrm{C}$ and therefore once more in very good agreement with our Debye-Grüneisen model [124]. In these calculations, the reference lattice constant is chosen equal to the value $a_{25\,^{\circ}\mathrm{C}} = 3.614\,91\,\text{Å}$ taken from reference [89]. Finally, in excellent agreement with [90], we predict the lattice

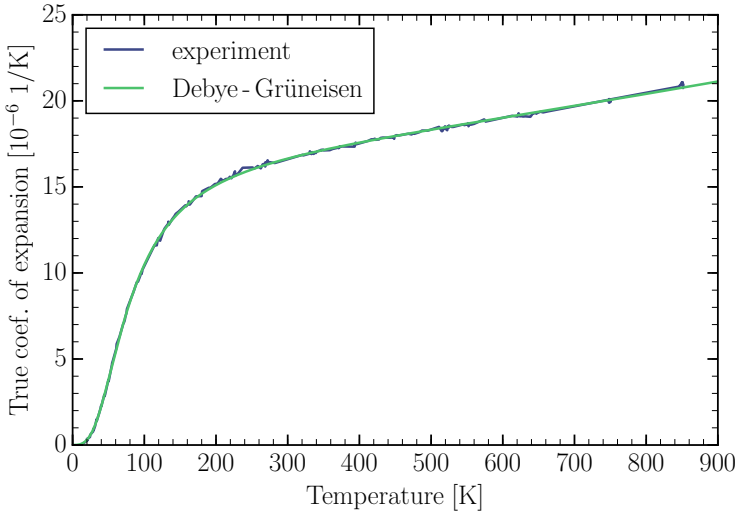

Figure 3.1.: True coefficient of thermal expansion of copper against temperature. The experimental data is taken from reference [87], the Debye-Grüneisen curve employs the parameters $\theta_D \approx 322.37\,\mathrm{K}$, $Q_0 \approx 119.59 \times 10^3\,\mathrm{cal/mol}$, and $g \approx 2.96$ [124].

constant of copper at absolute zero to be $a_{0\,\mathrm{K}} = 3.602\,90\,\text{Å}$ [124]. Other calculated lattice constants at various temperatures are given in table 3.1.

Based on these results and considering that the true coefficient of thermal expansion shows a near linear behavior for temperatures above room temperature it is justified to conclude that the Debye-Grüneisen curve may be used to extrapolate to values as high as 900 K, i.e., it correctly describes the thermal expansion of copper in the whole aspired temperature regime [124].

3.1.2. Electronic Structure

To accurately mimic the electron-phonon interaction, both electron and phonon structure must be described in sufficient detail. Hence, first the temperature dependence of the band structure is analyzed. As the electron-phonon vertices (2.116) are calculated by a generalized Fourier interpolation (2.144), the construction of a suitable set of maximally localized Wannier functions is discussed subsequently. Finally, the possibility of employing these Wannier functions to improve the equi-energy surface

T [K]	100	200	300	400	500	600	700	800	900
a [Å]	3.604	3.609	3.615	3.621	3.628	3.634	3.642	3.649	3.656

Table 3.1.: Lattice constants of copper at various temperatures as calculated by means of the proposed Debye-Grüneisen model.

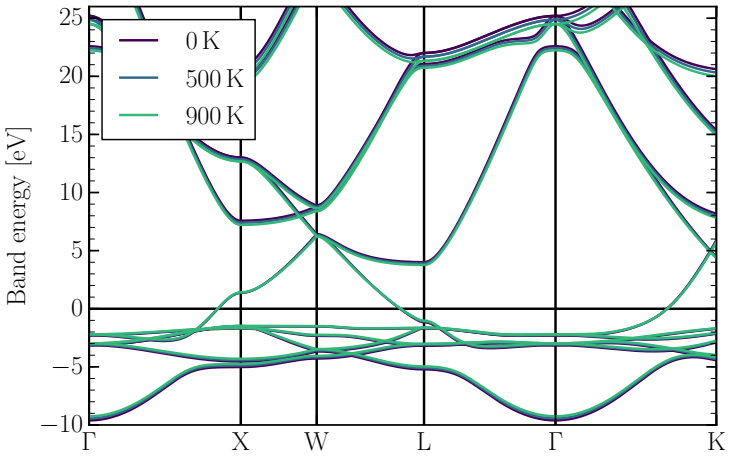

Figure 3.2.: Band structure of copper for three different temperatures (i.e., three different lattice constants) with aligned Fermi energies (each taken to be zero). With increasing temperature, the band structure is slightly contracted [124].

triangulations necessary for the wave-vector-averaging of the self-energy (2.148) are demonstrated.

Band Structure

The electronic structure calculations are performed using the third party code Quantum ESPRESSO [24]. Considering that 30–40 meV constitute the maximum order of typical phonon energies, it is reasonable to assume that very precise electronic structure calculations are necessary, the more so as the intermediate Wannier interpolation will most certainly introduce further deviations. We will therefore attempt to ensure a precision goal of 1 meV [124].

This may be achieved for all lattice constants in the range of 0 K to 900 K by using an energy cut-off of 80 Ry for the plane wave expansion of the pseudo wave function, corresponding to a cut-off of 320 Ry for the density. The exchange-correlation energy is treated in generalized-gradient approximation employing the parameterization of Perdew, Burke, and Ernzerhof [91]. Due to limitations of the EPW code, the calculations are performed using a norm-conserving pseudopotential of Troullier-Martins type [92]. The Brillouin zone integration is performed with a sampling of 280 $\underline{k}$ points in the irreducible wedge in conjunction with 20 mRy metallic occupation broadening in the model of Marzari-Vanderbilt [93].

The effects of thermal expansion on the band structure are displayed in figure 3.2 for the three different temperatures 0 K, 500 K, and 900 K. As the temperature increases, the Fermi energy E_F is monotonically decreasing, which is in the figure accounted for by aligning the electronic structures, i.e., the band energies are measured with respect to the corresponding Fermi energy, each. While the variations in the vicinity

of the Fermi energy are minimal, the dispersion relation shows a minor contraction with increasing temperature [124]. This is to be expected, because due to thermal expansion a rise in temperature will induce an increase in the lattice constant a. In the limit $a \to \infty$ the coupling of the atoms becomes ultimately negligible, and hence the electronic structure will tend to that of an isolated atom, i.e., it will show no dispersion at all.

Wannier Interpolation

In view of the comparatively small dependence of the electronic structure on the lattice constant, it is possible to use the very same parameters as input for the construction algorithm of maximally localized Wannier functions at each different temperature [124]. The proposed interpolation is based on the exhaustive study of Souza, Marzari, and Vanderbilt [46]: We employ the optimal subset $\mathcal{S}_7(\underline{k})$ containing five d-like and two tetrahedral-interstitial-centered Wannier functions as initial projections for the iterative optimization scheme, as this set yields a particularly good approximation of the sole dispersive s-like band in the vicinity of the Fermi energy [124]. To account for the missing band gap in metals, the maximum of the outer disentanglement window is chosen as 25.89 eV with respect to the Fermi energy, which represents an upper bound to the 12^{th} band. Further, a frozen energy window with a maximum value of 5.89 eV is introduced [124] to prevent the low-lying states from being affected by the minimization of certain[1] parts of the spread functional (2.143). The Wannier-interpolated band structure based on an equidistant 10^3 $\underline{k}$ point mesh is displayed in figure 3.3. It can be seen to be virtually identical to the *ab initio* result obtained using QUANTUM ESPRESSO at least within the frozen energy window [124].

Obviously, the quality of the interpolation will depend on the sampling of the set of all states, i.e., the Brillouin zone. To test this convergence, the eigenenergies are calculated on an equidistant 21^3 $\underline{k}$ point mesh spanning the whole Brillouin zone by means of QUANTUM ESPRESSO, and subsequently compared to their Wannier-interpolated counterparts, where the optimization process is based on a 6^3 $\underline{k}$ mesh, an 8^3 $\underline{k}$ mesh, a 10^3 $\underline{k}$ mesh, and a 12^3 $\underline{k}$ mesh, respectively. We find the coarse 10^3 $\underline{k}$ mesh to significantly improve over the smaller meshes, but to perform on par with the 12^3 $\underline{k}$ mesh at least with respect to its root-mean-square deviation (RMSD) of 13.6 meV near the Fermi energy [124]. Even though the deviations are of the same magnitude as the phonon eigenfrequencies, all following calculations on copper employ the Wannier interpolation based on the coarse 10^3 $\underline{k}$ mesh for two important reasons:

First, as discussed in section 2.3.3, the coarse meshes used to sample the electronic and vibrational systems must be commensurate, which drastically limits the set of computationally feasible meshes. Second, the energy-conserving delta functions in the electron linewidth equation (2.141) are evaluated based on the interpolated

[1] For details, we urge the reader to study reference [46].

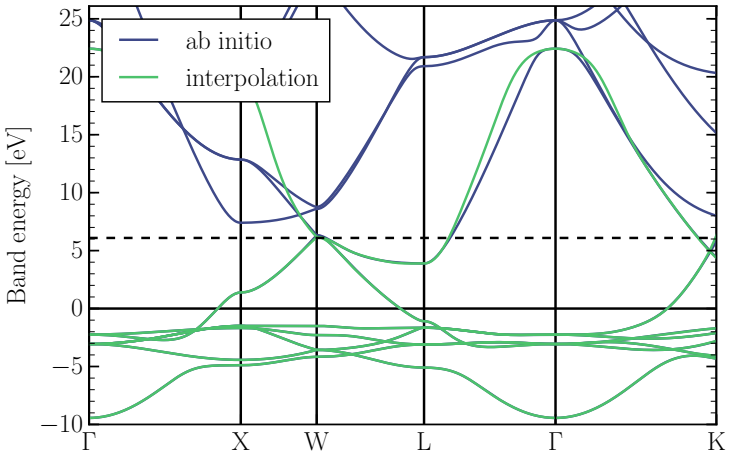

Figure 3.3.: Comparison of the *ab initio* band structure calculated at 500 K and the corresponding Wannier interpolation associated with five *d*-like and two two tetrahedral-interstitial-centered Wannier functions as proposed by Souza, Marzari, and Vanderbilt [46]. The dashed line indicates the frozen energy window [124].

values, and hence only relative differences determine the validity of the Brillouin zone integration. Additionally, in our numerical calculations the delta distributions are subject to Gaussian smearing. On average, this will further reduce the necessary accuracy of the interpolation [124].

Fermi Surface

It will be seen in section 3.1.5 that copper lends itself to the use of equation (2.78b), i.e., it is sufficient to restrict both transmission and self-energy calculations to the Fermi energy, only. To calculate the energy-resolved electron linewidth (2.148) in the next section we must therefore obtain the Fermi surface triangulation, evaluate the $\underline{k}$-resolved self-energy on this surface, and then average this quantity using appropriate weights.

Based on an equidistant $10 \times 10 \times 10$ mesh calculated using Quantum ESPRESSO as well as Wannier-interpolated 40^3 and 70^3 meshes, the Fermi surface of copper at 500 K is triangulated as discussed in subsection 2.3.4 and displayed in the left column of figure 3.4. Ideally, the band energy at a vertex would equal the Fermi energy, but as the surface vertices are calculated by means of an interpolation scheme, this is only approximately the case. The total deviations $\Delta E = E - E_F$ of the vertex energy to the Fermi energy are given by the color function and range from -124 meV to $+43$ meV for the coarsest mesh [124].

It is a striking feature that the total deviations of the vertex energies are directly connected to the curvature of the surface, especially for the 10^3 mesh: Whenever the surface has a positive curvature, the vertex energies are below the Fermi energy,

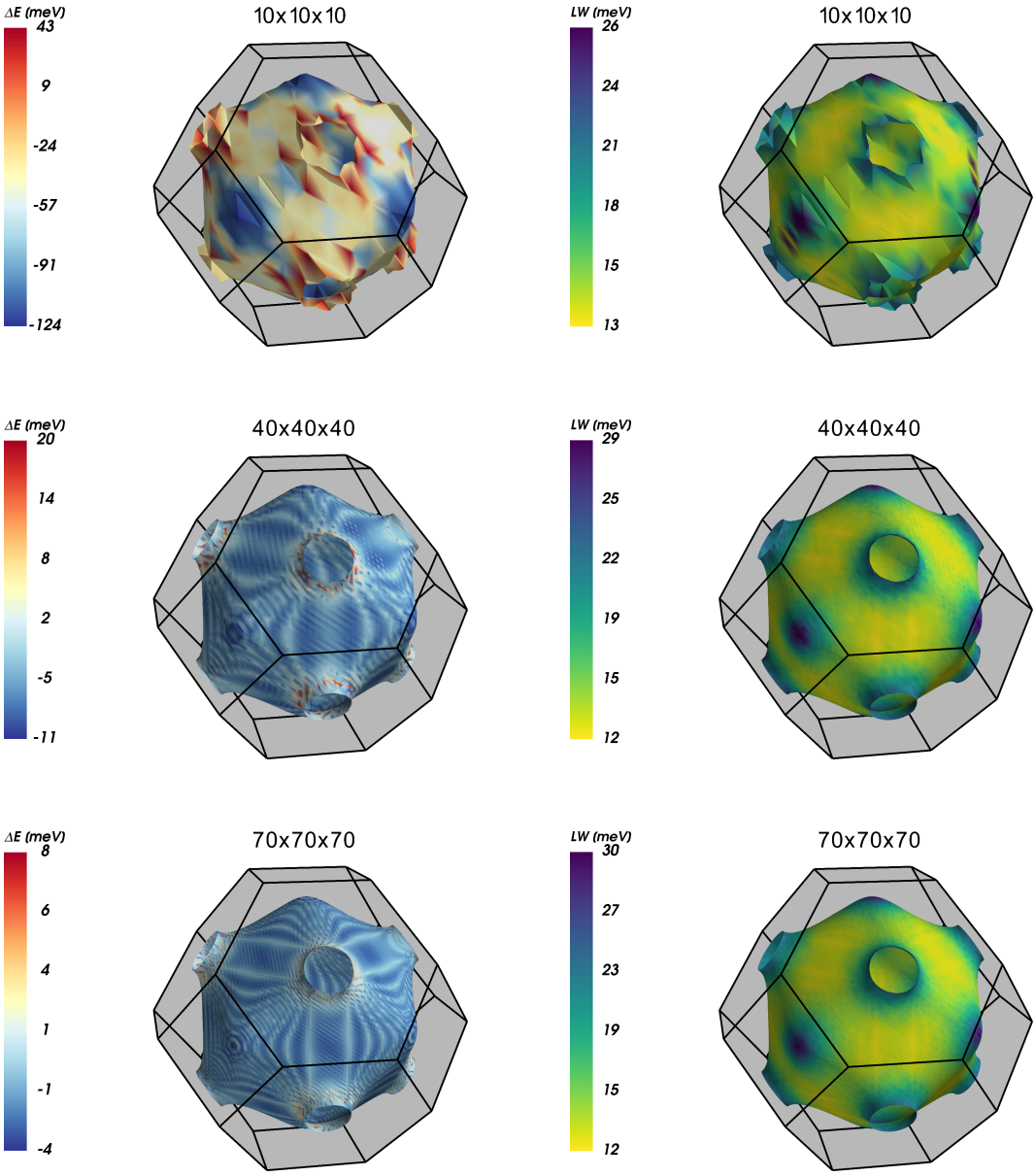

Figure 3.4.: Left column: Calculated Fermi surface triangulations at 500 K based on an *ab initio* $10 \times 10 \times 10$ mesh (top) and based on the Wannier-interpolated $40 \times 40 \times 40$ mesh (middle) and $70 \times 70 \times 70$ mesh (bottom). The color function yields the total difference of the vertex energies to the Fermi energy. Ideally, this difference should be zero. Right column: Electron linewidth at 500 K calculated on the very same Fermi surface triangulation used in the corresponding figure on the left. The magnitude is directly connected to the curvature of the surface [124].

and the same holds for interchanged signs. This is explained by noting that, as of now, only a *linear* interpolation scheme is implemented in *fermint*, which proves inadequate to predict values of highly curved dispersion relations [124].

This deficiency may of course temporarily be avoided by reducing the length scale for the linear interpolation, i.e., by basing the triangulation process on denser meshes.[2] Consequently, the deviation range of the 40^3 mesh is reduced to $-11\,\mathrm{meV}$ to $+20\,\mathrm{meV}$, and the deviations of the best mesh are even as small as $-4\,\mathrm{meV}$ to $+8\,\mathrm{meV}$ (see figure 3.4, left column). The importance of this observation will be discussed in subsection 3.1.4.

3.1.3. Phonon Dispersion

The second "ingredient" for a valid evaluation of the electron-phonon interaction is an accurate description of the vibrational degrees of freedom. Given that this analysis is built on the previously discussed electronic structure calculations and performed as described in subsection 2.3.3 using QUANTUM ESPRESSO, the convergence parameters are equal to those given in subsection 3.1.2.

Based on a coarse equidistant $\underline{q}$ mesh spanning the whole Brillouin zone, the phonon eigenfrequencies at an arbitrary wave vector may be calculated by Fourier interpolation [20]. We find that the quality of this interpolation is sufficiently good for all desired temperatures if meshes greater or equal to $6 \times 6 \times 6$ are used. Hence, to ensure the constraint of commensurate electron and phonon meshes, the dynamical matrices, displacement patterns and changes in the effective potentials are calculated on the symmetry-reduced equidistant $10 \times 10 \times 10$ mesh [124]. The interpolated phonon dispersion is displayed in figure 3.5 for the lattice constants corresponding to the three temperatures 0 K, 500 K, and 900 K, i.e., the phonons are treated in the quasi-harmonic approximation (see section 2.4).

While the general trend of the dispersion curve is in very good agreement with the experimental data at 296 K taken from reference [94], the magnitude of the eigenenergies is generally overestimated. This is most probably a consequence of using a GGA functional in conjunction with experimental lattice constants [124]: It was exemplified at least in the case of silicon that the dielectric screening calculated using a GGA functional is smaller than if an LDA functional is used [95]. According to Favot and Dal Corso [96] this result is compatible with our assertion in so far as a reduced capability of the electrons to screen the ion-ion interactions would induce higher interatomic force constants. It is further seen in figure 3.5 that an increase in temperature causes the phonon modes to soften, which may be explained by a decrease of the interatomic force constants with increasing atomic distances.

We finally note that, in our calculations, the "bare" phonon modes are overestimated

[2] This approach is severely limited by the necessary count of time-consuming self-energy evaluations: Exploiting symmetries, about 45 self-energy values have to be calculated for the triangulation based on the 10^3 mesh. This number increases to roughly 650 and 2000 vertices for the 40^3 and 70^3 mesh, respectively. Although a parallelization over vertices is possible and done, the implementation of a superior interpolation scheme is to be preferred.

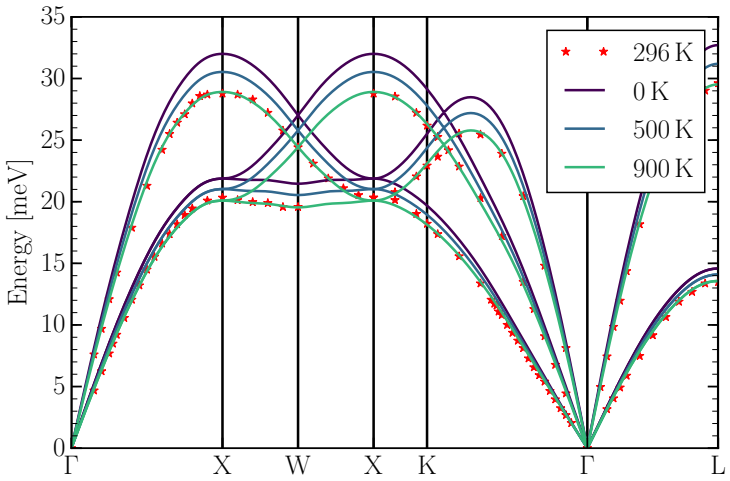

Figure 3.5.: Phonon dispersion of copper for 0 K, 500 K, and 900 K compared to experimental data [94] at 296 K. With increasing temperature, the phonon modes become weaker. The general overestimation is attributed to using a GGA pseudopotential in combination with experimental lattice constants [124].

throughout the whole Brillouin zone, but especially at Γ [124]. This is demonstrated in figure 3.6, where the phonon dispersion of copper at 500 K is plotted without imposing the acoustic sum rule during the interpolation process performed using Quantum ESPRESSO (graph labeled "no"). As pointed out by de Gironcoli [97], this behavior may yet again be accounted to the use of a GGA exchange-correlation functional, because the charge density energy cut-off of 320 Ry is in fact too small to ensure converged phonon frequencies in the Brillouin zone center.

When correcting for this issue with the sum rule algorithm "crystal," the phonon frequencies are exclusively mended in the vicinity of Γ, and hence the general overestimation is not suppressed. Even worse, an additional unphysical oscillation is introduced near Γ. The algorithm "simple," on the other hand, shifts the modes down in the whole Brillouin zone, thereby reducing the deviations to the fully converged result to less than 1 %. Calculating perfectly converged frequencies requires a charge density energy cut-off of 600 Ry and is therefore computationally rather expensive. Given that this would change the resistivity by less than 0.25 %, we refrain from doing so and instead employ the acoustic sum rule algorithm "simple" [124].

3.1.4. Electron Linewidth

Having calculated the electronic and phononic eigensystems on suitable coarse equidistant meshes spanning the Brillouin zone, we now proceed as described in subsection 2.3.3 and employ the generalized Wannier-Fourier interpolation as implemented in the EPW code [17, 43] to evaluate the self-energy integral (2.141) on very dense grids

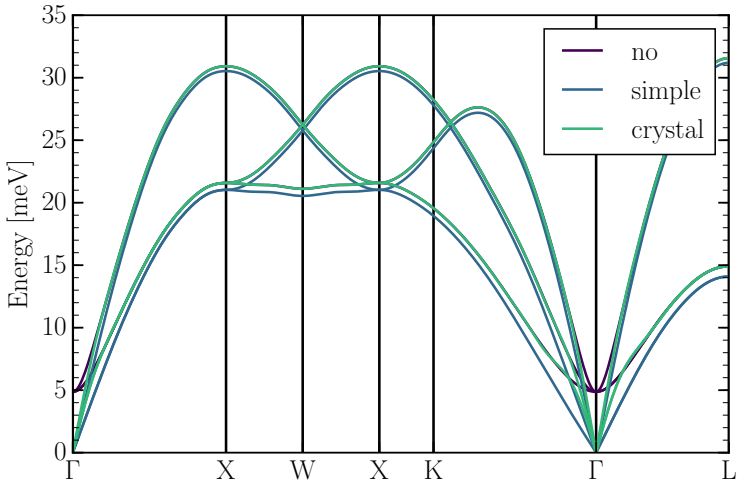

Figure 3.6.: Phonon dispersion of copper at 500 K calculated while not enforcing the acoustic sum rule at all (labeled "no") in comparison to the sum rule algorithms "simple," and "crystal." The latter algorithm leads to a minor but unphysical oscillation in the vicinity of the Γ point and otherwise does not affect the dispersion. In contrast, the sum rule "simple" shifts all phonon modes down in the whole Brillouin zone [124].

of supporting $\underline{q}$ points. Simultaneously, this procedure allows to restrict the linewidth calculations to the desired equi-energy surface triangulations, and subsequently to average over the electronic wave vector $\underline{k}$.

Although the $\underline{q}$ point sampling is already very fine, the delta distributions appearing in the integrand must always be replaced by Gaussian curves of appropriate widths to allow for negligibly small numerical energy deviations. The less supporting points are used, the bigger the typical deviations in energy may become, and hence the higher the necessary smearing (and vice versa). On the other hand, the smearing may not be chosen too big in order to avoid that many addends will wrongly contribute to the self-energy, which would result in an overestimation of the rather small linewidths especially at lower temperatures [124].

The required accuracy of the phonon wave vector sampling is counteracted by the averaging over all wave vectors constituting the equi-energy surface in so far as the more $\underline{k}$ points are taken into account, the better small numerical fluctuations in the self-energy values will compensate each other. All things considered, in the case of copper a valid trade-off is to use a 10 meV Gaussian broadening in conjunction with a 100^3 $\underline{q}$ mesh for the Brillouin zone integration at least for the two denser Fermi surface triangulations [124]. As the symmetry-reduced triangulation based on the 10^3 mesh typically consists of less than 50 vertices, the smearing is increased to 50 meV instead of improving the $\underline{q}$ point sampling. The effects arising from this decision towards computational efficiency will be discussed below.

	$\lvert \mathrm{Im}\, \Sigma_{n\underline{k}}(E_F, T) \rvert$ [meV]								
	$10 \times 10 \times 10$			$40 \times 40 \times 40$			$70 \times 70 \times 70$		
T [K]	min	max	avg	min	max	avg	min	max	avg
0	1.82	5.30	2.91	0.03	2.12	0.15	0.02	0.41	0.07
10	1.82	5.31	2.92	0.04	2.12	0.16	0.03	0.44	0.07
20	1.83	5.33	2.92	0.05	2.13	0.19	0.04	0.50	0.10
40	1.88	5.46	2.97	0.15	2.23	0.34	0.12	0.81	0.24
60	2.02	5.81	3.13	0.40	2.50	0.66	0.32	1.57	0.55
80	2.28	6.36	3.40	0.76	2.95	1.13	0.66	2.62	1.03
100	2.62	7.01	3.76	1.20	3.73	1.71	1.08	3.82	1.62
200	4.74	11.26	6.27	3.76	10.06	5.16	—	—	—
300	7.21	16.07	9.30	6.41	16.46	8.73	6.42	17.22	8.75
400	9.82	21.16	12.55	9.13	22.57	12.28	—	—	—
500	12.55	26.42	15.94	11.91	28.74	15.88	11.79	30.23	15.98
600	15.38	31.83	19.45	14.88	35.41	19.57	—	—	—
700	18.26	37.38	23.10	17.75	41.93	23.42	—	—	—
800	21.13	42.95	26.80	20.78	49.35	27.28	—	—	—
900	24.21	48.49	30.60	23.75	55.46	31.16	23.89	56.84	31.24

Table 3.2.: Minimum and maximum of the absolute value of the imaginary part of the electron-phonon self-energy on the three considered Fermi surface triangulations as well as averaged electron linewidth calculated using equation (2.148) against temperature. In the low temperature regime, the almost constant maximum values of about 5.3 meV and 2.1 meV for the 10^3 and 40^3 $\underline{k}$ mesh, respectively, indicate the systematic failure of the coarse triangulations.

For the three different considered Fermi surface triangulations, the wave-vector-resolved electron linewidth of copper at 500 K is displayed in the right column of figure 3.4. We find that the scattering rates are high whenever the absolute value of the surface curvature is high, and low otherwise [124]. Especially for the most coarse triangulations a striking coincidence with the deviations of the vertex energies to the Fermi energy is obvious, which leads to the assumption that the increased linewidth *might* yet again be a deficiency introduced by the linear interpolation scheme used to calculate the surface vertices. While a comparison by eye for the denser triangulations in the very same figure is inconclusive, the idea is substantiated by carefully studying the electron linewidth values presented in table 3.2, especially in the low temperature regime: The Fermi surface triangulation based on the $10 \times 10 \times 10$ mesh shows a near constant maximum value of about 5.3 meV for all temperatures below 40 K, which indicates a systematic error as the electron-phonon scattering rates must of course tend to zero with decreasing temperature. This incorrect constant maximum value shrinks to 2.1 meV and 0.4 meV with increasing mesh sizes, which were found to be directly related to smaller energy deviations during the discussion of the Fermi

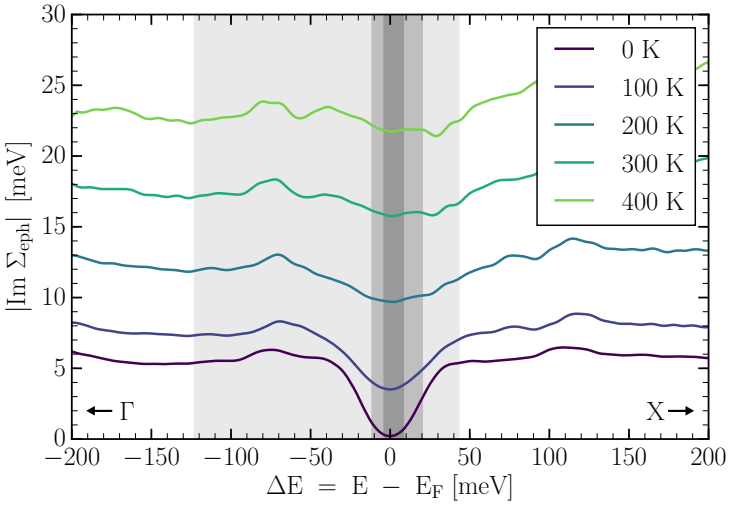

Figure 3.7.: Electron linewidth $|\mathrm{Im}\,\Sigma_{\mathrm{eph}}(\Delta E, E_F, T)|$ of copper at the Fermi energy for multiple temperatures T calculated along parts of the $\Gamma \to X$ path against the difference ΔE of the band energy $E(\underline{k})$ and the Fermi energy. For $T = 0\,\mathrm{K}$, the linewidth has a pronounced dip at the Fermi energy which is due to energy conservation [17]. This feature dissolves for higher temperatures. The shading in the background indicates the range of the energy deviations of the Fermi surface triangulation based on the $10 \times 10 \times 10$ mesh (light), $40 \times 40 \times 40$ mesh (medium), and $70 \times 70 \times 70$ mesh (dark) at absolute zero. The magnitudes are very similar in the whole temperature range (see, e.g., figure 3.4, left column).

surface triangulation in section 3.1.2. For higher temperatures, however, no such systematic change of the electron linewidth values with the triangulation quality is found.

To study this effect further, we calculate the electron linewidth of copper at various temperatures along parts of the $\Gamma \to X$ path in the Brillouin zone. When following this path in the vicinity of the Fermi energy, the band energy increases monotonically, as can be seen in figure 3.2 depicting the band structure. It is therefore possible to plot the linewidth against the total energy difference $\Delta E = E - E_F$ to the Fermi energy instead of plotting it against the corresponding $\underline{k}$ point of the path [124]. The resulting figure 3.7 then shows that for small temperatures, the electron linewidth has a pronounced "dip" near the Fermi energy. According to Poncé et al. [17], this feature is due to the energy conservation rule, which is enforced by the delta distributions in the electron linewidth relation (2.141). Nevertheless, this dip quickly dissolves with increasing temperature due to the additional thermal smearing [124].

The assumed connection between bad Fermi surface triangulations and elevated self-energies may now be understood in greater detail by comparing the total energy deviations ΔE of the vertex energies (indicated as shadings in the background of

figure 3.7) with the energy-difference dependence of the electron linewidth: Especially the deviations of the triangulation based on the 10^3 mesh are significantly too big to sample the electron linewidth exclusively in the dip range, and hence its (maximum) value will be overestimated for small temperatures. The triangulations based on the 40^3 and 70^3 meshes do, on the other hand, suffer considerably less from this issue, and therefore their low-temperature behavior is much better. Finally, the rather similar performance of all three Fermi surface triangulations at higher temperatures is readily explained by the vanishing of the dip [124].

Another noticeable feature is the near constant minimum value of the electron linewidth of about 1.8 meV up to 40 K as predicted by the Fermi surface triangulation based on the 10^3 mesh (see table 3.2). We mention in the beginning of this section that the electron linewidth of the coarse triangulation is calculated using a higher value for the Gaussian smearing in the Brillouin zone integration. In order to verify that this does in fact explain the error, the self-energy based on the 40^3 mesh is recalculated using a smearing of 50 meV. As expected, the minimum, maximum, and average value increase to about 1.60 meV, 3.45 meV, and 2.01 meV, respectively. Reducing the smearing in the calculations employing the triangulation based on the 10^3 mesh to 10 meV will, on the other hand, lower the minimum value to about 0.41 meV. Simultaneously, however, the maximum value will increase to 6.07 meV, which increases the average value to 4.27 meV. Hence, the higher smearing is considered *not* the cause for the failure of the coarse triangulation, but seen to correct for convergence issues as previously stated.

In conclusion, we find that an accurate sampling of the Fermi surface is necessary to correctly evaluate the electron-phonon self-energy in the low temperature regime, where "accurate" refers to small deviations of the vertex energies to the Fermi energy rather than a high density of the vertices [124]. For this to be possible, a good description of the electronic structure up to several meV in both the *ab initio* and Wannier interpolation steps is required. The linewidth evaluation itself has to be performed employing a Gaussian smearing sufficiently small to not interfere with the corresponding thermal fluctuations. At higher temperatures, the prerequisite of a valid description of the electronic structure seems less important. The observation that high Fermi surface curvature is linked to high scattering rates is accordingly not caused by numerical problems but physically meaningful [124]

3.1.5. Transmission and Resistivity

To verify the implementation of the Landauer-Büttiker formalism in the Gießen KKR Green's function code, we use the previously obtained electron linewidth to evaluate the temperature-dependent resistivity of copper. Given that, up to now, all numerical calculations have been performed in the framework of pseudopotential plane wave codes, this procedure consists of three steps: First, the effective one-particle potential $V_{\text{eff}}^{\{\underline{R}\}}(\underline{r})$ is obtained by solving the Kohn-Sham Hamiltonian (2.8) in a self-consistent manner. Subsequently, the Green's function (2.89) containing the electron-phonon self-energy is calculated and used to evaluate the various transmission functions (2.97)

and (2.100). Based thereupon, the effective transmission (2.76) and the resistance (2.78a) are calculated.

The effective Kohn-Sham potentials are obtained with an angular momentum cut-off of 3 in the expansions (2.47) of both the Green's functions of the repulsive[3] reference system as well as the real system. After having solved the algebraic Dyson's equation (2.54) for the screened reference system in real space taking 201 adjacent atomic sites into account, Dyson's equation for the Green's function of the real system is solved in reciprocal space by means of (2.57). The following Brillouin zone integration (2.58) uses 108^3 supporting points. In minor discrepancy with the electron linewidth calculations, the exchange-correlation energy E_{xc} is attributed for in the revised parameterization PBEsol [98] of the generalized-gradient approximation.[4]

After having solved for the effective potential, the three-dimensional bulk calculations are transformed into equivalent layer systems suitable to be treated in the non-equilibrium Green's function formalism presented in section 2.2. The domains $M_{L/R}$ of the decoupling potentials as introduced in the set of equations (2.82) are taken to coincide with the decimation block size of 8 layers, and the two-dimensional Brillouin zone integration (2.96) is, in analogy to the bulk calculations, performed using 108^2 $\underline{k}$ points in the surface Brillouin zone. In the course of this analysis we will study systems of high lengths, and in order to avoid numerical errors due to the neglect of the density contribution proportional to $\mathrm{Im}(z)$ [see equation (2.64)] the imaginary part of the energy is reduced to $2 \times 10^{-8}\,\mathrm{Ry}$. In consequence, Dyson's equation for the reference system has to be solved considering 603 neighboring sites to attain sufficiently converged results [124].

It was already mentioned and exploited that copper allows for restricting the transmission calculations to the Fermi energy E_F, only. To prove this it is – according to the discussion regarding the validity of equation (2.78b) – sufficient to show that the "curvature" of the effective transmission is small, where the concept of curvature is used in the sense of appendix A.4. Considering that we want to avoid calculating the self-energy for multiple energy values, it is however not reasonable to directly verify this condition. Instead, it is assumed in the following that the energy dependence of T_{LR}^{eff} will be quite similar to that of T_{LR}, which should hold if the self-energy is small in magnitude or not heavily dependent on the energy by itself. While the first of the two sufficient conditions is surely met for small temperatures, the latter will hold for higher temperatures as seen from figure 3.7.

Thus, in figure 3.8 the Fermi-Dirac difference function Δf as defined in equation (A.27) is plotted for the temperatures 100 K, 500 K, and 900 K in comparison to the energy-resolved ballistic transmission T_{LR}. In the displayed energy regime the

[3] The reference system is chosen to be described by a constant potential of 8 Ry in height.

[4] Considering that the PBEsol parameterization is specifically crafted to describe the exchange-correlation energy in a solid, it seems more appropriate for our bulk-like calculations than the PBE parameterization employed in all preceding calculations. A norm-conserving PBEsol pseudopotential as necessary for the EPW code is, however, not at hand, and hence we settle for the rather similar PBE parameterization. Please note that the presented KKR calculations are in fact rather insensitive to the particular choice of a GGA parameterization.

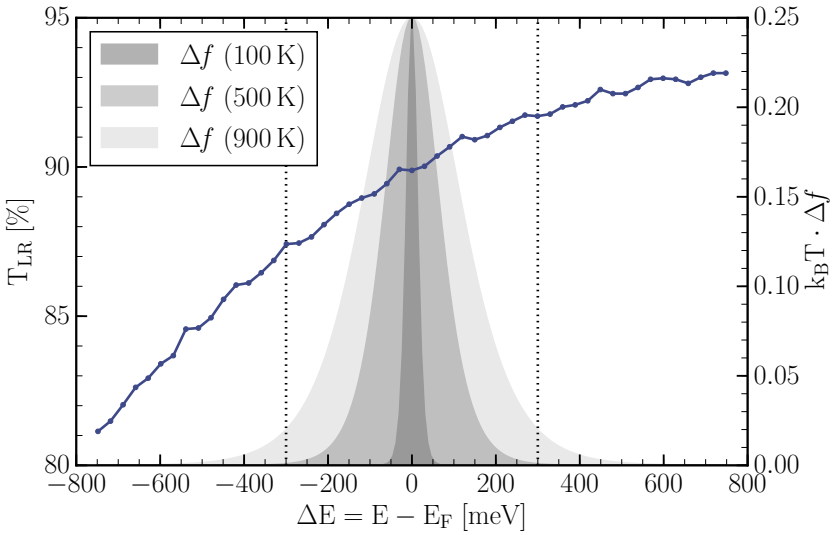

Figure 3.8.: Energy-resolved ballistic transmission T_{LR} [see equation (2.67); dots, line is to guide the eye] as well as Fermi-Dirac difference function Δf [see equation (A.27); shading] at 100 K (dark), 500 K (medium), and 900 K (light). The transmission function *does* have a nonvanishing curvature but may be, in good approximation, assumed linear in the regime $|\Delta E| \leq 300\,\text{meV}$ (indicated by dotted lines) [124].

transmission $T_{LR}(E)$ clearly *does* have a nonvanishing curvature. In the interval $|\Delta E| \leq 300\,\text{meV}$, on the other hand, it obviously is a valid approximation to assume the energy dependence linear. As the percentage of the area under the Δf curve outside of this energy range remains small for temperatures up to 900 K, the restriction of the transmission calculations to the Fermi energy is in fact considered justified for all aspired temperatures [124].

As was pointed out by Datta [34], in the limit of long device lengths the Landauer-Büttiker formalism includes Ohm's law, i.e., it correctly predicts the resistance R of the device to be a linear function $R(l) = R_0 + m \cdot l$ of its length l, where R_0 is the contact resistance introduced in equation (2.69). In systems of uniform cross section A the slope m is given in terms of the resistivity ρ as $m = \frac{\rho}{A}$. These experimentally well confirmed features yield another valuable test of our implementation, and hence the calculated resistance times area product $R \cdot A$ of copper at 500 K as a function of length is depicted in figure 3.9. It can be seen clearly that Ohm's law is valid at least for devices longer than 40 nm, but that the functional dependence is, as expected, not linear for relatively short conductors (see inset) [124].

The previously described behavior of the $R \cdot A$ curve is consistent over the whole aspired temperature regime, i.e., even for the lowest considered scattering rates the resistance depends in good approximation linear on device lengths greater 40 nm. For higher self-energies, the required length scales are even shorter. This motivates

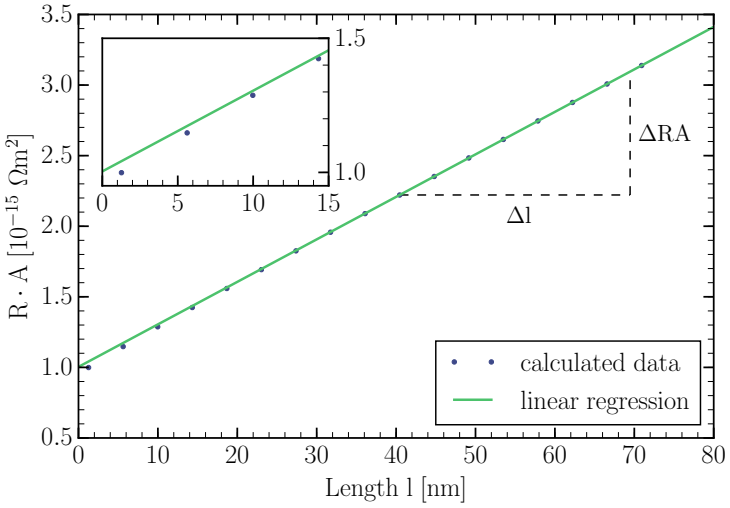

Figure 3.9.: Resistance times area product of copper as a function of device length calculated at 500 K. For device length greater 40 nm the dependence is near linear, and hence Ohm's law is valid for long devices. The inset shows the short length regime [124].

a simple yet physically appealing method to calculate the temperature dependence of the resistivity of simple metals: For each temperature of interest, the $R \cdot A$ value is sampled at various device length greater 40 nm, and subsequently the slope $\rho = {}^{\Delta RA}/_{\Delta l}$ is extracted from a linear regression analysis [124].

Based on the wave-vector-averaged electron linewidth values given in table 3.2, the resistivity is calculated by means of the aforementioned method and plotted as a function of temperature in figure 3.10 for each of the three considered Fermi surface triangulations. In comparison to experimental data taken from reference [99] we find very good agreement in all cases at least above room temperature. In the low temperature regime, however, the resistivities corresponding to the Fermi surface triangulation based on the 10^3 mesh fail to reproduce the correct behavior, i.e., the resistivity does not tend to zero. This is of course a remnant of the strong overestimation of the electron linewidth induced by the high deviations of the vertex energies to the Fermi energy as discussed in subsection 3.1.4. The same reasoning also explains why the resistivities obtained using the triangulation based on the 70^3 mesh improve over the results corresponding to the 40^3 mesh (see inset) [124].

Additionally we find [124] that our calculated resistivities corresponding to the two denser meshes are in better agreement with the experimental data than the values reported by Savrasov and Savrasov [10], which are obtained in the framework of the lowest-order variational approximation (LOVA) to the Boltzmann formalism. This is remarkable insofar as the LOVA is to be considered the *de facto* standard for DFT-based resistivity calculations in metallic systems. Furthermore, our predicted resistivities prove superior to those evaluated employing the alloy analogy [14].

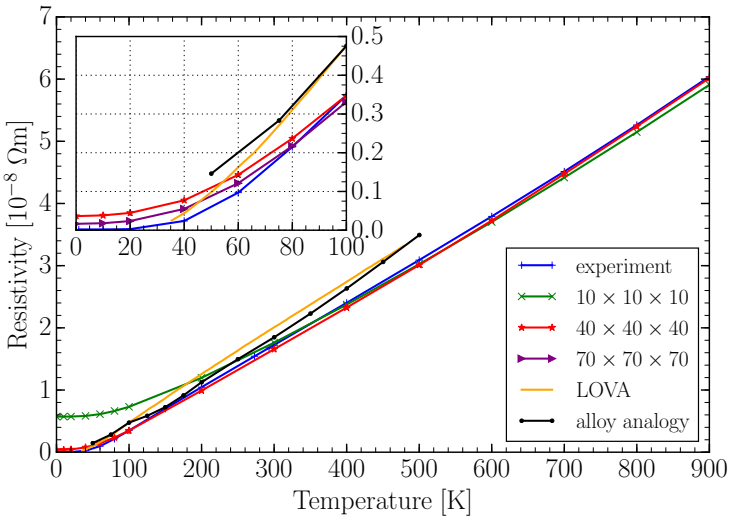

Figure 3.10.: Calculated resistivity of copper against temperature for the three considered Fermi surface triangulations in comparison to experimental data [99], lowest-order variational approximation (LOVA) to the Boltzmann formalism [10], and the alloy analogy [14]. While the most coarse triangulation fails in the low temperature regime, all meshes yield good to very good results for higher temperatures [124].

Studying this relative performance is particularly interesting, as the alloy analogy is another possibility to account for phase-breaking scattering in the framework of the Korringa-Kohn-Rostocker method, although this time based on the coherent potential approximation (CPA).

To study the effects of the imposed thermal expansion, figure 3.11 compares experimental resistivity data to values calculated employing the Fermi surface triangulation based on the 40^3 mesh under various assumptions. E.g., in the calculations to the dashed line (labeled "el. & ph. at 300 K") any effects of thermal expansion have been neglected at all, i.e., the lattice constant was kept fixed to its value at 300 K. In relation to the corresponding calculations taking thermal expansion into account, we find a minor overestimation of the result in the low-temperature regime, and a major underestimation for higher temperatures. This is consistent with the behavior of the true coefficient of thermal expansion (see figure 3.1): For small temperatures, the change in the lattice constant is rather small, and hence the effects on the resistivity will also be small. However, above room temperature the change in the lattice constant is not negligible [124].

Revisiting that the electronic structure shows only a minor temperature dependence (see figure 3.2) it is reasonable to attribute the observed underestimation of the resistivity to the atomic vibrations [124], the more so as this is to be expected from a phenomenological point of view: A smaller lattice constant leads to a increased ion-ion interaction and hence to higher interatomic force constants. Therefore, the

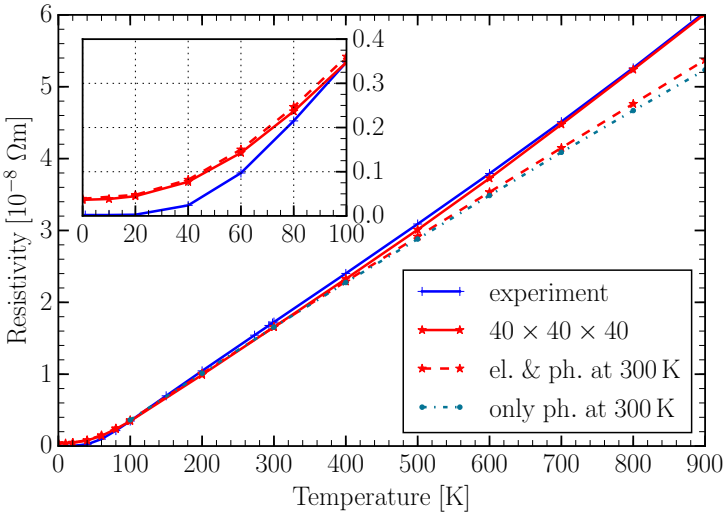

Figure 3.11.: Temperature-dependent resistivity of copper resistivity calculated using the Fermi surface triangulation based on the $40 \times 40 \times 40$ mesh in comparison to experimental data taken from [99]. The solid curve assumes the presence of thermal expansion, while the dashed curve (el. & ph. at 300 K) completely neglects this effect. The dash-dotted line (only ph. at 300 K) considers thermal expansion in the electronic structure, but not for the calculation of the phonon dispersion. In both latter cases, the slope is too low especially at higher temperatures [124].

phonon eigenfrequencies harden, as is consistent with the trend depicted in figure 3.5. Consequently, on average higher energy transfers are required in the interactions of electrons and ions, and hence bigger thermal fluctuations are necessary to induce scattering. In summary, the electron-phonon scattering rates at a specific temperature will decrease, which leads to smaller electrical resistances.

In order to verify this phenomenological reasoning, the dash-dotted curve (labeled "only ph. at 300 K") in figure 3.11 is calculated under the assumption that thermal expansion influences *only* the electronic structure, i.e., the phonon frequencies $\omega_{\underline{q}\nu}$ have been fixed to their respective values at 300 K [124]. In conformance with our considerations the curve shows even slightly higher deviations than the graph obtained by neglecting thermal expansion at all. Therefore, there actually is a small contribution of the electronic system — this is, however, dominated by the effects of the (missing) phonon softening [124].

In conclusion, the demonstrated accuracy of restricting the transmission calculations to the Fermi energy at all considered temperatures in retrospect legitimates to only evaluate the electron linewidth on the Fermi surface. As expected, the most coarse triangulation fails in the low temperature regime due to its overestimation of the magnitude of the electron-phonon self-energy, while the denser triangulations yield better resistivities than those obtained using established methods. The well

recognized Ohm's law is a limiting case of the proposed method for high device length, and hence both method and implementation are found to be valid at least in the case of copper. Finally, for a correct evaluation of the electrical resistance at higher temperatures it is crucial to carefully account for any changes in the phonon dispersion induced by the anharmonicity of the atomic vibrations. To do so in copper, it is sufficient to impose thermal expansion on the system.

3.2. Resistivity of Aluminum

Motivated by the impressive accuracy of the proposed method in the case of copper for temperatures as high as 900 K, this section tries to verify any conclusions drawn – especially the proposed crucial role of precise phonon calculations – by studying the temperature-dependent resistivity of aluminum. The analysis therefore proceeds along the very same lines as in the previous section, but in each step the differences arising from LDA and GGA exchange-correlation functionals are discussed. Finally, our findings are underlined by comparing the resistivities obtained within the non-equilibrium Green's function framework to those evaluated using Ziman's formula in the context of the Boltzmann formalism.

3.2.1. Thermal Expansion

The thermal expansion is once again treated in the Debye-Grüneisen model (2.163). Instead of performing the optimization procedure by ourselves, we this time rely on the parameter set proposed by Nix and MacNair [83], i.e., $\theta_D = 400\,\mathrm{K}$, $Q_0 = 83.6 \times 10^3\,\mathrm{cal/mol}$, and $g = 2.7$.

If we calculate the true coefficient of thermal expansion in the temperature range 15 K to 27 K using this parameterization, we find relative deviations in the order of 10 % compared to the values reported by McLean [100]. For even lower temperatures, the relative errors significantly increase. Given, however, that the true coefficient of thermal expansion must be small in this region, this is to be expected and – within the scope of this work – not an issue. In conformance with these results, the lattice constant of aluminum at absolute zero is estimated to be $a_{0\,\mathrm{K}} = 4.0241\,\text{Å}$, which is about 0.2 % smaller than the value predicted in reference [90]. Other calculated lattice constants are virtually identical with those in reference [101], i.e., we find relative deviations of less than 0.1 %.

In summary, these results confirm the conclusion drawn in the case of copper that thermal expansion may be modeled in this way. The lattice constants used in the following analysis may be found in table 3.3.

3.2.2. Electronic Structure

In the employed plane wave codes, the LDA and GGA exchange-correlation functionals are introduced by using two different pseudopotentials: For comparability with our previous results, the generalized-gradient approximation is yet again treated in the

T [K]	100	200	300	400	500	600	700	800	900
a [Å]	4.026	4.033	4.042	4.051	4.062	4.073	4.085	4.097	4.110

Table 3.3.: Lattice constants of aluminum at various temperatures as calculated by means of the Debye-Grüneisen model proposed by Nix and MacNair [83].

parameterization of Perdew, Burke, and Ernzerhof [91] on top of a norm-conserving pseudopotential of Troullier-Martins type [92]. As local approximation we utilize a norm-conserving pseudopotential of Goedecker-Hartwigsen-Hutter-Teter type [102, 103] which was generated using the LDA parameterization of Perdew and Zunger [104].

The convergence parameters are chosen identical for both potentials in order to facilitate the reasoning that differences in the result are due to the two types of potentials.[5] For all considered temperatures a pseudo wave function energy cut-off of 140 Ry and a corresponding charge density energy cut-off of 560 Ry is sufficient to reach convergence. The Brillouin zone integration is performed with 408 $\underline{k}$ points in the irreducible wedge in conjunction with a Methfessel-Paxton first-order spreading [105] of 20 mRy to account for the metallic occupation broadening.

For both LDA and GGA, the band structure as well as the employed Wannier interpolation of the GGA results are given in figure 3.12. The two *ab initio* band structures prove to be very similar, and hence it is possible to use the same initial projections for the corresponding optimization procedure of the maximally localized Wannier functions. However, because of the band crossing in the direct vicinity of the Fermi energy (see inset of figure 3.12), these projections need to be carefully crafted in order to yield an accurate interpolation.

Based on the results described in reference [106], we find the 9 *s*-, *p*- and *d*-like atom-centered Wannier functions to be a suitable starting guess for the minimization of the spread functional (2.143). The quality of the Wannier interpolation is strongly dependent on the successful disentanglement of the band structure, which is accounting for the missing band gap in metals. Thus, the result may be further improved by restricting the *ab initio* calculations of eigenstates and eigenvalues to 10 bands while simultaneously setting the outer disentanglement window to the maximum value of the 10^{th} band. As the band structure is slightly contracted with increasing lattice constant, this value is temperature-dependent, but may be automatically determined by analyzing the electronic structure before starting the optimization process.

To study the necessary sampling of the Brillouin zone, we adapt the test described in the case of copper, i.e., the eigenvalues on a 21^3 $\underline{k}$ point mesh are calculated using Quantum ESPRESSO and subsequently compared to the interpolated values

[5] Given the rather small number of available pseudopotentials and the elimination of parameterizations not implemented in the Gießen KKR code, we have to use different types of norm-conserving pseudopotentials. Further, different parameterizations of local and generalized-gradient approximations might perform differently. Although somewhat sloppy, we will not study these effects within this work, but nevertheless refer to the two pseudopotentials as LDA and GGA.

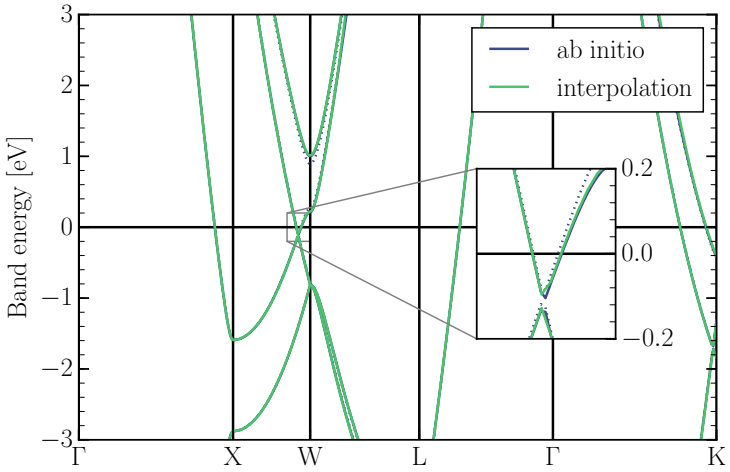

Figure 3.12.: *Ab initio* band structure employing a GGA (solid) and LDA (dotted) exchange-correlation functional in comparison to the Wannier interpolation based on the GGA calculations. Due to the band crossing in the vicinity of the Fermi energy (see inset as well as the comment in footnote 6), great care must be taken to ensure a valid interpolation for the Fermi surface calculation.

based on a 6^3 $\underline{k}$ mesh, an 8^3 mesh, a 10^3 mesh, and a 12^3 mesh. While the 8^3 mesh significantly improves over the 6^3 mesh, it performs with similar accuracy compared to the denser meshes especially for the "higher" band.[6] The maximum deviations are below 23 meV and the RMSD is bounded by 7 meV, which even excels the interpolation quality of copper. Hence, all Wannier interpolations used in the following calculations will be based on an $8 \times 8 \times 8$ $\underline{k}$ mesh.

Because of the band crossing near the Fermi energy, rather dense meshes are required for a valid triangulation of the Fermi surface. This is true in particular for the "higher" band, although its contribution to the Fermi surface area is quite small, and the error caused by this effect should hence be equally small.[7] For both LDA and GGA, the RMSD to the Fermi energy of the "lower" band is less than 14 meV for

[6] Instead of employing symmetry arguments to distinguish "physical" bands, all calculated eigenvalues are simply ordered by size, and the position in this sequence is identified with a band index. Hence, in the following, we denote the eigenvalues corresponding to the upper curve of the inset in figure 3.12 as "higher" band, and those corresponding to the lower curve of the inset as "lower" band, although this classification neglects that actually two monotonic curves or bands intersect one another. Please further note that the "lower" band does not cross the Fermi energy within the inset region but, e.g., on the $\Gamma \to X$ path (see figure 3.12).

[7] Given that we refrain from plotting the energy deviations of the triangulations as done for copper, we refer the reader to figure 3.14: The "higher" band consists of the multitude of "patches" at the borders of the Brillouin zone, and hence has a much smaller area than the "lower" band. When employing the triangulation based on a 40^3 mesh (left), these patches are still rather serrated. If, on the other hand, a 100^3 mesh is used as a basis for the Fermi surface triangulation (right), the quality improves by far.

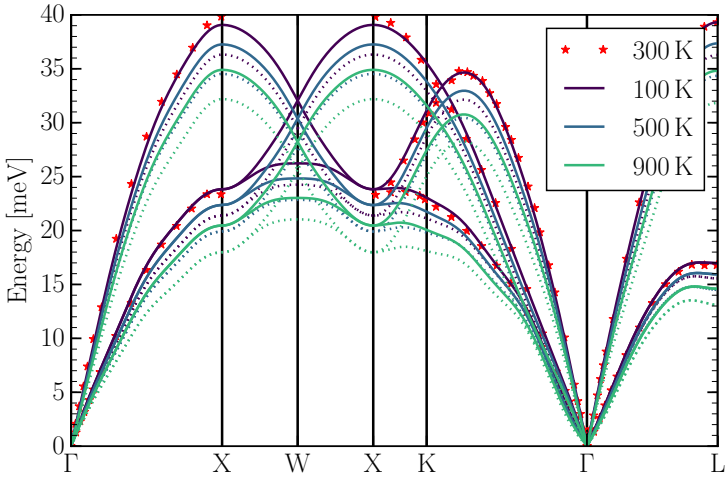

Figure 3.13.: Phonon dispersion of aluminum for 100 K, 500 K, and 900 K compared to experimental data [107] at 300 K (stars). Both GGA (solid) and LDA (dotted) do generally underestimate the experimental data. Nevertheless, the GGA pseudopotential shows much smaller deviations to the experimental results.

the triangulation based on a 40^3 mesh in the whole temperature range. The "higher" band is described with energy deviations of less than 40 meV RMSD. In case of the triangulation based on a 100^3 mesh, the RMSDs of both bands are below 9 meV. We therefore conclude that by using these triangulations, the electronic structure is described to similar accuracy as in the previous calculations.

3.2.3. Phonon Dispersion

Similar to the case of copper, the grid size of the equidistant $\underline{q}$ mesh does not drastically influence the quality of the Fourier interpolation used to calculate the phonon dispersion in the whole Brillouin zone. Hence, to ensure a mesh commensurate to the electronic subsystem as is necessary for the electron linewidth evaluation, an $8 \times 8 \times 8$ mesh is used. In view of the assumed importance of a valid description of phonons, the convergence parameters given in section 3.2.2 are this time carefully chosen to yield converged eigenfrequencies, particularly at Γ. This choice is due to the fact that although we find that the acoustic sum rule algorithm "simple" suitably corrects for convergence problems in copper, we do not want to risk that numerical issues might interfere with our examinations of the differences due to the LDA and GGA exchange-correlation functionals.

The phonon dispersion at the three different temperatures 100 K, 500 K and 900 K along several high-symmetry paths in the Brillouin zone is given in figure 3.13. In comparison to experimental data at 300 K taken from reference [107], we find

that the GGA functional slightly[8] *under*estimates the eigenfrequencies, even though experimental lattice constants are used. This observation seems to conflict with our findings in the case of copper, but is rectified by noting that the LDA functional performs even worse, i.e., it considerably underestimates the phonon dispersion.

In view of the minor dependence of the electronic structure on the type of exchange-correlation functional, to support our conclusions drawn in the previous section one would expect that the electron linewidth and hence the resistivities will be highly overestimated if calculated with the LDA functional. In the following, this will be analyzed in more detail.

3.2.4. Electron Linewidth

Based on the previous results concerning the electronic and vibrational structure of aluminum, we now turn to evaluate the electron linewidth as explained in subsection 2.3.3. In conformance with our course of action in case of copper, the self-energy will be calculated at the Fermi energy only. The justification of this approach, i.e., the proof of the validity of equation (2.78b), will be postponed to the discussion of the resistivity curves in subsection 3.2.5.

Considering our findings in subsection 3.1.4 that a Gaussian smearing of 50 meV proved too large for an accurate Brillouin zone integration in equation (2.141), the electron linewidth is yet again calculated using a broadening of 10 meV. Under these circumstances, 60^3 supporting $\underline{q}$ points are sufficient to converge the wave-vector-averaged self-energy for triangulations based on equidistant meshes consisting of 40^3 $\underline{k}$ points and more. This value is considerably lower than the employed Brillouin zone sampling of 100^3 $\underline{q}$ points in the case of copper, which is most probably an effect caused by the increased complexity of the Fermi surface: The symmetry-reduced vertex count of the Fermi surface triangulation of aluminum based on the 40^3 mesh is comparable to the respective vertex count of the Fermi surface triangulation of copper based on a 70^3 mesh, and therefore the error canceling due to the electronic wave-vector-averaging is superior.

A comparison of the GGA results to the wave-vector-resolved electron linewidth of aluminum at 500 K for the two considered Fermi surface triangulations based on the 40^3 mesh (left) and the 100^3 mesh (right) is given in figure 3.14. The general trend of the linewidth as calculated using an LDA functional is virtually identical, although the magnitude of the values is generally higher. At least for the "lower" band we can confirm that high surface curvature is directly related to elevated self-energy magnitudes, as was found in case of copper. This feature is slightly more pronounced in the LDA calculations due to an enlarged range between minimum and maximum value. For the "higher" band, however, this assumption remains inconclusive.

To allow for a more detailed discussion, the minimum, maximum, and wave-vector-averaged value of the electron linewidth of both LDA and GGA for the triangulation based on the 40^3 mesh as well as the GGA result for the triangulation based on the

[8] Please note that the coefficient of thermal expansion is small for low temperatures, and hence the dispersion relations for 100 K and 300 K will be rather similar.

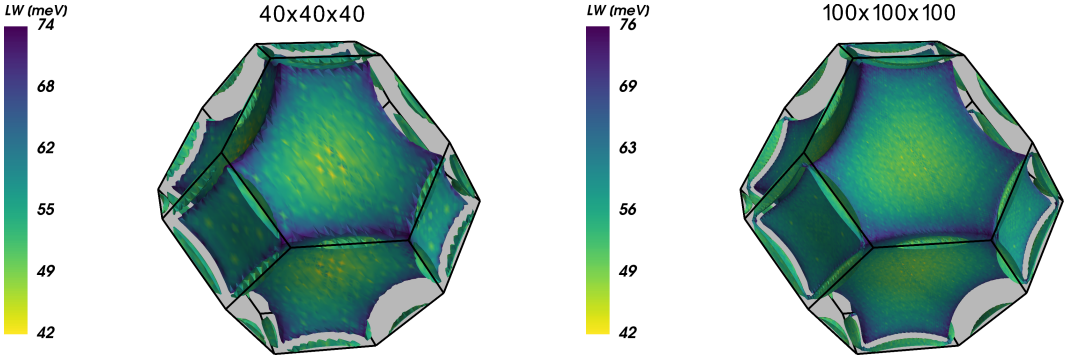

Figure 3.14.: Electron linewidth of aluminum at 500 K for the two considered Fermi surface triangulations based on an equidistant $40 \times 40 \times 40$ mesh (left) and on the finer $100 \times 100 \times 100$ mesh (right). Especially the serrated surface of the "higher" band is much improved in the latter calculations. For the "lower" band, the magnitude of the linewidth is connected to the curvature of the surface.

100^3 mesh are given in table 3.4 at various temperatures. In conformance with our previous observations, the values obtained using an LDA functional are generally bigger, and the range between minimum and maximum value is increased in the whole temperature range. This further substantiates the assumption that the strong underestimation of the phonon dispersion in case of LDA drastically influences the electron-phonon scattering rates.

Finally, the near constant maximum value of the electron linewidth for temperatures below 60 K indicates once more the presence of the energy-conservation-induced [17] dip in the self-energy near the Fermi energy. Similar to our findings in the case of copper, the band energies along parts of the $\Gamma \to X$ and $\Gamma \to L$ paths in the vicinity of the Fermi energy behave monotonic (see figure 3.12), and hence it is possible to generate the analog of figure 3.7. For both LDA and GGA we find that the width of the dip is virtually identical to the one observed for copper. The effect of sampling the self-energy outside the dip region is, however, more severe, because the electron linewidths are this time in the order of 15 meV and hence at least two times larger than the corresponding values in figure 3.7.

In conclusion, the observed behavior of the electron linewidth is perfectly similar to the results presented in the case of copper: In the low temperature regime an accurate triangulation of the Fermi surface is necessary in order to sample the self-energy in the dip region, i.e., in the vicinity of the Fermi energy, the more so as the magnitude of the linewidth is much larger in case of aluminum. The increased complexity of the Fermi surface allows, on the other hand, for the use of a comparatively coarse $\underline{q}$ point sampling. For higher temperatures the constraint of precise Fermi surface triangulations is yet again released. The differences in the LDA and GGA self-energy calculations are significant and attributed mostly to the discrepancies in the vibrational degrees of freedom.

	$\left\lvert \mathrm{Im}\,\Sigma_{n\underline{k}}(E_F,T) \right\rvert$ [meV]								
	LDA			GGA					
	$40 \times 40 \times 40$			$40 \times 40 \times 40$			$100 \times 100 \times 100$		
T [K]	min	max	avg	min	max	avg	min	max	avg
0	0.03	24.20	2.08	0.02	19.45	1.38	0.02	10.67	0.16
10	0.05	23.94	1.89	0.02	19.34	1.41	0.02	15.70	0.21
20	0.07	24.33	2.02	0.04	19.30	1.45	0.04	13.01	0.23
40	0.30	24.46	2.36	0.17	20.82	1.77	0.16	12.88	0.51
60	0.93	24.68	3.31	0.59	19.76	2.45	0.59	15.44	1.27
80	2.04	25.18	4.86	1.41	21.53	3.50	1.41	13.96	2.38
100	3.34	26.89	6.84	2.64	22.17	5.08	2.65	13.00	4.06
200	12.54	38.77	20.98	12.08	31.44	16.48	12.20	24.60	15.95
273	—	—	—	18.26	40.44	26.11	18.51	36.81	25.88
300	26.29	54.56	37.15	20.38	44.92	29.68	21.04	39.92	29.57
400	40.72	71.59	53.92	29.38	59.77	43.34	30.06	57.74	43.54
500	55.98	94.78	71.61	42.25	74.48	57.60	42.28	76.22	57.94
600	74.53	116.32	90.37	57.60	93.88	72.53	57.21	96.23	72.96
700	91.37	145.10	110.31	69.18	114.55	88.44	69.38	118.08	88.66
800	106.73	170.73	131.26	84.51	134.70	105.28	83.93	140.75	105.56
900	127.68	201.68	153.73	103.14	158.78	123.39	98.91	163.15	123.67

Table 3.4.: Minimum, maximum and wave-vector-averaged value of the electron linewidth for the Fermi surface triangulation based on the $40 \times 40 \times 40$ mesh using both LDA and GGA, as well as the corresponding values of the GGA calculations performed for the finer triangulation based on the $100 \times 100 \times 100$ mesh. In the low temperature regime, the near constant maximum values indicate the presence of the characteristic dip in the vicinity of the Fermi energy. In general, the LDA pseudopotential predicts higher scattering rates.

3.2.5. Temperature-dependent Resistivity

As discussed in more detail in subsection 3.1.5, we start the analysis by obtaining the effective one-particle potentials $V_{\mathrm{eff}}^{\{\underline{R}\}}(\underline{r})$ as a prerequisite to our transport calculations. All Green's functions are calculated using an angular momentum cut-off of 3. After having solved the algebraic Dyson's equation for the Green's function of the constant 8 Ry reference potential on real space clusters consisting of 201 adjacent atomic sites, the Green's function of the physical system is evaluated in reciprocal space using 120^3 supporting $\underline{k}$ points in the subsequent Brillouin zone integration. For consistency with the pseudopotential plane wave calculations described above the generalized-gradient approximation is treated in the PBE parameterization [91], and the LDA parameterization is due to Perdew and Zunger [104].

In the corresponding transport systems, the domains $M_{L/R}$ of the decoupling

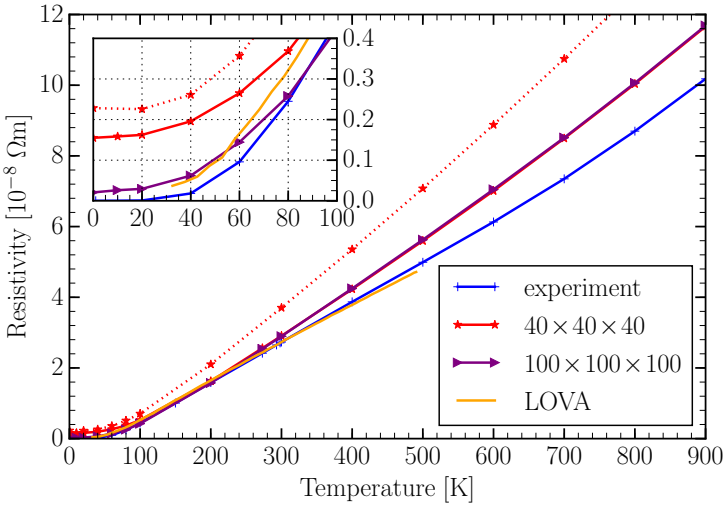

Figure 3.15.: Temperature-dependent resistivity of aluminum for the two considered Fermi surface triangulations in comparison to experimental data [99] and the LOVA to the Boltzmann formalism [10]. Both GGA results (solid) mirror the experimental data up to 200 K rather well, but overestimate for higher temperatures. In contrast, the LDA result (dotted) is too big in the whole temperature regime.

potentials coincide yet again with the decimation block size of 8 layers. It is, however, sufficient to perform the Brillouin zone integration with 96^2 sampling points, and the imaginary part of the energy may be chosen as high as $\mathrm{Im}(z) = 2 \times 10^{-7}$ Ry in order to converge the resistivity calculations to less than 1 % for even the smallest scattering rates. Therefore, the algebraic Dyson's equation for the Green's function of the screened reference system may be solved taking only 459 neighboring sites into account.

Akin to what was stated in the case of copper, Ohm's law is valid for device lengths greater 45 nm in the whole aspired temperature regime. Despite the generally higher electron linewidth in aluminum, the lower bounds are of similar order, which is understood by noting that in the low-temperature regime the scattering rates are, in fact, comparable in size. It is further confirmed that higher scattering rates reduce the required length scales. Given, however, that the transmission calculations are computationally rather inexpensive, this is not exploited and the resistance times area products necessary for the evaluation of the resistivities are obtained using the very same layer count at all temperatures.

The LDA (dotted) and GGA (solid) resistivity calculations are depicted in figure 3.15 in comparison to experimental data taken from reference [99] as well as to results in the lowest-order variational approximation to the Boltzmann formalism reported by Savrasov and Savrasov [10]. In case of the GGA exchange-correlation functional, the values corresponding to both the 40^3 and 100^3 mesh show only minor

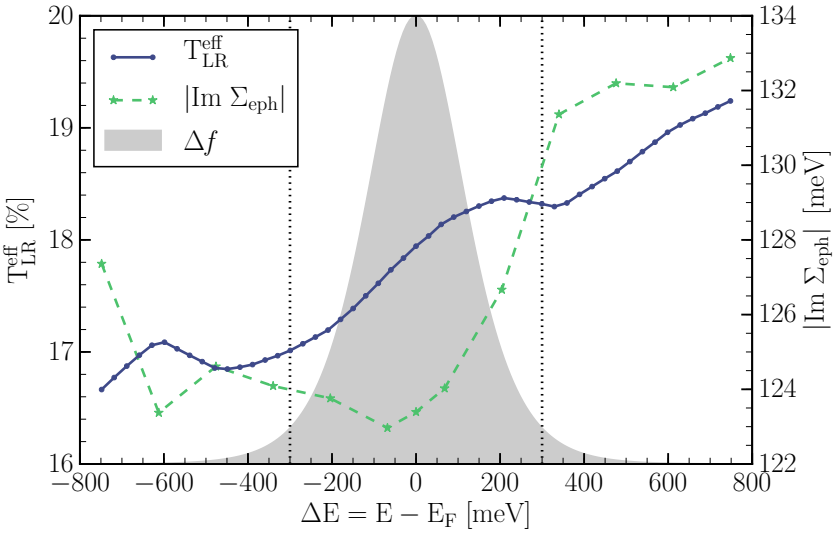

Figure 3.16.: Energy-resolved effective transmission (solid line) of aluminum at 900 K calculated using a linear interpolation of the corresponding electron linewidth (dashed line). The monochromatic shading in the background illustrates the behavior of the Fermi-Dirac difference function Δf at this very temperature. The transmission is essentially antisymmetric in the range $|\Delta E| \leq 300\,\mathrm{meV}$.

discrepancies to experiment for all temperatures up to 200 K, but then start to systematically overestimate. In conformance to what is seen in the case of copper and the previous discussions of the electron linewidth results, the resistivities calculated using the denser mesh prove superior due to the more accurate sampling of the self-energy in the dip region. In further agreement, both triangulations perform virtually identical at higher temperatures where the dip has smeared out. As expected when studying table 3.4, the LDA results overestimate the resistivities in the whole temperature regime. However, analogous to the GGA calculations, the differences to the experimental data grow with increasing temperature.

While this behavior does substantiate to some extent the assumption that the underestimation of the phonon energies is the main cause of error, there are several other conceivable reasons for the failure at higher temperatures. In particular, the observation that the range between the minimum and maximum value of the electron linewidth grows with temperature (see table 3.4) might indicate that the proposed wave-vector-averaging might fail in the high temperature regime. Given, however, that it is very hard to estimate the magnitude of the introduced deviation without being able to calculate the $\underline{k}$-resolved result, we will postpone the discussion to the end of this section and first discuss the other more manageable possibilities.

Considering that the overestimation of the resistivity increases with temperature for both LDA and GGA, the problem could be induced by an erroneous usage of the

resistance formula (2.78b): For elevated temperatures, the Fermi-Dirac difference function Δf defined in equation (A.27) will spread in energy, and hence higher-order contributions to the transmission function will become more important, i.e., curvatures previously considered "small" might actually influence the result significantly. To verify that this is *not* the case, we present in figure 3.16 the energy-resolved effective transmission[9] of aluminum at 900 K (solid line) in comparison to the corresponding weighting function Δf. The behavior of $T_{LR}^{\text{eff}}(E)$ is primarily antisymmetric with respect to the Fermi energy, and the quadratic contribution hence is negligible in the important energy range $|\Delta E| \leq 300\,\text{meV}$. Consequently, the resistivity calculated taking the full energy dependence into account is $11.709 \times 10^{-8}\,\Omega\,\text{m}$, and thus in fact 0.5 % higher than the corresponding value of $11.661 \times 10^{-8}\,\Omega\,\text{m}$ obtained by reducing the transmission calculations to the Fermi energy.

Another and quite likely possibility to introduce a temperature-dependent error as observed would be an overestimation of the phonon softening due to the anharmonic ion-ion interactions. While it was demonstrated in case of copper that these effects may be adequately modeled by imposing thermal expansion on the system, this needs not necessarily be true for aluminum, the more so as the upper bound of the employed temperature regime is comparatively close to the melting point. Although we witness in subsection 3.2.1 that the Debye-Grüneisen model is suited to accurately describe the thermal expansion of the solid, the phonon densities of states calculated and measured in reference [108] may serve as allowedly weak evidence that, by using these lattice constants in both our LDA and GGA calculations, we do not only underestimate the phonon eigenfrequencies, but simultaneously overestimate the attenuation thereof. A continuing analysis of this conjecture is definitely in order, but collapses as we lack detailed, publicly available data on the temperature dependence of the phonon modes in aluminum.

It may, however, be demonstrated that the overestimation of the resistivity is a general trend of the employed GGA pseudopotential, and thus not solely caused by our proposed method. To do so, we show in figure 3.17 the temperature-dependent resistivity as calculated using the Ziman formula, i.e., in lowest-order variational approximation to the Boltzmann transport equation. The fact that our result is significantly larger than the directly comparable values of Savrasov and Savrasov [10] nicely fortifies the claim that the utilized pseudopotential induces at least a portion of the error. Further, given our previous discussion, the assumption that this is most probably due to a misdescription of the phonon structure could in principle be studied by manually setting the phonon frequencies to their respective value at

[9] During the analogous discussion in case of copper we studied the transmission T_{LR} instead of T_{LR}^{eff} due to the reasoning that their energy dependence is rather similar. Although this assumption should still be valid, this time the effective transmission is considered in order to make sure we do not rely on marginal approximations. Nevertheless, to reduce the number of costly self-energy evaluations, its values are calculated in 10 mRy steps symmetric to the Fermi energy, thus having a slightly increased sampling at the maximum of the Δf function (see figure 3.16). For lack of a more reasonable interpolation scheme, the electron linewidth is subsequently linearly interpolated to calculate T_{LR}^{eff} on a 2.2 mRy mesh.

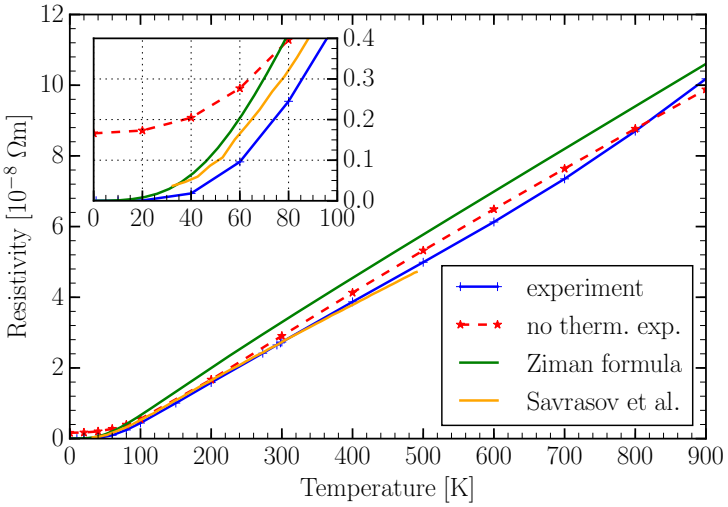

Figure 3.17.: Temperature-dependent resistivity of aluminum calculated employing the Fermi surface triangulation based on the 40^3 mesh while neglecting thermal expansion ("no therm. exp.") as well as GGA pseudopotential evaluation of the "Ziman formula" in comparison to "experiment" [99] and the LOVA result of "Savrasov et al." [10]. The GGA pseudopotential generally overestimates the result. All calculated results fail to reproduce the increasing slope at high temperatures.

100 K, as these frequencies coincide rather well with the experimental data at 300 K (see figure 3.13). This is yet to be done.

Having calculated the resistivity with the employed GGA pseudopotential by exclusively using Quantum ESPRESSO and EPW, it is of course tempting to utilize this calculation as a benchmark for the proposed method as implemented in the Gießen KKR code. This is, in fact, interesting and worthwhile if one keeps in mind that the first method is embedded in the semi-classical Boltzmann formalism, while the latter is a fully quantum-mechanical non-equilibrium Green's function formalism. Quantitative differences should therefore be used as "guesstimates" at the most, if at all.

This being said, in comparison to the previously explained results obtained in the Boltzmann formalism we further show in figure 3.17 the temperature-dependent resistivity of aluminum calculated in the Gießen KKR code employing the Fermi surface triangulation based on the 40^3 mesh while neglecting thermal expansion, i.e., the lattice constant is kept fixed to its value at 300 K. This choice is founded in the consideration that the Ziman formula does not incorporate the effects of thermal expansion, and hence the general trend of both curves is quite similar. In particular, the increasing slope of the experimental data for temperatures above 600 K is not accurately reflected by any of the two calculations, and is therefore most probably an indication for anharmonic effects in the ion-ion interaction.

The Ziman formula does, on the other hand, correctly describe the wave-vector-dependent scattering strengths in the material. The observation that this method nevertheless overestimates the experimental data might be interpreted as evidence that the wave-vector-averaging of the self-energy is potentially not the main cause of error, even though the Fermi surface of aluminum is slightly more complicated than that of copper. Although not conclusive, the relative deviation in the order of 7 % at 900 K could be considered a vague "guesstimate" of the magnitude of error introduced by using purely energy-dependent self-energies in bulk-like resistivity calculations. This should be subject to additional research.

In summary, many of the conclusions drawn in the case of copper can be confirmed. First, it is yet again possible to restrict any transmission calculations to the Fermi energy even at very high temperatures. Consistent with our previous findings, accurate Fermi surface triangulations prove to be superior in the low-temperature regime, but not above room temperature. Additionally, Ohm's law is valid with comparable lower length bounds, as the scattering rates are similar for small temperatures. The presented LDA calculations tend to overestimate both electron linewidth and resistivity, and it is reasonable – though not certain – that the underestimation of the phonon modes is the main cause. Both discussed LDA and GGA calculations yield deviations increasing with temperature, which might indicate that imposing thermal expansion is, unlike copper, not sufficient to correctly treat phonon anharmonicities near the melting point. However, we cannot eliminate the possibility that the wave-vector-averaging of the self-energy is responsible for a significant part of the error.

3.3. Temperature Characteristics of Fe/MgO Double Barrier Structures

So far, the consideration of noncoherent transport processes in the study of Fe/MgO tunnel junctions has been limited to some special scattering mechanism, e.g., to ad hoc level broadening models for disorder [7], to alloy scattering in the metallic electrodes [9], and to the effects of oxygen vacancies in the insulating barriers [109]. In particular, the impact of the temperature-induced electron-phonon interaction on the resonant behavior of the electronic transport in Fe/MgO double barrier structures still lacks a reliable theoretical description. In order to shed some light onto this rather complex phenomenon, we will in the following examine the validity of our proposed method in this context. Due to the high level of intricacy, many additional approximations are made to ensure the feasibility of the calculations. We are, however, confident that the quality of the description is sufficiently high to yield valuable insights and starting points for consecutive in-depth studies.

Given that magnetic tunnel junctions are far more elaborate than the previously considered bulk-like material systems, we start by summarizing relevant physical properties of the Fe/MgO interface and the corresponding single barrier structure. Subsequently, the resonant tunneling mechanism in a Fe/MgO double barrier is

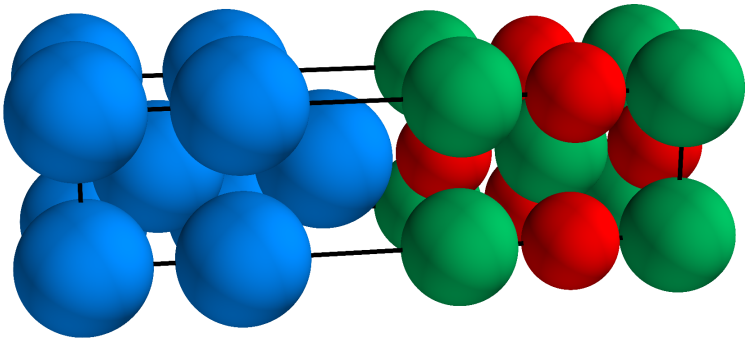

Figure 3.18.: Schematic of the Fe/MgO interface as found in both the single and double barrier structures considered in this work. Details regarding the distances of the various species are given in the text. Fe: blue, Mg: green, O: red.

investigated in some detail. After explaining the necessary approximations to the electron-phonon self-energy, the section is finalized by studying the effects of elevated temperatures on the electronic transmission and the current-voltage characteristics of the device.

3.3.1. Fe/MgO Interface and Single Barrier Structure

It was pointed out by several authors that a detailed discussion of the Fe/MgO interface structure is very important, as it tends to have rather drastic effects on the transport properties [6, 110, 111, and references therein]. Thus, the structure employed within this work is depicted in figure 3.18. It is based on single barrier calculations performed by Czerner [112] using a variant of the "ideal structure" proposed by Heiliger et al. [110, 111], i.e., the metal electrodes are assumed to consist of iron in bcc crystal structure, where the lattice constant is taken to coincide with its experimental value of $a_{\mathrm{Fe}} = 2.866\,\text{Å}$. The [100] direction in Fe is aligned with the MgO [110] direction, and the in-plane lattice constant of MgO is hence taken to be $\sqrt{2}a_{\mathrm{Fe}}$. Out-of-plane, the experimental value of $a_{\mathrm{MgO}} = 4.212\,\text{Å}$ is retained. In order to account for relaxation effects [113], the distance between the two Fe layers adjacent to the interface is increased to 1.69 Å, and the Fe-O distance is assumed to be 2.35 Å. Further in accordance to this very reference [113], the distance between the two MgO layers abutting the Fe/MgO interface is slightly expanded to 2.15 Å.

We begin by considering Cu(10)/Fe(20)/MgO(6)/Fe(20)/Cu(10) to exemplify the behavior of a single barrier magnetic tunnel junction (MTJ). Here, the numbers in round brackets denote the corresponding layer counts. Please note, that the Cu(10) boundary does in fact *not* consist of copper, but of Cu atoms in bcc structure with the experimental lattice constant a_{Fe} of iron. From a physical point, these layers could in principle be though of as a means to model the intricate substrate stacks used in experimental growth processes. More to the point, FeCo alloys instead of

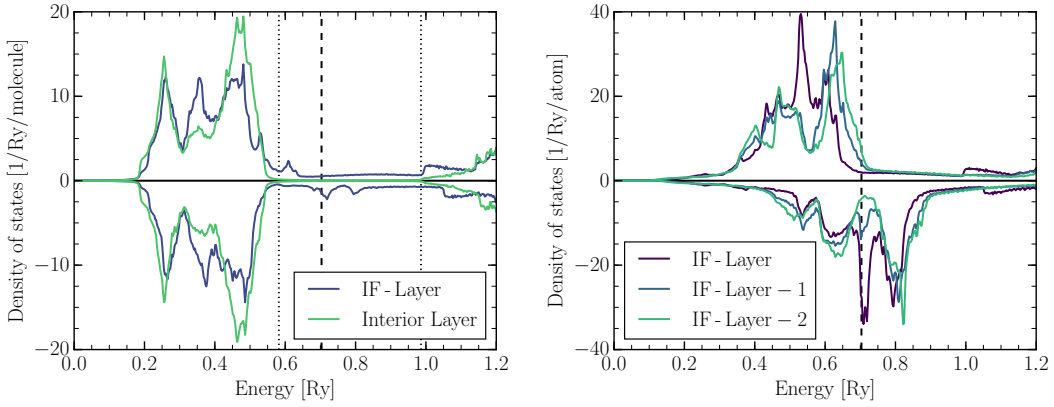

Figure 3.19.: Left: Layer and spin-resolved (majority: positive sign, minority: negative sign) density of states of MgO in the vicinity of the Fe/MgO interface (IF-Layer) and in the center of the barrier (Interior Layer). The Fermi energy of the system is displayed as a dashed line and seen to be located slightly below the center of the MgO band gap (dotted lines). Right: Layer and spin-resolved density of states of iron in the vicinity of the interface. Please note the surface state in the minority spin channel, which is rapidly decaying in space.

pure iron are used in realistic tunnel junctions, which may be simulated in the Gießen KKR code by means of the coherent potential approximation [9]. Accounting for alloy scattering in the semi-infinite leads employed in transport calculations is, however, not implemented, and hence a pseudo-material yielding all necessary electronic states is used [112]. The artificial copper layers are therefore solely kept to facilitate any generalizations of this study to the more realistic case.

The self-consistent effective one-particle potentials $V_{\text{eff}}^{\{\underline{R}\}}(\underline{r})$ are obtained by using a cut-off of $l_{\max} = 3$ in the angular momentum expansions of the Green's functions. After having solved the algebraic Dyson's equation for the Green's function of the constant 8 Ry reference potential on real space clusters of 27 to 68 adjacent atomic sites, the Green's function of the physical system is evaluated in reciprocal space using $24 \times 24 \times 1$ supporting $\underline{k}$ points in the subsequent Brillouin zone integration. The choice of restricting k_z to zero is motivated by the fact that the length of the device in z-direction is rather long, because this is the transport direction by construction. As known from previous studies [9, 112, 114] it is sufficient to treat the exchange-correlation energy E_{xc} in the parameterization of Vosko, Wilk, and Nusair [115] to the local-density approximation.

To demonstrate that these convergence parameters lead to reliable effective potentials, the densities of states of Fe and MgO in the vicinity of the interface and (for the latter) deep in the barrier region are displayed in figure 3.19. As expected from the use of an LDA exchange-correlation functional, we find the MgO band gap of 5.5 eV to be severely underestimated in comparison to its experimental value of

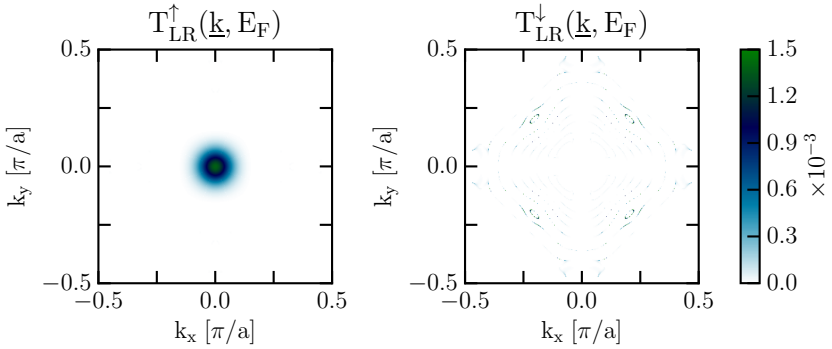

Figure 3.20.: Contour plot of the $\underline{k}$-resolved transmission of the considered Fe/MgO single barrier at the Fermi energy E_F for the majority (↑, left) and minority spin channel (↓, right). While the transmission in the spin up channel is of Δ_1 symmetry and hence confined to $\bar{\Gamma}$, there are several sharp peaks in the spin down channel.

7.8 eV, but to coincide with the value reported by Butler et al. [116]. The use of appropriate "empty spheres"[10] in addition to the atoms in the "ideal" structure leads to a gap-centered Fermi energy in the self-consistent calculations, thus making any renormalizing potential shifts unnecessary.

In the minority spin channel of Fe the well known surface state near the Fermi energy is seen to be very localized in space [114, 116]. According to Rungger, Mryasov, and Sanvito [7], this feature leads to a sharp transmission resonance in the parallel configuration of comparatively thin MgO junctions. It will be discussed later whether this effect is also observable in the following double barrier calculations. In general, however, we find our results to be quite similar to those presented in reference [116]. We hence conclude that the electronic structure is well described.

In the corresponding transport system, the domains $M_{L/R}$ of the decoupling potentials are chosen to coincide with the decimation block size of 4 layers. Due to the high device length, the imaginary part of the energy is set to 2×10^{-6} Ry, which requires to solve the algebraic Dyson's equation on real space clusters of 259 to 599 sites. As for the subsequent discussion we are not only interested in the total conductance, but in separate wave-vector-resolved transmission values for both spins, the surface Brillouin zone is sampled on 400^2 supporting $\underline{k}$ points.

These spin and wave-vector resolved transmission functions at the Fermi energy E_F for the case of two magnetically parallel aligned Fe electrodes are depicted in figure 3.20. It can be clearly seen that the transmission in the majority (↑) spin channel is firmly localized at the center of the surface Brillouin zone, the so-called $\bar{\Gamma}$ point, while at the same time the transmission in the minority spin (↓) channel is characterized by sharp peaks far away from the zone center. The characteristic that the states contributing to the transport are located in different $\underline{k}$ regions leads to a

[10] Auxiliary muffin-tin spheres (2.32) containing vacuum potentials to improve the space filling.

strong suppression of the transmission probability in the antiparallel alignment of the electrodes and hence to a high TMR ratio [9].

The behavior in both spin channels is widely known and explained by two fundamentally different mechanisms: The electronic transport through the MgO barriers is dominated by states of Δ_1 symmetry, because these decay the most slowly as can be deduced from complex band structure calculations [116]. Given that in Fe at the Fermi energy such Δ_1 states are present only in the majority spin channel [9], the transmission in the minority spin channel must be due to another effect. According to Butler et al. [116], the sharp peaks stem from the coupling of the minority surface states in the parallel configuration.

In summary, the presented results are in very good agreement with the characteristic properties of Fe/MgO single barrier structures as known from literature. We may therefore conclude that the electronic structure is sufficiently well described to base the following examinations of double barrier magnetic tunnel junctions upon these preliminary considerations.

3.3.2. Resonant Tunneling in Fe/MgO Double Barriers

The system of choice for the introductory study of Fe/MgO double barrier structures is Cu(10)/Fe(20)/MgO(6)/Fe(30)/MgO(6)/Fe(20)/Cu(10). After the effective one-particle potentials are obtained using the very same numerical parameters as given above in the case of the corresponding single barrier tunnel junction, the densities of states in the interface and barrier regions are calculated and found to be virtually unchanged[11] in comparison to figure 3.19 except for a constant shift in energy. In particular, the Fermi energy shifts from 0.70 Ry to 0.71 Ry.

Similarly, most convergence parameters of the transport calculations coincide with the values given above. This is also true for the imaginary part of the energy, although the double barrier structure is in fact much longer than the previously discussed device. Footnote 13 will comment on the significance of this choice. Considering, on the other hand, the very fine structure of the transmission in the minority spin channel observed in figure 3.20 as well as the notes in references [7] and [8], great care is taken to ensure a valid Brillouin zone integration. Thus, in the zero temperature transmission calculations presented here, a non-equidistant and automatically refined $\underline{k}$ mesh is used to adaptively sample the surface Brillouin zone with a final precision goal of 5 % to the total integrated transmission.

In figure 3.21, the wave-vector-integrated energy-resolved transmission at 0 K is given. The most striking feature of the transmission function are strong, asymmetric peaks that do not reach unity. Both observations regarding peak shape and height will be extensively discussed later in this subsection. Here we will, however, first focus on the question whether these peaks really are due to resonant tunneling processes

[11] Later in this subsection it is argued that quantum well states should be visible in the *s* components of the densities of states of the central Fe layers. We do not observe this, which is most probably due to a comparatively high smearing in the density calculations as well as the fact that the *s* component is roughly 100 times smaller than the total density of states.

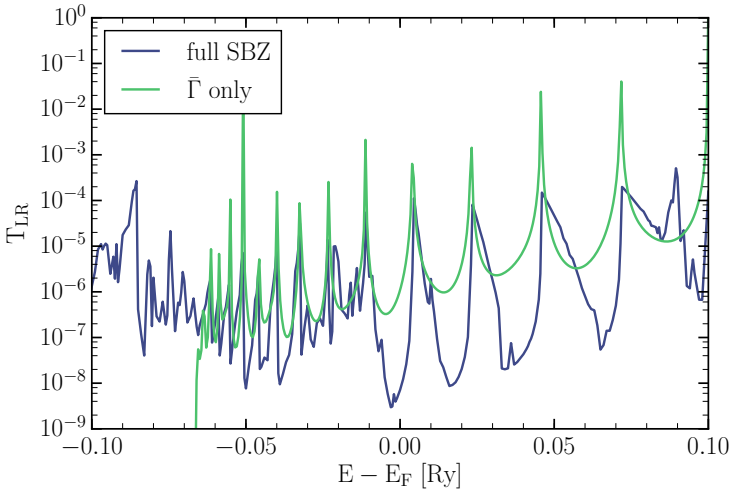

Figure 3.21.: Surface-Brillouin-zone-integrated transmission $T_{LR}(E)$ (labeled "full SBZ") of the considered Fe/MgO double barrier structure as a function of energy in comparison to the transmission value at the zone center (labeled "$\bar{\Gamma}$ only"). Strong peaks are found in both calculations at very similar energy values. In the first case, the peaks prove to be rather asymmetric in energy.

through quantum well states in the Fe intermediate layers as proposed by various authors [6, 34, 85].

Extrapolating the known properties of the eigenenergies of an idealized quantum well to the problem at hand, one would assume that the distance in energy of two "neighboring" eigenstates increases with the main quantum number or, equivalently, with energy. It can be clearly seen in figure 3.21 that this is true for the transmission maxima, especially if the transmission calculations are restricted to its value at $\bar{\Gamma}$. Using the very same reasoning, the eigenenergy differences of two "neighboring" states are assumed to decrease if the quantum well broadens in widths. Analogously to the approach taken in reference [85], this feature has been verified by varying the intermediate Fe layer count.[12] In summary, these results constitute strong evidence that the peaks in the transmission are in fact related to quantum well states formed in the intermediate metal electrode.

Considering that the electronic transport through MgO barriers is dominated by states having Δ_1 symmetry, it is reasonable to assume that these states are responsible for the resonant behavior of the device [6, 85]. To study this further, we depict in figure 3.21 the transmission of the Fe/MgO double barrier at 0 K restricted to the $\bar{\Gamma}$ point and find strong coincidence with the Brillouin-zone-integrated transmission.[13]

[12] Please note that choosing 30 intermediate Fe layers is a result of this test, because the quantum well was designed to be both sufficiently narrow as well as to provide multiple eigenstates in the energy integration window corresponding to bias voltages up to 1 V.

[13] The peculiarity that the peaks in the $\bar{\Gamma}$-restricted calculations do not reach values in the order of

As in figure 3.20 the Δ_1 states where found to be firmly localized at $\bar{\Gamma}$, this assumption is hence corroborated. Given the substantial correlation between wave-vector-resolved local density of states of s-character and $\underline{k}$-resolved transmission as demonstrated by Heiliger, Zahn, and Mertig [117], this approach is believed to be physically very similar to the study of Wang et al. [85]. While they demonstrate both existence and s-character of quantum well states at $\bar{\Gamma}$ in the intermediate Fe layers, we find the coherent transport to be strongly influenced by these states. The latter is, allowedly, to be expected if the first is known.

An even more detailed analysis of figure 3.21 reveals that the peaks of the total transmission $T_{LR}(E)$ and the maxima of the transmission restricted to $\bar{\Gamma}$ do not perfectly coincide: Even if two peaks are related, the one at $\bar{\Gamma}$ seems to occur at slightly lower energies. Further, especially below the Fermi energy, there are additional oscillations in the total transmission. In order to examine both features, we show in figure 3.22 the wave-vector and spin-resolved transmission at selected energy values. Analogous to the case of Fe/MgO single barriers, we find two competing transport mechanisms in the vicinity of the Fermi energy: The transmission in the minority spin channel seems to be determined by resonances on the surface states of the Fe interface layers, which is found by extrapolating the energy-resolved transmission curves given by Rungger, Mryasov, and Sanvito [7] to the case of our double barrier structures. It is exactly those states that introduce the aforementioned additional oscillations. The other peaks in the total transmission do, however, relate to fluctuations in the majority spin channel. In accordance with the previous notion that the peaks are resonances on Δ_1 quantum well states, these fluctuations particularly reside at the surface Brillouin zone center. Now, in order to analyze the assumed shifts in the peak positions as well as the asymmetry of the peaks, the reason for the peak formation must first be studied in greater detail by contrasting the one-dimensional with the three-dimensional case.

In a one-dimensional transport situation, resonant tunneling occurs if the square of the wave number k^2 coincides with the eigenenergy of any quantum well state. In three dimensions, the resonance criterion depends yet again only on the projection of the wave vector $\underline{k}$ onto the transport direction, i.e., k_z^2 must coincide with an eigenenergy of the quantum well. Therefore, contrary to the one-dimensional case, the resonance condition may still be fulfilled if the energy $\underline{k}^2 = k_x^2 + k_y^2 + k_z^2$ of the electron is higher than the eigenstate energy as long as k_x and k_y are chosen in such a way that k_z^2 equals said eigenenergy. Assuming a parabolic dispersion relation, these states would hence form a perfect circle in the surface Brillouin zone, where the radius is a measure for the energy difference to the quantum well eigenenergy. The analog is seen in the contour plots of the majority spin channel in figure 3.22 as a diamond-like pattern veering away from the zone center with increasing energy.

10^0 is most probably owing to the coarse energy-resolution. It might, however, also be a remnant of high imaginary parts of the energy, as test calculations on Cu/Vac double barriers indicate that imaginary parts lower than 2×10^{-9} Ry are necessary for converged transmission values. Given that the peaks will be broadened due to thermal fluctuations for temperatures above 0 K (see subsection 3.3.4), this is not considered an issue within the scope of this work.

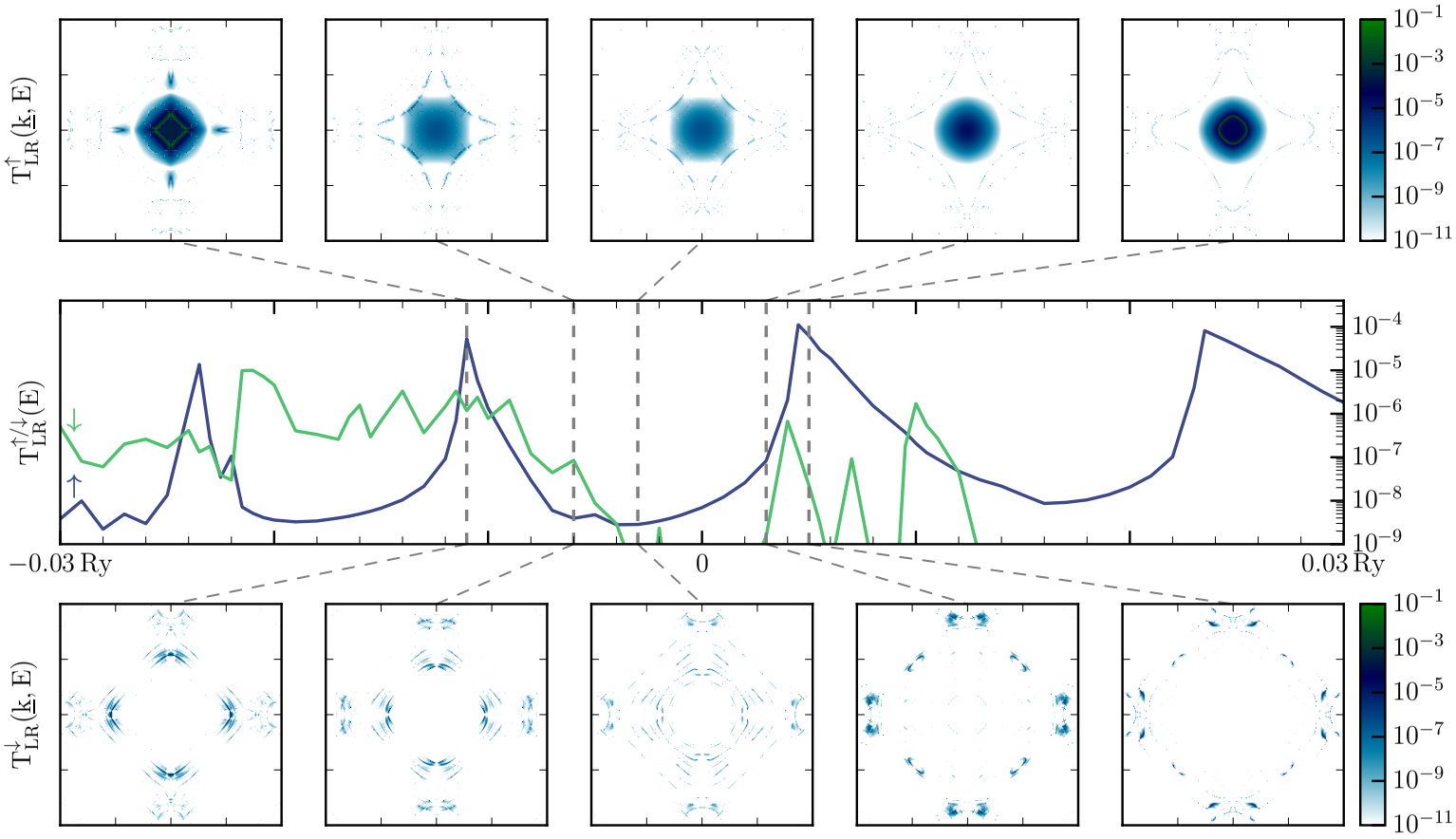

Figure 3.22.: Transmission functions $T_{LR}^{\uparrow/\downarrow}(E)$ of the Fe/MgO double barrier (middle row) near the Fermi energy (set to zero) in comparison to their wave-vector-resolved counterparts $T_{LR}^{\uparrow/\downarrow}(\underline{k}, E)$ at selected energy values (upper and lower row). The resonant peaks in the majority (↑) spin channel due to modulations of the electronic states having Δ_1 symmetry are superposed by additional features stemming from the Fe minority (↓) surface states.

The strong localization of the Δ_1 states near the $\bar{\Gamma}$ point is thus the reason for the suppression of resonances lower in energy, and consequently responsible for the formation of peaks in the first place, because the energy-resolved transmission function would resemble a step function instead of showing oscillatory behavior if these lower-lying resonance states do not vanish.

In summary, the peak shapes and positions as well as their heights in the total transmission are now seen to be due to the surface Brillouin zone integration: As the diamond-like resonance structure moves away from the zone center, there is a critical "radius" at which the integrated transmission is highest (though not unity).[14] For energies above the quantum well eigenenergy the integrated transmission will recede rather slowly, because the Δ_1 states do not vanish abruptly but decay continuously with the distance to the zone center. For electron energies $\underline{k}^2$ below the eigenenergy, however, there are no (k_x, k_y) such that $k_z^2 = \underline{k}^2 - k_x^2 - k_y^2$ is equal to said eigenenergy. Consequently, this results in a sudden rise of the transmission.

Given this thorough discussion of the resonant behavior of Fe/MgO double barrier junctions, we have strong reason to believe that, as suspected by Wang et al. [85], the quantum well resonances may be exploited to generate very high TMR ratios at small bias voltages by suitably choosing the width of the intermediate Fe electrode in such a way that an eigenenergy is very similar to the Fermi energy.[15] Although, as pointed out by Franz, Czerner, and Heiliger [9], a high conductance polarization in the parallel configuration does not necessarily suggest an equally elevated TMR ratio, we find in figure 3.22 the conductance in the minority spin channel to be located in $\underline{k}$ regions far away from the zone center. As this feature was related to the Fe surface states induced by the Fe/MgO interface [116], it should not drastically depend on the width of the potential well. The proposed tuning method is hence assumed to yield the desired result.

In conclusion, we find that convergence parameters similar to the study of Fe/MgO single barrier magnetic tunnel junctions are sufficient for an accurate description of electronic transport properties in the corresponding double barrier structures. The problematic $\underline{k}$-convergence may conveniently be managed by using adaptive sampling techniques. In accordance with the pioneering literature [6, 85], most strong peaks in the energy-resolved transmission are confirmed to relate to resonant tunneling processes involving quantum well states of Δ_1 symmetry in the majority spin channel of the intermediate iron layers, although additional oscillations due to Fe surface states are seen in the vicinity of the Fermi energy. Both existence as well as asymmetry of the resonant transmission peaks are due to the continuous decay of the Δ_1 states in the surface Brillouin zone. The width of the quantum well is believed to be a convenient parameter for the tuning of the TMR ratio.

[14] Although the presented explanation for the claimed minor shift in the peak positions does make sense, we do note for the sake of scientific rigor that there may be other or competing reasons. Additional studies focusing on the effects of the imaginary part of the energy as well as the required energy resolution are necessary if this effect should prove physically relevant.

[15] According to reference [85], the 7th eigenstate in a quantum well consisting of 16 monolayer Fe should have this property.

3.3.3. Electron-phonon Self-energy Approximation

During the studies on the temperature-dependent resistivity in the bulk-like test systems presented in sections 3.1 and 3.2, one of the most important "ingredients" for a valid description of the effects of the electron-phonon scattering proved to be a suitable approximation to the corresponding self-energy. Unfortunately, the situation is found to be even more complicated in the case of Fe/MgO double barrier structures for various reasons.

First, MgO is an insulator and, therefore, does not posses a Fermi surface to average the wave-vector-resolved electron linewidth upon as proposed previously. Consequently, and although there is both experimental [109] and theoretical [118] evidence for the necessity of considering phase-breaking scattering events in the barrier material, we are obliged to assume the tunneling process through the MgO barriers to be free of scattering. Given that the main objective of this study is to examine the effects of the temperature-induced electron-phonon scattering on the resonant behavior and hence on the quantum well states in the Fe intermediate layers, we are confident that the physical picture will not be distorted beyond recognition by applying this approximation.

Still, the restriction of the phase-breaking scattering to the Fe electrodes is not sufficient to retain the proposed method for the evaluation of the electron linewidth, because, as of now, the EPW code is not capable of handling the ferromagnetism displayed by iron. Instead, in order to obtain an approximate value for the electron-phonon self-energy, we propose to fit the temperature-dependent resistivity of Fe bulk to *ab initio* data presented by Verstraete [16] as follows.

As a preliminary, the spin-resolved resistivity $\rho^{\uparrow/\downarrow}$ is calculated employing two arbitrary imaginary parts of the self-energy $\operatorname{Im}\Sigma_{\mathrm{eph}}^{\uparrow/\downarrow}$ spanning (at least parts of) the assumed self-energy range.[16] Further, for every temperature of interest, the corresponding spin-resolved resistivity value extracted from reference [16] is taken as reference value $\rho_{\mathrm{ref}}^{\uparrow/\downarrow}$. The following two steps are then iterated until convergence is achieved: *1)* Based on all previously calculated (self-energy, resistivity) pairs, a functional dependence $\operatorname{Im}\Sigma_{\mathrm{eph}}^{\uparrow/\downarrow}(\rho^{\uparrow/\downarrow})$ is established by means of an appropriate[17] spline interpolation. This function is then used to calculate the required self-energy guess as $\operatorname{Im}\Sigma_{\mathrm{eph}}^{\uparrow/\downarrow}(\rho_{\mathrm{ref}}^{\uparrow/\downarrow})$. *2)* Using this new self-energy guess, the resistivity is calculated and compared to the desired reference value.

It was found in the previous studies that small temperatures or, more precisely, small imaginary parts of the electron-phonon self-energy tend to be problematic with respect to the convergence parameters. Although the calculations in this examination are restricted to temperatures of 100 K and higher, we nevertheless aim for a valid description of the resistivity and hence the electron linewidth for temperatures as low as 20 K to 40 K, because there is wellfounded hope that these values might be

[16] In the actual calculations, we set these two values to 0 Ry and -1×10^{-4} Ry.

[17] First and second order if less than 4 (self-energy, resistivity) pairs are available, cubic spline interpolation otherwise.

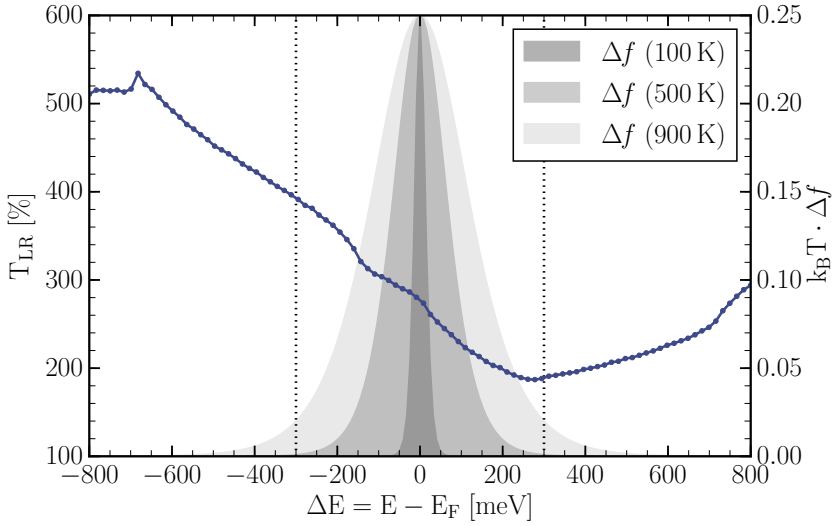

Figure 3.23.: Energy-resolved ballistic transmission T_{LR} [see equation (2.67); dots, line is to guide the eye] of bcc iron as well as Fermi-Dirac difference function Δf [see equation (A.27); shading] at 100 K (dark), 500 K (medium), and 900 K (light). In reasonable approximation, the energy dependence may be assumed linear in the regime $|\Delta E| \leq 300\,\mathrm{meV}$ (indicated by dotted lines), and hence the restriction of the fit to the Fermi energy is considered justifiable.

interesting and useful on its own. Given that these small temperatures correspond to electron linewidths in the order of $1 \times 10^{-5}\,\mathrm{Ry} \approx 0.136\,\mathrm{meV}$, it is necessary to reduce the imaginary part of the energy to $2 \times 10^{-8}\,\mathrm{Ry}$. Then, the algebraic Dyson's equation of the reference system has to be solved using real space clusters of 537 sites. The surface Brillouin zone integration is sufficiently well converged using 100^2 sampling points.

To verify that it is possible to restrict any transmission calculations to the Fermi energy only, in figure 3.23 the energy-resolved coherent part of the transmission $T_{LR}(E)$ is depicted. As discussed in subsection 3.1.5 in the case of copper, the energy dependence of the coherent part should be very similar to that of the effective transmission $T_{LR}^{\mathrm{eff}}(E)$. Therefore, as $T_{LR}(E)$ is in good approximation linear in the energy regime $|\Delta E| \leq 300\,\mathrm{meV}$, the restriction is considered justified for all temperatures up to approximately 900 K.

Given further that the validity of Ohm's law can be demonstrated for device length of at least 56 nm even at the smallest considered temperatures, we may use the resistivity calculation procedure for simple metals employed in the previous studies on aluminum and copper, which, in summary, allows for the iterative calculation of the electron linewidth at the Fermi energy as proposed above. The thusly obtained spin-resolved electron linewidth and resistivity is given in table 3.5.

T [K]	$\lvert\mathrm{Im}\,\Sigma_{\mathrm{eph}}\rvert$ [meV] spin ↓	spin ↑	ρ [$10^{-8} \cdot \Omega\,\mathrm{m}$] spin ↓	spin ↑
20	0.078	0.104	0.104	0.105
40	0.208	0.243	0.263	0.219
60	0.476	0.487	0.571	0.395
80	0.907	1.090	1.039	0.777
100	1.504	2.038	1.668	1.335
200	6.354	7.804	6.738	4.717
300	11.314	13.179	11.945	7.920
400	16.060	18.431	16.918	11.054
500	20.742	23.582	21.798	14.118
600	25.375	28.698	26.595	17.147
700	29.962	33.754	31.305	20.124
800	34.579	38.975	36.003	23.181
900	39.216	44.092	40.671	26.309

Table 3.5.: Spin-resolved absolute value of the imaginary part of the electron-phonon self-energy in iron bulk as well as the corresponding resistivities both as functions of temperature. The electron linewidth is obtained by fitting the resistivities to *ab initio* values reported by Verstraete [16].

Please note that the self-energy obtained in the described way is not to be confused with the "simple" Fock-like self-energy (2.148) used in all previous studies. It is a conglomeration of multiple effects instead – most notably, the thermal expansion is not considered in any electronic structure calculations, and hence all those effects are assumed summarized in this self-energy. Moreover, there are multiple additional issues inherent in the presented approach.

First, the proposed fit procedure of the self-energy only allows to obtain the electron linewidth $\mathrm{Im}\,\Sigma_{\mathrm{eph}}(E_F)$ at the Fermi energy, as all transmission and hence resistivity calculations are restricted to the Fermi energy. In the course of this study we will assume the imaginary part of the self-energy to be constant as a function of energy, although this is known not to be the case [17, 43]. If we extrapolate what is seen in figure 3.16 in the case of aluminum, the "guesstimate" would be a total deviation of approximately 10 % in the considered energy range.

Second, the electronic transmission in iron bulk is nonvanishing in wide areas of the surface Brillouin zone, while, as is demonstrated in the previous subsections, in Fe/MgO double barrier junctions the transmission in the majority spin channel is due to Δ_1 states and hence strongly located at $\bar{\Gamma}$. The transmission in the minority spin channel is driven by the Fe surface states and thus even stronger localized. This suggests that the implicit wave-vector-averaging in the bulk-like case may be a rather bad approximation to the self-energy in Fe/MgO double barriers. The magnitude of the self-energy should, however, be sufficiently well described for the desired qualitative analysis.

Third, as was shown by Hyldgaard et al. [119], the Hartree-like contribution to the self-energy proves to be an important addend at least in the one-dimensional case of resonant tunneling processes. Nevertheless, this contribution is not incorporated in the proposed treatment.

Finally, the real part of the electron-phonon self-energy is not considered. Given that this would only introduce a comparatively small[18] shift of the quantum well states, this is believed not to be an issue in the scope of this work.

In conclusion, similar to what is found in the cases of copper and aluminum, it is considered justified to restrict the transmission and resistivity calculations in iron bulk to the Fermi energy. Ohm's law is valid at slightly higher device lengths than in the previous cases. It hence proves possible to obtain the electron linewidth of iron at the Fermi energy by fitting the temperature-dependent resistivity to *ab initio* data. This quantity is deemed to be a rather coarse approximation to the electron-phonon self-energy if applied in the context of Fe/MgO double barrier junctions, particularly due to both missing energy and wave-vector dependence. The general magnitude is, however, believed to be sufficiently well described to yield a valid description of the effects of temperature given in the next subsection.

3.3.4. Effects of Temperature on the Electronic Transport

In the study of temperature effects, we first consider the general influence of electron-phonon scattering on the electronic transmission, and subsequently expand the analysis to finite bias voltages.

Temperature Dependence of the Transmission

The convergence parameters for the transport calculations at elevated temperatures coincide once again with those presented in subsection 3.3.1. Phase-breaking scattering does, however, introduce an additional broadening of any features in the wave-vector-resolved transmission. Hence, the higher the temperature, the less supporting $\underline{k}$ points are necessary in the surface Brillouin zone integration, which is the reason for restricting the studied temperature range to values of 100 K and higher (besides, of course, the already treated case of absolute zero). More precisely, we use 400^2 $\underline{k}$ points at 100 K, 80^2 samples at 500 K, and only 40^2 supporting points prove sufficient at 900 K.

The energy-resolved transmission at the aforementioned temperatures is given in figure 3.24. The higher the temperature, the more the peaks broaden. This feature has a particularly strong impact at energies in the order of -0.06 Ry with respect to the Fermi energy,[19] as in this region the peaks are especially close to one another. Further, all peaks become more symmetric with increasing temperature. From a phenomenological point of view, both effects are to be expected, as electrons at

[18] The energy difference between the two quantum well states flanking the Fermi energy is approximately 0.25 eV and hence about 10 times higher than typical phonon energies.

[19] Near the bottom of the Δ_1 band in the majority spin channel of Fe [9].

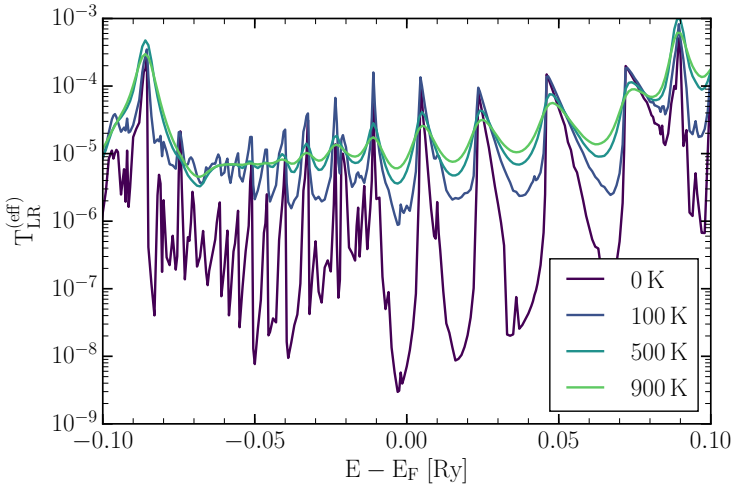

Figure 3.24.: Energy-resolved (effective) transmission T_{LR}^{eff} of the Fe/MgO double barrier at different temperatures. The resonant peaks are "palmed off" with increasing temperature. In regions of very dense peaks they eventually disappear, in higher energy ranges they are only damped.

the quantum well energy may be scattered to higher or lower energies by emitting or absorbing a phonon, and vice versa.[20] The higher the temperature, the more likely such scattering events, and hence the broader the peaks. The asymmetry is lowered because now an electron having a smaller energy than the quantum well state eigenenergy might be scattered to a higher energy by absorbing a phonon; hence, contrary to the case at absolute zero, it may contribute to the resonance. A more detailed analysis less driven by phenomenology is work in progress.

Current-voltage Characteristics

One of the main reasons for the study of double barrier structures is the display of highly nonlinear current-voltage characteristics. In limiting cases, even negative differential resistances $^{\mathrm{d}V}/_{\mathrm{d}I}$ have been reported [34]. To elaborate on this effect, the dependence of the electronic transmission on the bias voltage must obviously be examined first.

Given that, as of now, the Gießen KKR code does not support the self-consistent calculation of the effective one-particle potentials in the presence of nonvanishing external electric fields,[21] the voltage drop in the device has to be modeled by hand.

[20] Please note that the described inelastic scattering processes are not explicitly accounted for by the implementation in the Gießen KKR code. Instead, the electron-phonon self-energy formula (2.138) does average any phonon emission and absorption processes into a quasi-elastic scattering rate by means of an integration over the energy. This approximation is, however, apparently sufficient to accurately mimic the actual physical situation.

[21] The issue is due to the fact that the equilibrium density operator (2.27) is not valid in the interval $\mu_R < E \leq \mu_L$, and consequently the non-equilibrium density operator (2.64) must be evaluated

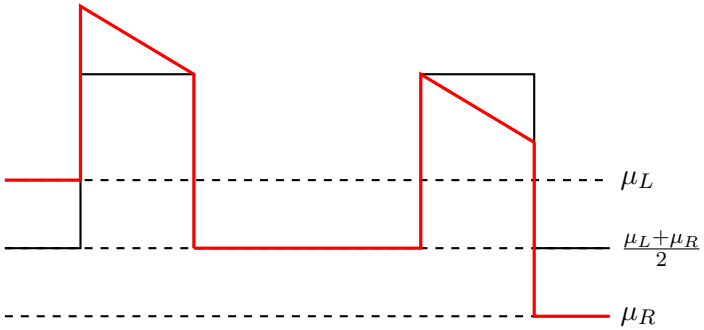

Figure 3.25.: Schematic of the idealized potential curves in the considered Fe/MgO double barrier structures in the case of vanishing external bias voltage (black line) and for finite voltages (red, thick line).

Considering that MgO is an insulator and Fe a metal, it is reasonable to assume that the voltage drop occurs exclusively in the barrier regions because the resistance of iron is basically negligible. Further, ignoring any interface effects and because each MgO layer is structurally equivalent[22], the voltage drop is presumed linear. This idealized potential curve is depicted in figure 3.25. In comparison to self-consistent calculations performed by Rungger, Mryasov, and Sanvito [7], it is seen to be a valid approximation.[23]

Evaluating the voltage dependence of the transmission function is computationally rather expensive, because for each considered bias voltage, a full transmission calculation has to be performed. Especially for small temperatures this is not feasible. Given, however, that the main features are resonant tunneling peaks due to Δ_1 quantum well states, one would expect that the qualitative voltage dependence may be predicted by studying the electronic transmission at $\bar{\Gamma}$ only. To verify this assumption, we show in figure 3.26 the $\bar{\Gamma}$-restricted calculation of the scattering-free case, i.e., $T = 0\,\mathrm{K}$, for various bias voltages up to $1\,\mathrm{V}$ (solid line) in comparison to the total voltage-dependent transmission at $900\,\mathrm{K}$ (dotted line). The latter *does* show some voltage-induced effects that are unrelated to the transmission value at $\bar{\Gamma}$, but in the vicinity of the (quasi-)Fermi energy the behavior remains determined by the Δ_1 states. This confirms that the voltage dependence of the transmission function may be determined by solely studying its value at the zone center. In the following we will use this result to demonstrate that the voltage dependence actually is in good approximation negligible.

in this energy regime. The latter may, however, not be (trivially?) solved on the complex energy contour depicted in figure 2.1, and hence a very dense energy sampling is necessary. Nevertheless, the implementation of this feature is work in progress [120].

[22] The different distances of the boundary layers discussed in subsection 3.3.1 are considered an interface effect.

[23] Actually, a linear voltage drop may not be realized using spherically symmetric potentials. Instead of generalizing to full-potential calculations, the linear voltage drop is further approximated by step functions.

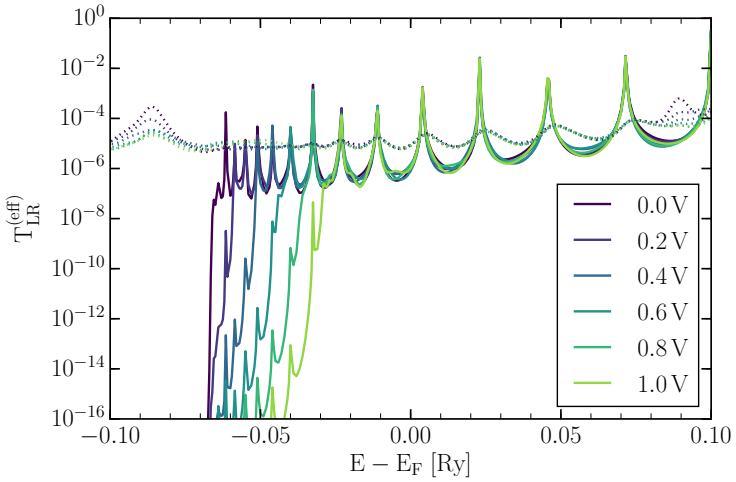

Figure 3.26.: Electronic transmission at $\bar{\Gamma}$ for various bias voltages at 0 K (solid lines) as well as voltage-dependent transmission calculations at 900 K (dotted curves) performed using the full surface Brillouin zone integration. In both cases any changes due to the application of a non-vanishing bias voltage are in good approximation negligible at least in the vicinity of the Fermi energy.

Please note, in a first step, that we consider only positive bias voltages in the following analysis, because in contrast to Nozaki, Tezuka, and Inomata [6], the transmission $T_{LR}(E, V)$ and hence the current $I(V)$ is found to be an even function of the applied bias voltage. This is most probably due to the use of the "ideal" structure, as in this case there is no pollution of the boundary layers with FeO, which was assumed to be responsible for the uneven behavior in this very reference.

In general it is seen in figure 3.26 that (at least at the Fermi energy) neither peak positions nor peak heights are strongly affected by the applied bias voltage. This is explained by considering that the main effect of such an electric field is to shift the electrochemical potentials $\mu_{L/R}$ in the leads as seen in figure 3.25. Further, the barrier potential is affected. If, as in our case of 6 MgO layers, the barrier potential is sufficiently wide and high enough, then the intermediate Fe layers will still form a quantum well of very similar potential. Therefore, the eigenenergies are expected to show no substantial bias voltage dependence, and in conclusion the peaks in the transmission will remain unchanged in good approximation.

The most striking feature seen in figure 3.26 is the strong decrease of the transmission at $\bar{\Gamma}$ in the low energy regime. The energy value at which this drop occurs increases with the bias voltage, and by extrapolating the results of Rungger, Mryasov, and Sanvito [7] to our double barrier setup this is presumed to relate to the edge of the Δ_1 band sweeping through the energy regime due to the applied bias. Because the bottom of the Δ_1 band is roughly 1 eV below E_F [7, 9] the resonance peaks in the vicinity of the Fermi energy will not vanish due to a voltage-driven band

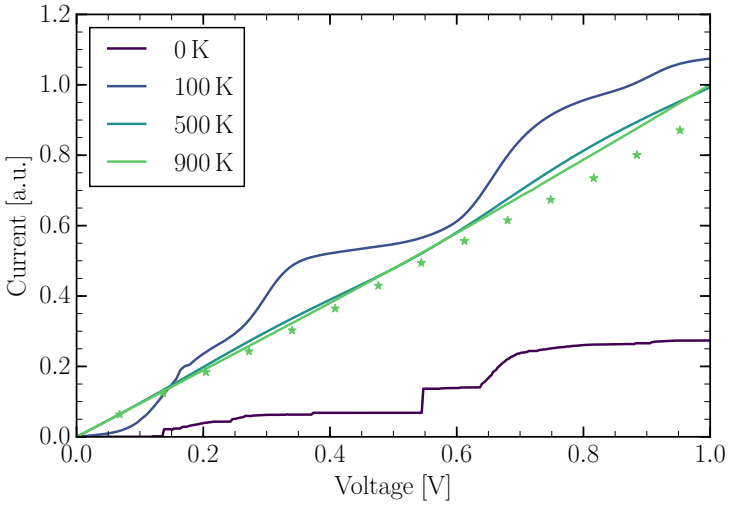

Figure 3.27.: Current-voltage characteristics of the Fe/MgO double barrier at various temperatures neglecting any voltage dependence of the transmission function (solid lines). The higher the temperature, the more the resonant behavior in the current is damped. Negative differential conductivity is absent at any temperature. For comparison, selected current-voltage pairs calculated at 900 K while taking the full voltage dependence of the transmission into account are given as stars.

misalignment in the whole considered bias voltage regime. By the same reasoning, we expect substantial effects for biases of 2 V and higher.

In view of the aforementioned results, and although this seems paradoxical, we will completely neglect any bias voltage dependence of the transmission in the following analysis of the current-voltage characteristics. Given that the resonance on the Fe surface states in the minority spin channel is destroyed by very small bias voltages [7], it is expected that some features in the low bias regime are hence not contained in the results to be presented. This should be an issue only in the low temperature regime, as otherwise these oscillations are completely smeared out due to the additional broadening (see figure 3.24). Nevertheless, a careful review of this approximation should be a guidance for future work.

As mentioned in the introduction, a very interesting feature of double barrier structures is the possibility to exhibit negative differential resistance. This is true in particular for semiconductor-based devices, because in these systems the application of a bias voltage may change the relative alignment of the conduction band and a quantum well eigenstate within this band in such a way that the eigenstate is pushed into the band gap, thereby loosing its capability to contribute to the resonant charge carrier transport [34]. Given, however, that the transmission in Fe/MgO double barriers is dominated by resonances on Δ_1 quantum well states, such behavior is not expected. The reason is that Δ_1 states are present in Fe in the whole energy

interval $E_F \pm 1\,\mathrm{eV}$, and transmission peaks at the Fermi energy may hence not be annihilated by applying bias voltages smaller than 2 V (see above).

For voltages of up to 1 V this expectation is confirmed by figure 3.27. There are strong nonlinearities in the current-voltage characteristics, but the curves remain monotonic, i.e., the higher the voltage, the higher the current. Both is caused by the change in the electrochemical potentials in the electrodes, which leads to an increased energy integration window in equation (2.68): Whenever another peak enters the integration regime, a strong rise in the current is witnessed.

Further, and in accordance with reference [6], we conclude from figure 3.27 that the nonlinear features in the I/V curves are smeared out with increasing temperature. From a theoretical point of view, there are two reasons for this observation: First, the peaks in the transmission curve are palmed off at higher temperatures. Additionally, resonant peaks adjacent to the zero temperature integration window are partially taken into account in the analog of equation (2.68) due to the temperature broadening of the Fermi-Dirac distributions.

To double-check whether the approximation of ignoring any influences of the bias voltage on the transmission is in fact valid at least at higher temperatures, selected (current, voltage) pairs considering the full voltage dependence of the transmission function are calculated at 900 K and displayed in figure 3.27 as stars. Revisiting that there are changes in the transmission far from the Fermi energy, small corrections to the current are to be expected. Indeed, the main result of this approximation seems to be an overestimation of the current in the order of 10 %. For the discussion at hand the presented approach is hence sufficient.

Another observation that seems very curious at first glance is that the inclusion of phase-breaking scattering in the calculations *decreases* the resistance. While there is certainly an increase in the ohmic resistance in the metal electrodes, it is also conceivable that more states having a rather small transmission probability are scattered to states of higher probability than the other way round. Therefore, the electron-phonon coupling could in principle lead to a net increase in the tunneling probability, and hence to a decrease in resistance.

On the other hand, the decrease in the resistance might be introduced by the neglect of scattering in the barrier region: According to reference [109], the scattering on oxygen vacancies in MgO leads to an increase in the resistance. In contrast, Caroli et al. [118] predict a decrease in the resistance due to electron-phonon scattering in the barriers of metal/insulator junctions. Then again, the same reference theoretically finds a decrease in conductance due to scattering in the electrodes, while experimentally an increase is witnessed. Although it hence remains unclear whether the electron-phonon scattering in MgO would (partially) counteract this effect, the observed behavior is still physically sound. Nevertheless, the magnitude of the predicted change as well as the implications of taking scattering in the barriers into account should be subject to further studies.

In conclusion, the resonant peaks in the energy-resolved transmission are broadened due to the temperature-induced electron-phonon scattering. This mechanism also reduces the asymmetry of the peaks, as electrons may now absorb phonons to obtain

the necessary energy for a resonant tunneling process. In the considered Fe/MgO double barrier, the voltage dependence of the transmission is found to be negligible due to two effects: First, the high and wide MgO barrier potentials are only slightly modified by the applied bias, which leads to only minor changes in the quantum well eigenenergies. Second, Δ_1 states are present in Fe in the whole energy interval $E_F \pm 1\,\mathrm{eV}$, and an applied voltage may thus not annihilate any resonant peaks in the vicinity of the Fermi energy. Accordingly, the current-voltage characteristics do not display any negative differential resistance. In agreement with the behavior of the transmission, the nonlinearities in the I/V curves diminish at elevated temperatures. The observation that phase-breaking scattering reduces the resistance of the device might be explained by assuming that the increase in the ohmic resistance of the electrodes is completely reversed by an increase in the net tunneling probability induced by the electron-phonon coupling. Additional studies are necessary to confirm the magnitude of the predicted change. Still, the general trend is in conformance with experimental data [118], and hence considered an additional hint that the proposed method yields significant results regarding the temperature characteristics of Fe/MgO-based double barrier structures.

4. Summary and Outlook

Within this work, a thorough mathematical and physical discussion of the challenges in describing phase-breaking scattering events – in particular those induced by the coupling of electrons and phonons – in *ab initio* electronic transport calculations has been given. The resulting method to do so is characterized by the usage of suitable additional scattering self-energies in the framework of the Keldysh NEGF formalism, and the corresponding implementation of the NEGF part in the Gießen KKR Green's function code was hence generalized to yield all scattering probabilities necessary to calculate the effective transmission. Further, two methods to obtain the required electron-phonon self-energies have been developed: In case of nonmagnetic metals, the implemented *fermint* toolkit may be used to wave-vector-integrate any bulk self-energies obtained using the third party codes Quantum ESPRESSO and EPW. If, on the other hand, spin-resolved resistivities are known, these were shown to be appropriate reference values for an automated self-energy fitting procedure. In conjunction, this approach gives very accurate results when applied to both complex nanostructures as well as devices of macroscopic length scales.

In order to verify the correctness of the implementation and the physical validity of all the necessary approximations, the bulk-like test systems copper (see section 3.1), aluminum (see section 3.2), and, to some extent, iron (see subsection 3.3.3) have been studied. For all three materials it was found that the Landauer formula, i.e., the restriction of the transmission calculation to the Fermi energy E_F, is a sufficiently well approximation to evaluate the temperature-dependent resistivity for temperatures as high as 900 K.

Even though the proposed method is based on the principles of quantum mechanics, it nevertheless displays the experimentally well confirmed linear dependence of the resistance on the device length for very long systems. The necessary length scale of 40 nm and above for the validity of Ohm's law is consistent for all three materials, although slightly higher values are required in the case of iron.

The study of the thermal expansion was restricted to copper and aluminum. It was found that this effect significantly influences the electric conductivity of these metals especially for temperatures above room temperature. The main contribution was traced back to the volume dependence of the phonon dispersion, i.e., the quasi-harmonic approximation proves to be valid. Further, the Debye-Grüneisen theory used to fit the true coefficient of thermal expansion is found to be very accurate in these simple metallic systems.

In the low temperature regime, an accurate sampling of the Fermi surface is far more important for a valid evaluation of the electron-phonon self-energy than any effects due to thermal expansion. Given that in this sentence "accurate" is meant

in the sense of small deviations of the equi-energy surface vertex energies to the reference energy rather than density of these vertices, the necessary computational effort is believed to significantly reduce by using a suitable higher-order interpolation scheme. Additionally, it is of essential importance that any smearing accounting for numerical inaccuracies is much smaller than the corresponding level broadening induced by the thermal fluctuations.

Especially during the study of aluminum it was found that the GGA pseudopotential yields better resistivities than the local-density approximation. This was yet again traced back to an improved description of the phonon dispersion. Considering the rather consistent trend that LDA underestimates the phonon frequencies when used in conjunction with experimental lattice constants, a generalized-gradient approximation seems generally more suited for these kinds of calculations. In any case, great care must be taken to ensure a valid description of the vibrational degrees of freedom in order to obtain proper results.

As a prerequisite to study the applicability of the proposed method in the context of complex nanostructures, the understanding of the quantum-mechanical phenomenon of resonant tunneling in Fe/MgO double barrier junctions was first confirmed and improved. The strong localization of the Δ_1 quantum well states at $\bar{\Gamma}$ was found to mimic the one-dimensional situation, thus leading to the formation of asymmetric peaks in the energy-resolved transmission. Given the presence of Δ_1 states in all of the range $E_F \pm 1\,\mathrm{eV}$, small bias voltages were unable to destroy resonant peaks. Negative differential resistance was hence neither expected nor observed.

Based thereupon, the temperature dependence of the resonant tunneling through Fe/MgO double barrier structures was confirmed to be well described. As expected from a phenomenological point of view, the resonant peaks in the energy-resolved transmission are smeared out and symmetrized with increasing temperature. Consistently, and in conformance with experimental data, the resonant behavior of the current-voltage characteristics was reduced likewise. The latter is, however, both due to the increased electron-phonon scattering as well as the Fermi-Dirac broadening of the energy integration window. Finally, taking phase-breaking scattering in the metallic leads into account led to a decrease of the resistance of the device. This trend is also backed by experimental evidence.

In view of these results, the proposed method is hence found to be valid both for macroscopic and microscopic devices. In the first case it is particularly noteworthy, that the resistivities of copper reported within this work are in better agreement with experimental data than those obtained in the LOVA to the Boltzmann formalism. This is remarkable insofar as the latter is to be considered the *de facto* standard for DFT-based resistivity calculations in metallic systems. Our values also prove superior to other KKR-driven calculations employing the alloy analogy. The significance of the presented microscopic results may be appreciated by noting that we were not only able to confirm the validity of the proposed method, but simultaneously to contribute first theoretical insights regarding the as of yet barely studied effects of temperature on the resonant behavior of Fe/MgO double barrier structures. They hence provide the foundations for many interesting in-depth studies.

It is exactly those studies that should be a guidance for the most pressing future work. In particular, analyzing both voltage and temperature dependence of the TMR and TMS ratio in Fe/MgO double barrier structures is to be considered the next step: On the one hand these quantities are of great interest as was motivated in the introduction, on the other hand the calculations presented in this work already comprise half of the necessary computational cost, i.e., the transmission calculations simply have to be repeated imposing antiparallel aligned magnetic moments in the ferromagnetic leads. This is hence work in progress.

Another interesting project will be to confirm the assumption that the TMR ratio of an Fe/MgO double barrier may in fact be tuned by varying the quantum well thickness in such a way that either a resonant peak or a valley is located at the Fermi energy. While in the first case a negative dependence of the TMR ratio on the temperature is expected, the opposite should happen otherwise. Both assumptions are of course based on the presented result that the resonance peaks are palmed out with increasing temperature. Considering further that at 500 K the nonlinear behavior in the current-voltage characteristics has virtually vanished (see figure 3.27), the low-temperature regime should be studied in more detail.

A. Theoretical Supplementary

A.1. Sum Rule for the Spherical Bessel Function

In the common literature on the theory of the KKR formalism[22, 53], the sum rule (2.42) is proved for real energies E only, as the derivation relies on the so-called Bauer's identity [22]

$$\mathrm{e}^{i\underline{k}\cdot\underline{r}} = 4\pi \sum_L i^l j_L(\underline{r}, E)^{\times} Y_L(\hat{k}), \tag{A.1}$$

where $k^2 \equiv E, k \equiv \|\underline{k}\|$, and $\hat{k} \equiv \underline{k}/k$. These three definitions explicitly rule out complex energy arguments z, and the generalization to arbitrary complex wave vectors $\underline{k}$ seems problematic as in this case $Y_L(\hat{k})$ is undefined. It is, however, possible and sufficient to retain this identity for vectors of the kind

$$\underline{k} = \sqrt{z} \cdot \hat{k} \equiv \sqrt{z} \cdot \begin{pmatrix} \sin\theta_k \cos\phi_k \\ \sin\theta_k \sin\phi_k \\ \cos\theta_k \end{pmatrix}, \quad z \in \mathbb{C},\ \theta_k \in [0, \pi],\ \phi_k \in [0, 2\pi). \tag{A.2}$$

To prove that this is in fact possible, we rewrite

$$\mathrm{e}^{i\underline{k}\cdot\underline{r}} = \mathrm{e}^{i\sqrt{z}r\hat{k}\cdot\hat{r}} = \mathrm{e}^{i\sqrt{z}r\cos\omega} \tag{A.3}$$

where $r = \|\underline{r}\|$, $\underline{r} = r \cdot \hat{r}$ and $\cos\omega \equiv \hat{k} \cdot \hat{r} = \cos\theta_k \cos\theta_r + \sin\theta_k \sin\theta_r \cos(\phi_k - \phi_r)$ denotes the cosine of the angle between the two real-valued unit vectors. Using equation 10.1.47 of reference [121, p. 440], i.e.,

$$\mathrm{e}^{i\sqrt{z}r\cos\omega} = \sum_{l=0}^{\infty} (2l+1) \mathrm{e}^{1/2 l\pi i} j_l(\sqrt{z}r) P_l(\cos\omega), \tag{A.4}$$

in combination with the expansion of the Legendre polynomials

$$P_l(\cos\omega) = \frac{4\pi}{2l+1} \sum_{m=-l}^{l} Y_{lm}(\theta_k, \phi_k) Y_{lm}^*(\theta_r, \phi_r) \tag{A.5}$$

(see [122, p. 63]) yields the claimed relation

$$\mathrm{e}^{i\sqrt{z}r\hat{k}\cdot\hat{r}} = 4\pi \sum_L i^l j_l(\sqrt{z}r) Y_L^*(\hat{r}) Y_L(\hat{k}) \tag{A.6}$$

for arbitrary $z, r \in \mathbb{C}$ and real-valued unit vectors $\hat{k}$ and $\hat{r}$. Please note that – because of the symmetry of the scalar product – it is possible to interchange $\hat{k}$ and $\hat{r}$ in the spherical harmonics.

The proof of the sum rule now proceeds in the usual manner: Starting from the addition theorem for the exponential function

$$\mathrm{e}^{i\sqrt{z}\|\underline{r}-\underline{r}'\|\widehat{\hat{k}\cdot r-r'}} = \mathrm{e}^{i\sqrt{z}r\hat{k}\cdot\hat{r}}\mathrm{e}^{i(-\sqrt{z}r')\hat{k}\cdot\hat{r}'} \tag{A.7}$$

and inserting the derived expansion gives

$$\sum_{L'} i^{l'} j_{L'}(\underline{r}-\underline{r}',z)Y_{L'}^*(\hat{k}) = 4\pi \sum_{L'L''} i^{l'-l''} j_{L'}(\underline{r},z)j_{L''}(\underline{r}',z)^{\times}Y_{L'}^*(\hat{k})Y_{L''}(\hat{k}), \tag{A.8}$$

where we have made use of the fact that $j_l(-\sqrt{z}r') = i^{2l}j_l(\sqrt{z}r')$ (see [121, p. 439]). As the last equation is valid for *any* real-valued unit vector $\hat{k}$, we may multiply with $\int \mathrm{d}\hat{k}\; Y_L(\hat{k})$ from the left and obtain the desired sum rule (2.42) because of the orthonormality of the complex spherical harmonics.

A.2. Lippmann-Schwinger Equation for Self-Energies

In order to prove the Lippmann-Schwinger equation for (a specific kind of) self-energies we will make the following assumptions:

1. The possibly energy-dependent Hamiltonian $\mathcal{H}(z)$ of the "new" system may be written as the sum of a "reference" Hamiltonian $\mathring{\mathcal{H}}$ and a "potential difference" $\Delta\mathcal{V}(z)$, i.e.,
$$\mathcal{H}(z) = \mathring{\mathcal{H}} + \Delta\mathcal{V}(z). \tag{A.9}$$

2. For the given energy z exists an eigenstate of the reference system, i.e.,[1]
$$\ker\left(z\mathbb{1} - \mathring{\mathcal{H}}\right) \neq \varnothing. \tag{A.10}$$

3. The "potential difference" $\Delta\mathcal{V} \equiv \mathcal{V} - \mathring{\mathcal{V}}$ is the difference of two physically sound "potentials". In particular
   - the possibly complex-valued and energy-dependent "potentials" $V(\underline{r},z)$ and $\mathring{V}(\underline{r},z)$ are continuous within the muffin-tin sphere V_{MT}, i.e.,
   $$V(\bullet,z), \mathring{V}(\bullet,z) \in \mathcal{C}^0\big(V_{\mathrm{MT}},\mathbb{C}\big). \tag{A.11}$$
   - both "potentials" are bounded above, i.e.,
   $$\exists B<\infty: \quad \forall \underline{r}\in V_{\mathrm{MT}}: \quad \big|V(\underline{r},z)\big|, \big|\mathring{V}(\underline{r},z)\big| < B. \tag{A.12}$$

[1] $\ker f$ denotes the kernel of the operator $f: X \to Y$, i.e., the set $\{v \in X \mid f(v) = o\}$, o being the zero vector in Y.

In case of assumption 1, the existence of an eigenstate $|\psi(z)\rangle$ to $\mathcal{H}(z)$ is equivalent to

$$\exists\,|\psi(z)\rangle: \quad \left(z\mathbb{1}-\mathring{\mathcal{H}}\right)|\psi(z)\rangle = \Delta\mathcal{V}(z)\,|\psi(z)\rangle\,. \tag{A.13}$$

It is now necessary to distinguish two cases:

Case I: $|\psi(z)\rangle \in \ker\left(z\mathbb{1}-\mathring{\mathcal{H}}\right)$.
Then, statement (A.13) transforms to

$$\exists\,|\psi(z)\rangle: \quad 0 = \Delta\mathcal{V}(z)\,|\psi(z)\rangle\,, \tag{A.14}$$

which, when projected to real space, reads

$$\exists\,|\psi(z)\rangle: \quad \forall\underline{r}\in V_{\mathrm{MT}}: \quad 0 = \Delta V(\underline{r},z)\psi(\underline{r},z). \tag{A.15}$$

Whenever $\psi(\underline{r},z)$ does not vanish, obviously $\Delta V(\underline{r},z)$ has to. Because of assumption 3 both "potentials" are bounded above, and therefore $\psi(\underline{r},z)$ has isolated roots. Using again assumption 3, but this time the continuity of the "potentials", we conclude that $\Delta\mathcal{V}(z)=0$. This pathologic case is not considered to be of interest.

Case II: $|\psi(z)\rangle \notin \ker\left(z\mathbb{1}-\mathring{\mathcal{H}}\right)$.
Then $\left(z\mathbb{1}-\mathring{\mathcal{H}}\right)$ has an invertible restriction in the vicinity of $|\psi(z)\rangle$. This is especially true if the Green's function $\mathring{\mathcal{G}}(z)\equiv\left(z\mathbb{1}-\mathring{\mathcal{H}}\right)^{-1}$ exists. Hence, statement (A.13) is equivalent to

$$\exists\,|\psi(z)\rangle: \quad |\psi(z)\rangle = |\mathring{\psi}(z)\rangle + \mathring{\mathcal{G}}(z)\Delta\mathcal{V}(z)\,|\psi(z)\rangle\,, \tag{A.16}$$

where $|\mathring{\psi}(z)\rangle \in \ker\left(z\mathbb{1}-\mathring{\mathcal{H}}\right)$ exists because of assumption 2. This concludes the proof of the Lippmann-Schwinger equation.

A.3. Numerical Evaluation of the Transition Operator

Starting from the Lippmann-Schwinger equation (2.48) for the isolated muffin-tin potential and inserting representation (2.40) for the free Green's function yields in the case $\|\underline{r}\|\geq R^n_{\mathrm{MT}}$ [123]

$$\underline{\underline{R}}^n(\underline{r},z) = \underline{\underline{j}}(\underline{r},z) - i\sqrt{z}\underline{\underline{h}}^+(\underline{r},z)\underbrace{\int_{V_{\mathrm{MT}}}\mathrm{d}^3x\;\underline{\underline{j}}(\underline{x},z)^{\times}V^n(\underline{x})\underline{\underline{R}}^n(\underline{x},z)}_{=\underline{\underline{t}}^n(z)} \tag{A.17}$$

With the definition of the spherical Hankel functions (2.36) this relation may be rewritten to

$$\underline{\underline{R}}^n(\underline{r},z) = \left(\underline{\underline{j}}(\underline{r},z)\underbrace{\left[\underline{\underline{t}}^n(z)^{-1}-i\sqrt{z}\mathbb{1}\right]}_{\equiv\underline{\underline{K}}^n(z)^{-1}} + \sqrt{z}\underline{\underline{n}}(\underline{r},z)\right)\cdot\underline{\underline{t}}^n(z) \tag{A.18}$$

where the reactance matrix $\underline{\underline{K}}^n(z)$ was defined [22]. Using this relation for the regular scattering solution in the definition of the logarithmic derivative (2.56) allows for the derivation of [22]

$$K_l^n(z)^{-1} = -\sqrt{z} \cdot \frac{L_l^n(z)\, n_l(\sqrt{z}R_{\mathrm{MT}}^n) - \partial_r\, n_l(\sqrt{z}R_{\mathrm{MT}}^n)}{L_l^n(z)\, j_l(\sqrt{z}R_{\mathrm{MT}}^n) - \partial_r\, j_l(\sqrt{z}R_{\mathrm{MT}}^n)}. \tag{A.19}$$

Finally, the two derivatives of the spherical Bessel and Neumann functions may be equivalently formulated as

$$\partial_r\, x_l(\sqrt{z}R_{\mathrm{MT}}^n) = \frac{l}{R_{\mathrm{MT}}^n}\, x_l(\sqrt{z}R_{\mathrm{MT}}^n) - \sqrt{z}\, x_{l+1}(\sqrt{z}R_{\mathrm{MT}}^n), \quad x_l \in \{j_l, n_l\}, \tag{A.20}$$

employing Rayleigh's formulas [53, 121]. Therefore, the components of the transition matrix may be calculated as

$$\begin{aligned} t_l^n(z) &= \left(K_l^n(z)^{-1} + i\sqrt{z}\right)^{-1} \\ &= -\frac{i}{\sqrt{z}} \frac{(L_l^n(z) - {}^{l}/_{R_{\mathrm{MT}}^n})\, j_l(\sqrt{z}R_{\mathrm{MT}}^n) + \sqrt{z}\, j_{l+1}(\sqrt{z}R_{\mathrm{MT}}^n)}{(L_l^n(z) - {}^{l}/_{R_{\mathrm{MT}}^n})\, h_l^+(\sqrt{z}R_{\mathrm{MT}}^n) + \sqrt{z}\, h_{l+1}^+(\sqrt{z}R_{\mathrm{MT}}^n)}. \end{aligned} \tag{A.21}$$

The numerical procedure to obtain the transition matrix is now as follows: First, some initial values of the regular scattering solutions near the origin are extracted from a power series expansion. The remaining unknown values are then integrated with an Adams-Bashforth predictor-corrector scheme. The logarithmic derivatives $L_l^n(z)$ are thus a mere by-product. After evaluating the spherical Bessel and Hankel functions at the muffin-tin radius the transition matrix is given by (A.21).

In case of an additional complex self-energy, the regular scattering solutions

$$\tilde{R}_l^n(r, z) = R_l^n(r, z - \Sigma_{\mathrm{scat}}^n(z)) \tag{A.22}$$

are calculated with the very same numerical integration scheme at the shifted energy $z - \Sigma_{\mathrm{scat}}^n(z)$, giving rise to a different logarithmic derivative $\tilde{L}_l^n(z)$. Otherwise, no adjustment of the beforementioned procedure is necessary. Please note that this approach is only valid under the assumption that each muffin-tin potential may be assigned an explicitly defined *site-diagonal* and *constant* self-energy $\Sigma_{\mathrm{scat}}^n(z)$.

A.4. Resistance in the Limit of Vanishing Bias Voltage

The main steps of the derivation of equation (2.70), being equivalent to what is commonly called "linearized Landauer formalism" [34], have been given in reference [124]. Here, these steps are explained in greater detail: The total transmission

$$T_{LR}^{\mathrm{tot}}(\mu_L, \mu_R, T) \equiv \int_{\mathbb{R}} \mathrm{d}E\; T_{LR}(E, \mu_L, \mu_R, T) \frac{f(E, \mu_L, T) - f(E, \mu_R, T)}{\mu_L - \mu_R} \tag{A.23}$$

contains all the voltage dependence of the resistance (2.69), and hence will mirror its behavior for vanishing bias. Using Lebesgue's theorem of dominated convergence it is possible to interchange integration and limit, and because both μ_L and μ_R will tend to the Fermi energy E_F we find

$$\begin{aligned} T_{LR}^{\mathrm{tot}}(E_F,T) &= \lim_{\Delta\mu\to 0} T_{LR}^{\mathrm{tot}}(\mu_L,\mu_R,T) \\ &= \int_{\mathbb{R}} \mathrm{d}E\; T_{LR}(E,E_F,T) \lim_{\Delta\mu\to 0} \frac{f(E,E_F+\frac{\Delta\mu}{2},T)-f(E,E_F-\frac{\Delta\mu}{2},T)}{\Delta\mu}, \end{aligned} \tag{A.24}$$

where it was further assumed that the transmission function T_{LR} is continuous in the electrochemical potentials. Substituting $\Delta = {}^{\Delta\mu}/_{2}$ and employing l'Hôspital's rule shows that this is equivalent to

$$\int_{\mathbb{R}} \mathrm{d}E\; T_{LR}(E,E_F,T) \lim_{\Delta\to 0} \frac{\partial_\Delta\Big(f(E,E_F+\Delta,T)-f(E,E_F-\Delta,T)\Big)}{2}. \tag{A.25}$$

The derivative of the Fermi-Dirac distribution (2.30) may be evaluated as

$$\begin{aligned} \partial_\Delta f(E,E_F\pm\Delta,T) &= \partial_\Delta \left(\exp\left[\frac{E-E_F\mp\Delta}{k_BT}\right]+1\right)^{-1} \\ &= -\left(\exp\left[\frac{E-E_F\mp\Delta}{k_BT}\right]+1\right)^{-2} \cdot \exp\left[\frac{E-E_F\mp\Delta}{k_BT}\right] \cdot \left(\mp\frac{1}{k_BT}\right) \\ &= \pm\frac{f(E,E_F\pm\Delta,T)^2}{k_BT}\left(f(E,E_F\pm\Delta,T)^{-1}-1\right) \\ &= \pm\frac{f(E,E_F\pm\Delta,T)\left(1-f(E,E_F\pm\Delta,T)\right)}{k_BT}, \end{aligned} \tag{A.26}$$

and therefore the total transmission in the limit of vanishing bias voltage reads

$$T_{LR}^{\mathrm{tot}}(E_F,T) = \int_{\mathbb{R}} \mathrm{d}E\; T_{LR}(E,E_F,T) \underbrace{\frac{f(E,E_F,T)\left(1-f(E,E_F,T)\right)}{k_BT}}_{\equiv \Delta f(E,E_F,T)}. \tag{A.27}$$

Assuming the Taylor series of the transmission function converges, this relation may further be simplified to

$$T_{LR}^{\mathrm{tot}}(E_F,T) = T_{LR}(E_F,T) + \sum_{n=1}^{\infty} \frac{\partial_E^n T_{LR}(E_F,T)}{n!} \cdot \mu_n\left(\Delta f,E_F,T\right), \tag{A.28}$$

and – because Δf is an even function with respect to E_F – all odd moments

$$\mu_n\left(\Delta f,E_F,T\right) \equiv \int_{\mathbb{R}} \mathrm{d}E\; (E-E_F)^n \cdot \Delta f\left(E,E_F,T\right) \tag{A.29}$$

must vanish, i.e., the first correction term to the total transmission is the *second* order change in the transmission at the Fermi energy. Hence, in summary, equation (2.70) is valid in the limit of vanishing bias even for higher temperatures, as long as the "curvature" $\kappa\left(T_{LR}\right)$ is negligible, which is meant in the more general sense as that all (even) higher order derivatives shall be small.

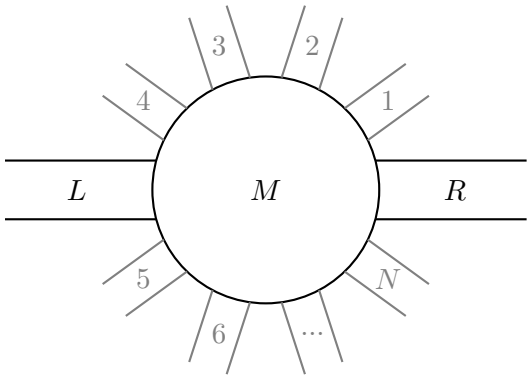

Figure A.1.: Partitioning in the multi-terminal case: The device region M is coupled to two leads L and R and, additionally, N virtual terminals.

A.5. NEGF in a Multiple Terminal Setup

As discussed in section 2.2.2, phase-breaking scattering events in a device are, within this work, modeled through so-called Büttiker probes, i.e., additional (fictitious) voltage probes. It is widely known that the NEGF formalism explained in section 2.2.1 may be expanded to the case of multiple terminals [34, 35]. In this appendix it is demonstrated how this may be achieved considering the case of a device region M connected to two leads L and R as well as N virtual terminals $\alpha \in \mathcal{S}$, for simplicity labeled by Arabic numerals (see figure A.1). Employing once again the partitioning approach [32, 34, 36], it is possible to relate the decoupled system

$$\mathcal{H}_{\mathrm{dc}} = \begin{pmatrix} \mathcal{H}_L & 0 & 0 & \cdots & 0 & 0 \\ 0 & \mathcal{H}_1 & 0 & \cdots & 0 & 0 \\ 0 & 0 & \ddots & \ddots & \vdots & \vdots \\ \vdots & \vdots & \ddots & \mathcal{H}_N & 0 & 0 \\ 0 & 0 & \cdots & 0 & \mathcal{H}_M & 0 \\ 0 & 0 & \cdots & 0 & 0 & \mathcal{H}_R \end{pmatrix}, \quad \tilde{\mathcal{V}}_{\mathrm{c}} = \begin{pmatrix} 0 & 0 & \cdots & 0 & \mathcal{V}_{LM} & 0 \\ 0 & 0 & \cdots & 0 & \mathcal{V}_{1M} & 0 \\ \vdots & \vdots & \ddots & \vdots & \vdots & \vdots \\ 0 & 0 & \cdots & 0 & \mathcal{V}_{NM} & 0 \\ \mathcal{V}_{ML} & \mathcal{V}_{M1} & \cdots & \mathcal{V}_{MN} & 0 & \mathcal{V}_{MR} \\ 0 & 0 & \cdots & 0 & \mathcal{V}_{RM} & 0 \end{pmatrix}, \tag{A.30}$$

to the coupled system $\tilde{\mathcal{H}}_{\mathrm{c}} = \mathcal{H}_{\mathrm{dc}} + \tilde{\mathcal{V}}_{\mathrm{c}}$ via the coupling potentials $\tilde{\mathcal{V}}_{\mathrm{c}}$, where it was assumed that there is no direct coupling between the terminals (regardless whether real or fictitious). Writing, analogous to the case of two terminals (2.60), the relation $\mathbb{1} = (z\mathbb{1} - \tilde{\mathcal{H}}_{\mathrm{c}})\tilde{\mathcal{G}}_{\mathrm{c}}(z)$ in matrix notation, one may extract those $N+3$ subequations containing the Green's function of the coupled middle region $\tilde{\mathcal{G}}_{MM}(z)$

$$0 = (z\mathbb{1} - \mathcal{H}_\alpha)\,\tilde{\mathcal{G}}_{\alpha M}(z) - \mathcal{V}_{\alpha M}\tilde{\mathcal{G}}_{MM}(z), \quad \alpha \in \mathcal{S} \cup \{L, R\}, \tag{A.31a}$$

$$\mathbb{1} = (z\mathbb{1} - \mathcal{H}_M)\,\tilde{\mathcal{G}}_{MM}(z) - \sum_{\alpha \in \mathcal{S}\cup\{L,R\}} \mathcal{V}_{M\alpha}\tilde{\mathcal{G}}_{\alpha M}(z). \tag{A.31b}$$

Solving the first set of equations for $\tilde{\mathcal{G}}_{\alpha M}(z)$ and inserting the results into the last equation yields

$$\mathbb{1} = (z\mathbb{1} - \mathcal{H}_M - \underbrace{(\Sigma_L(z) + \Sigma_R(z))}_{\equiv\Sigma_{\text{leads}}(z)} - \underbrace{\sum\nolimits_{\alpha\in\mathcal{S}} \Sigma_\alpha(z)}_{\equiv\Sigma_{\text{scat}}(z)})\tilde{\mathcal{G}}_{MM}(z), \tag{A.32}$$

where the self-energies

$$\Sigma_\alpha(z) \equiv \mathcal{V}_{M\alpha}\mathcal{G}_\alpha(z)\mathcal{V}_{\alpha M}, \quad \alpha \in \mathcal{S} \cup \{L, R\}, \tag{A.33}$$

have been defined, i.e., the coupling to the device is determined by the Green's function of the isolated subsystems $\mathcal{G}_\alpha(z) \equiv (z\mathbb{1} - \mathcal{H}_\alpha)^{-1}$ as well as the coupling potentials $\mathcal{V}_{M\alpha} = \mathcal{V}_{\alpha M}{}^\dagger$.

This result is equivalent to Dyson's equation

$$\tilde{\mathcal{G}}_{MM}(z) = \mathcal{G}_M(z) + \mathcal{G}_M(z)(\Sigma_{\text{leads}}(z) + \Sigma_{\text{scat}}(z))\tilde{\mathcal{G}}_{MM}(z) \tag{A.34a}$$

$$= \tilde{\mathcal{G}}_M(z) + \tilde{\mathcal{G}}_M(z)\Sigma_{\text{leads}}(z)\tilde{\mathcal{G}}_{MM}(z) \tag{A.34b}$$

with the Green's function of the isolated middle region containing scattering $\tilde{M}$ defined by

$$\tilde{\mathcal{G}}_M(z) = \mathcal{G}_M(z) + \mathcal{G}_M(z)\Sigma_{\text{scat}}(z)\tilde{\mathcal{G}}_M(z). \tag{A.35}$$

This second point of view is favorable if the scattering self-energies are to be calculated by other means and not within the partitioning approach. Please note that this is actually the common case given that the Büttiker probes are a purely hypothetical concept and hence the Green's functions of the isolated probes are not accessible [124]. Details regarding this idea are discussed in sections 2.2.2 and 2.2.3.

A.6. Derivation of Effective Transmission Formulae

In this section a detailed derivation of equation (2.74) taken from reference [35] is given. In fact, the sole purpose is to shed some light on "some algebraic manipulation[s]" mentioned in this very work. Subsequently it is shown how to transform this equation into (2.76) taking the limit of infinite scattering order into account.

The total current (density) per spin degree of freedom from the left to the right terminal is given by equation (2.68), which gives rise to the definition of its energy-resolved counterpart

$$j_{LR}(E) = \frac{q}{h}T_{LR}(E)(f_L(E) - f_R(E)). \tag{A.36}$$

In case of a multiple terminal setup, the total current originating from terminal X is given by the superposition of the currents from this (possibly virtual) terminal to all other (possibly virtual) terminals [34, 35]. Denoting the set of all real terminals with $\mathcal{T}$ and of all Büttiker probes (i.e., virtual terminals) with $\mathcal{S}$, this reads

$$j_X(E) = \sum_{n\in\mathcal{T}} \frac{q}{h}T_{Xn}(E)(f_X(E) - f_n(E)) + \sum_{\alpha\in\mathcal{S}} \frac{q}{h}T_{X\alpha}(E)(f_X(E) - f_\alpha(E)). \tag{A.37}$$

While the leads $\mathcal{T}$ are usually considered to be in thermodynamic equilibrium with an electron reservoir and therefore having Fermi-Dirac distributed charge carriers [35], the distribution functions f_α of the Büttiker probes are per se unknown. For reasons of charge and energy conservation it is further convenient to enforce the sufficient (yet not necessary[2]) condition that the current per energy in the virtual terminals must vanish, i.e., $\forall \alpha \in \mathcal{S}$:

$$\begin{aligned} 0 &= \sum_{n\in\mathcal{T}} T_{\alpha n}(E)(f_\alpha(E) - f_n(E)) + \sum_{\beta\in\mathcal{S}}^{\beta\neq\alpha} T_{\alpha\beta}(E)(f_\alpha(E) - f_\beta(E)) \\ \Leftrightarrow \quad f_\alpha(E) &= \frac{\sum_{n\in\mathcal{T}} T_{\alpha n}(E) f_n(E) + \sum_{\beta\in\mathcal{S}}^{\beta\neq\alpha} T_{\alpha\beta}(E) f_\beta(E)}{S_\alpha(E)} \end{aligned} \tag{A.38}$$

with the denominator

$$S_\alpha(E) \equiv \sum_{n\in\mathcal{T}} T_{\alpha n}(E) + \sum_{\beta\in\mathcal{S}}^{\beta\neq\alpha} T_{\alpha\beta}(E). \tag{A.39}$$

Dropping the energy argument for the sake of readability and using (A.38) iteratively in equation (A.37) yields

$$\begin{aligned} \frac{h}{q} j_X = &\sum_{n\in\mathcal{T}} \underbrace{\left(T_{Xn} + \sum_{\alpha\in\mathcal{S}} \frac{T_{X\alpha}T_{\alpha n}}{S_\alpha} + \sum_{\alpha,\beta\in\mathcal{S}}^{\beta\neq\alpha} \frac{T_{X\alpha}T_{\alpha\beta}T_{\beta n}}{S_\alpha S_\beta} + \dots \right)}_{\equiv T^{\text{eff}}_{Xn}} (f_X - f_n) \\ &+ \underbrace{\sum_{\alpha\in\mathcal{S}} \left(T_{X\alpha} - \sum_{n\in\mathcal{T}} \frac{T_{X\alpha}T_{\alpha n}}{S_\alpha} - \sum_{n\in\mathcal{T}} \sum_{\beta\in\mathcal{S}}^{\beta\neq\alpha} \frac{T_{X\alpha}T_{\alpha\beta}T_{\beta n}}{S_\alpha S_\beta} - \dots \right)}_{\equiv \mathcal{O}_X} f_X \end{aligned} \tag{A.40}$$

The remaining task is to discuss why $\mathcal{O}_X = 0$. This is true because

$$\begin{aligned} \mathcal{O}_X &= \sum_{\alpha\in\mathcal{S}} \frac{T_{X\alpha}}{S_\alpha} \left(S_\alpha - \sum_{n\in\mathcal{T}} \left[T_{\alpha n} + \sum_{\beta\in\mathcal{S}}^{\beta\neq\alpha} \frac{T_{\alpha\beta}T_{\beta n}}{S_\beta} + \dots \right] \right) \\ &= \sum_{\alpha,\beta\in\mathcal{S}}^{\beta\neq\alpha} \frac{T_{X\alpha}T_{\alpha\beta}}{S_\alpha S_\beta} \left(S_\beta - \sum_{n\in\mathcal{T}} \left[T_{\beta n} + \sum_{\gamma\in\mathcal{S}}^{\gamma\neq\beta} \frac{T_{\beta\gamma}T_{\gamma n}}{S_\gamma} + \dots \right] \right), \end{aligned} \tag{A.41}$$

i.e., each scattering order is annihilated by the next higher one. Please note that, even though it seems obvious from a physical point of view, it is rather nontrivial to show both convergence and limit of the series

$$\mathcal{O}_X = \sum_{\alpha,\beta,\gamma,\dots\in\mathcal{S}}^{\beta\neq\alpha,\gamma\neq\beta,\dots} \frac{T_{X\alpha}T_{\alpha\beta}T_{\beta\gamma}\cdots}{S_\alpha S_\beta S_\gamma \cdots} = 0 \tag{A.42}$$

[2] It would be necessary to enforce that the energy-integrated current in each Büttiker probe must vanish, which would also allow for inelastic scattering events. These are, however, not within the scope of this work.

in a mathematically exact manner.

Formula (2.76) is now easy to obtain: With the renormalized transmission

$$\tilde{T}_{\alpha X} \equiv \frac{T_{\alpha X}}{S_\alpha}, \quad \alpha \in \mathcal{S}, \quad X \in \mathcal{T} \cup \mathcal{S}, \tag{A.43}$$

the effective transmission from left to right may be written as

$$T_{LR}^{\text{eff}} = T_{LR} + \sum_{\alpha \in \mathcal{S}} T_{L\alpha} \tilde{T}_{\alpha R} + \sum_{\alpha,\beta \in \mathcal{S}}^{\beta \neq \alpha} T_{L\alpha} \tilde{T}_{\alpha\beta} \tilde{T}_{\beta R} + \ldots \tag{A.44}$$

Defining further $T_{\alpha\alpha} \equiv 0$ for all $\alpha \in \mathcal{S}$, the row vector $\underline{T}_L \equiv \left\{T_{L\alpha}\right\}_{\alpha \in \mathcal{S}}$, as well as the column vector $\underline{\tilde{T}}_R \equiv \left\{\tilde{T}_{\alpha R}\right\}_{\alpha \in \mathcal{S}}^{\mathrm{T}}$ and the matrix $\underline{\underline{\tilde{T}}} \equiv \left\{\tilde{T}_{\alpha\beta}\right\}_{\alpha,\beta \in \mathcal{S}}$, then it is seen that the last equation is equivalent to

$$T_{LR}^{\text{eff}} = T_{LR} + \underline{T}_L \underbrace{\left(\mathbb{1} + \underline{\underline{\tilde{T}}} + \underline{\underline{\tilde{T}}}^2 + \ldots\right)}_{\equiv \underline{\underline{\tilde{T}}}_{\text{inf}}} \underline{\tilde{T}}_R. \tag{A.45}$$

Of course, $\underline{\underline{\tilde{T}}}_{\text{inf}}$ is the limit of a geometric series and therefore

$$\underline{\underline{\tilde{T}}}_{\text{inf}} = \mathbb{1} + \underline{\underline{\tilde{T}}} \cdot \underline{\underline{\tilde{T}}}_{\text{inf}} \quad \Leftrightarrow \quad \underline{\underline{\tilde{T}}}_{\text{inf}} = \left(\mathbb{1} - \underline{\underline{\tilde{T}}}\right)^{-1}, \tag{A.46}$$

which concludes the proof.

Bibliography

[1] G. E. Moore. “Progress In Digital Integrated Electronics”. In: *International Electron Devices Meeting, IEEE* (1975).

[2] G. E. Moore. “Cramming more components onto integrated circuits”. In: *Electronics* 38.8 (1965).

[3] M. Julliere. “Tunneling between ferromagnetic films”. In: *Phys. Lett. A* 54.3 (1975), pp. 225–226. ISSN: 0375-9601. DOI: https://doi.org/10.1016/0375-9601(75)90174-7.

[4] T. Miyazaki and N. Tezuka. “Giant magnetic tunneling effect in Fe/Al2O3/Fe junction”. In: *J. Magn. Magn. Mater.* 139.3 (1995), pp. L231–L234. ISSN: 0304-8853. DOI: https://doi.org/10.1016/0304-8853(95)90001-2.

[5] J. S. Moodera et al. “Large Magnetoresistance at Room Temperature in Ferromagnetic Thin Film Tunnel Junctions”. In: *Phys. Rev. Lett.* 74 (16 Apr. 1995), pp. 3273–3276. DOI: 10.1103/PhysRevLett.74.3273.

[6] T. Nozaki, N. Tezuka, and K. Inomata. “Quantum Oscillation of the Tunneling Conductance in Fully Epitaxial Double Barrier Magnetic Tunnel Junctions”. In: *Phys. Rev. Lett.* 96 (2 Jan. 2006), p. 027208. DOI: 10.1103/PhysRevLett.96.027208.

[7] I. Rungger, O. Mryasov, and S. Sanvito. “Resonant electronic states and $I-V$ curves of Fe/MgO/Fe(100) tunnel junctions”. In: *Phys. Rev. B* 79 (9 Mar. 2009), p. 094414. DOI: 10.1103/PhysRevB.79.094414.

[8] J. Peralta-Ramos et al. “$I-V$ curves of Fe/MgO (001) single- and double-barrier tunnel junctions”. In: *Phys. Rev. B* 78 (2 July 2008), p. 024430. DOI: 10.1103/PhysRevB.78.024430.

[9] C. Franz, M. Czerner, and C. Heiliger. “Influence of the magnetic material on tunneling magnetoresistance and spin-transfer torque in tunnel junctions: Ab initio studies”. In: *Phys. Rev. B* 88 (9 Sept. 2013), p. 094421. DOI: 10.1103/PhysRevB.88.094421.

[10] S. Y. Savrasov and D. Y. Savrasov. “Electron-phonon interactions and related physical properties of metals from linear-response theory”. In: *Phys. Rev. B* 54 (23 Dec. 1996), pp. 16487–16501. DOI: 10.1103/PhysRevB.54.16487.

[11] G. Grimvall. *The electron-phonon interaction in metals*. Selected topics in solid state physics. North-Holland Pub. Co. : sole distributors for the U.S.A. and Canada, Elsevier North-Holland, 1981. ISBN: 9780444861054.

[12] E. Grüneisen. “Theorie des festen Zustandes einatomiger Elemente”. In: *Ann. Phys.* 344.12 (1912), pp. 257–306. ISSN: 1521-3889. DOI: 10.1002/andp.19123441202.

[13] T. Holstein. “Theory of transport phenomena in an electron-phonon gas”. In: *Ann. Phys.* 29.3 (1964), pp. 410–535. ISSN: 0003-4916. DOI: http://dx.doi.org/10.1016/0003-4916(64)90008-9.

[14] H. Ebert et al. “Calculating linear-response functions for finite temperatures on the basis of the alloy analogy model”. In: *Phys. Rev. B* 91 (16 Apr. 2015), p. 165132. DOI: 10.1103/PhysRevB.91.165132.

[15] P. B. Allen et al. “dc transport in metals”. In: *Phys. Rev. B* 34 (6 Sept. 1986), pp. 4331–4333. DOI: 10.1103/PhysRevB.34.4331.

[16] M. J. Verstraete. “Ab initio calculation of spin-dependent electron-phonon coupling in iron and cobalt”. In: *J. Phys.: Condens. Matter* 25.13 (2013), p. 136001. DOI: 10.1088/0953-8984/25/13/136001.

[17] S. Poncé et al. “EPW: Electron–phonon coupling, transport and superconducting properties using maximally localized Wannier functions”. In: *Comput. Phys. Commun.* 209.Supplement C (2016), pp. 116–133. ISSN: 0010-4655. DOI: https://doi.org/10.1016/j.cpc.2016.07.028.

[18] A. P. Jauho. “Quantum electron-phonon transport equations revisited”. In: *J. Phys. F: Met. Phys.* 13.10 (1983), p. L203.

[19] W. Kohn. “Nobel Lecture: Electronic structure of matter – wave functions and density functionals”. In: *Rev. Mod. Phys.* 71 (5 Oct. 1999), pp. 1253–1266. DOI: 10.1103/RevModPhys.71.1253.

[20] S. Baroni et al. “Phonons and related crystal properties from density-functional perturbation theory”. In: *Rev. Mod. Phys.* 73 (2 July 2001), pp. 515–562. DOI: 10.1103/RevModPhys.73.515.

[21] W. Kohn and L. J. Sham. “Self-Consistent Equations Including Exchange and Correlation Effects”. In: *Phys. Rev.* 140 (4A Nov. 1965), A1133–A1138. DOI: 10.1103/PhysRev.140.A1133.

[22] J. Zabloudil et al. *Electron Scattering in Solid Matter*. Vol. 147. Springer Series in Solid-State Sciences. Berlin: Springer, 2005.

[23] W. Kohn and N. Rostoker. “Solution of the Schrödinger Equation in Periodic Lattices with an Application to Metallic Lithium”. In: *Phys. Rev.* 94 (5 June 1954), pp. 1111–1120. DOI: 10.1103/PhysRev.94.1111.

[24] P. Giannozzi et al. “QUANTUM ESPRESSO: a modular and open-source software project for quantum simulations of materials”. In: *J. Phys.: Condens. Matter* 21.39 (2009), 395502 (19pp). DOI: 10.1088/0953-8984/21/39/395502.

[25] X. Gonze et al. “Recent developments in the ABINIT software package”. In: *Comput. Phys. Commun.* 205 (2016), p. 106. ISSN: 0010-4655. DOI: 10.1016/j.cpc.2016.04.003.

[26] G. Kresse and J. Hafner. “Ab initio molecular dynamics for liquid metals”. In: *Phys. Rev. B* 47 (1 Jan. 1993), pp. 558–561. DOI: 10.1103/PhysRevB.47.558.

[27] J. Korringa. “On the calculation of the energy of a Bloch wave in a metal”. In: *Physica* 13.6 (1947), pp. 392–400. ISSN: 0031-8914. DOI: 10.1016/0031-8914(47)90013-X.

[28] P. Hohenberg and W. Kohn. “Inhomogeneous Electron Gas”. In: *Phys. Rev.* 136 (3B Nov. 1964), B864–B871. DOI: 10.1103/PhysRev.136.B864.

[29] Y. Liu et al. “First-principles calculations of magnetization relaxation in pure Fe, Co, and Ni with frozen thermal lattice disorder”. In: *Phys. Rev. B* 84 (1 July 2011), p. 014412. DOI: 10.1103/PhysRevB.84.014412.

[30] D. W. Taylor. “Vibrational Properties of Imperfect Crystals with Large Defect Concentrations”. In: *Phys. Rev.* 156 (3 Apr. 1967), pp. 1017–1029. DOI: 10.1103/PhysRev.156.1017.

[31] P. Soven. “Coherent-Potential Model of Substitutional Disordered Alloys”. In: *Phys. Rev.* 156 (3 Apr. 1967), pp. 809–813. DOI: 10.1103/PhysRev.156.809.

[32] C. Franz, M. Czerner, and C. Heiliger. “Implementation of non-equilibrium vertex corrections in KKR: transport through disordered layers”. In: *J. Phys.: Condens. Matter* 25.42 (2013), p. 425301. DOI: 10.1088/0953-8984/25/42/425301.

[33] M. Büttiker. “Small normal-metal loop coupled to an electron reservoir”. In: *Phys. Rev. B* 32 (3 Aug. 1985), pp. 1846–1849. DOI: 10.1103/PhysRevB.32.1846.

[34] S. Datta. *Electronic Transport in Mesoscopic Systems*. Cambridge Studies in Semiconductor Physics and Microelectronic Engineering. Cambridge University Press, 1995. DOI: 10.1017/CBO9780511805776.

[35] G. Metalidis. “Electronic Transport in Mesoscopic Systems”. PhD thesis. Martin-Luther-Universität Halle-Wittenberg, 2007.

[36] J. Henk et al. “Computing conductances of tunnel junctions by the Korringa–Kohn–Rostoker method: formulation and test of a Green function approach”. In: *J. Phys.: Condens. Matter* 18.8 (2006), pp. 2601–2614. DOI: 10.1088/0953-8984/18/8/021.

[37] M. Brandbyge et al. “Density-functional method for nonequilibrium electron transport”. In: *Phys. Rev. B* 65 (16 Mar. 2002), p. 165401. DOI: 10.1103/PhysRevB.65.165401.

[38] M. M. Dacorogna, M. L. Cohen, and P. K. Lam. “Self-Consistent Calculation of the q Dependence of the Electron-Phonon Coupling in Aluminum”. In: *Phys. Rev. Lett.* 55 (8 Aug. 1985), pp. 837–840. DOI: 10.1103/PhysRevLett.55.837.

[39] P. K. Lam, M. M. Dacorogna, and M. L. Cohen. “Self-consistent calculation of electron-phonon couplings”. In: *Phys. Rev. B* 34 (8 Oct. 1986), pp. 5065–5069. DOI: 10.1103/PhysRevB.34.5065.

[40] A. I. Liechtenstein et al. “Structural phase diagram and electron-phonon interaction in $Ba_{1-x}K_xBiO_3$”. In: *Phys. Rev. B* 44 (10 Sept. 1991), pp. 5388–5391. DOI: 10.1103/PhysRevB.44.5388.

[41] S. Baroni, P. Giannozzi, and A. Testa. “Green’s-function approach to linear response in solids”. In: *Phys. Rev. Lett.* 58 (18 May 1987), pp. 1861–1864. DOI: 10.1103/PhysRevLett.58.1861.

[42] X. Gonze. “Adiabatic density-functional perturbation theory”. In: *Phys. Rev. A* 52 (2 Aug. 1995), pp. 1096–1114. DOI: 10.1103/PhysRevA.52.1096.

[43] F. Giustino, M. L. Cohen, and S. G. Louie. “Electron-phonon interaction using Wannier functions”. In: *Phys. Rev. B* 76 (16 Oct. 2007), p. 165108. DOI: 10.1103/PhysRevB.76.165108.

[44] T. Gunst et al. “First-principles method for electron-phonon coupling and electron mobility: Applications to two-dimensional materials”. In: *Phys. Rev. B* 93 (3 Jan. 2016), p. 035414. DOI: 10.1103/PhysRevB.93.035414.

[45] A. A. Mostofi et al. “An updated version of wannier90: A tool for obtaining maximally-localised Wannier functions”. In: *Comput. Phys. Commun.* 185.8 (2014), pp. 2309–2310. ISSN: 0010-4655. DOI: 10.1016/j.cpc.2014.05.003.

[46] I. Souza, N. Marzari, and D. Vanderbilt. “Maximally localized Wannier functions for entangled energy bands”. In: *Phys. Rev. B* 65 (3 Dec. 2001), p. 035109. DOI: 10.1103/PhysRevB.65.035109.

[47] G. Czycholl. *Theoretische Festkörperphysik: von den klassischen Modellen zu modernen Forschungsthemen*. 3., aktualisierte Auflage. Springer-Lehrbuch. Berlin: Springer, 2008. ISBN: 978-3-540-74790-1. DOI: 10.1007/978-3-540-74790-1.

[48] M. Born and R. Oppenheimer. “Zur Quantentheorie der Molekeln”. In: *Ann. Phys.* 389.20 (1927), pp. 457–484. ISSN: 1521-3889. DOI: 10.1002/andp.19273892002.

[49] R. Heid. “Density Functional Perturbation Theory and Electron Phonon Coupling”. In: *Emergent Phenomena in Correlated Matter*. Ed. by E. Pavarini, E. Koch, and U. Schollwöck. Vol. 3. Modeling and Simulation. Verlag des Forschungszentrum Jülich, 2013. Chap. 12. ISBN: 978-3-89336-884-6.

[50] H. Haug and A.-P. Jauho. *Quantum Kinetics in Transport and Optics of Semiconductors*. Vol. 123. Springer Series in Solid-State Sciences. Berlin: Springer, 2008. DOI: 10.1007/978-3-540-73564-9.

[51] J. Rammer. *Quantum Field Theory of Non-equilibrium States*. Cambridge University Press, 2007. DOI: 10.1017/CBO9780511618956.

[52] W. Walter. *Gewöhnliche Differentialgleichungen: eine Einführung*. 7., neu bearbeitete und erweiterte Auflage. Springer-Lehrbuch. Berlin [u.a.]: Springer, 2000. ISBN: 9783540676423. DOI: 10.1007/978-3-642-97631-5.

[53] I. Mertig, E. Mrosan, and P. Ziesche. *Multiple Scattering Theory of Point Defects in Metals: Electronic Properties*. Leipzig: Teubner, 1987.

[54] W. Nolting. *Grundkurs Theoretische Physik 5/1: Quantenmechanik - Grundlagen*. 8. Auflage. Springer-Lehrbuch. Berlin, Heidelberg: Springer, 2013. ISBN: 3642254039 (Sekundärausgabe). DOI: 10.1007/978-3-642-25403-1.

[55] M. Czerner. "Beiträge zur Theorie des Elektronentransports in Systemen mit nichtkollinearer magnetischer Ordnung". PhD thesis. Naturwissenschaftlichen Fakultät II - Chemie und Physik, Martin-Luther-Universität Halle-Wittenberg, 2009.

[56] E. N. Economou. *Green's Functions in Quantum Physics*. Vol. 7. Springer Series in Solid-State Sciences. Berlin: Springer, 2006. DOI: 10.1007/3-540-28841-4.

[57] K. Wildberger et al. "Fermi-Dirac distribution in ab initio Green's-function calculations". In: *Phys. Rev. B* 52 (15 Oct. 1995), pp. 11502–11508. DOI: 10.1103/PhysRevB.52.11502.

[58] R. Zeller. "Towards a linear-scaling algorithm for electronic structure calculations with the tight-binding Korringa–Kohn–Rostoker Green function method". In: *J. Phys.: Condens. Matter* 20.29 (2008), p. 294215. DOI: 10.1088/0953-8984/20/29/294215.

[59] R. Zeller, J. Deutz, and P. H. Dederichs. "Application of complex energy integration to selfconsistent electronic structure calculations". In: *Solid State Commun.* 44.7 (1982), pp. 993–997. ISSN: 0038-1098. DOI: 10.1016/0038-1098(82)90320-9.

[60] J. Korringa. "Early history of multiple scattering theory for ordered systems". In: *Phys. Rep.* 238.6 (1994), pp. 341–360. DOI: 10.1016/0370-1573(94)90122-8.

[61] L. B. Rall. "Resolvent kernels of Green's function kernels and other finite-rank modifications of Fredholm and Volterra kernels". In: *J. Optimiz. Theory App.* 24.1 (Jan. 1, 1978), pp. 59–88. ISSN: 1573-2878. DOI: 10.1007/BF00933182.

[62] R. Zeller. "An elementary derivation of Lloyd's formula valid for full-potential multiple-scattering theory". In: *J. Phys.: Condens. Matter* 16.36 (2004), p. 6453. DOI: 10.1088/0953-8984/16/36/011.

[63] R. Zeller. "Projection potentials and angular momentum convergence of total energies in the full-potential Korringa–Kohn–Rostoker method". In: *J. Phys.: Condens. Matter* 25.10 (2013), p. 105505. DOI: 10.1088/0953-8984/25/10/105505.

[64] S. Achilles et al. “Nonequilibrium Green’s functions and Korringa-Kohn-Rostoker method: Open planar junctions”. In: *Phys. Rev. B* 88 (12 Sept. 2013), p. 125411. DOI: 10.1103/PhysRevB.88.125411.

[65] D. S. Fisher and P. A. Lee. “Relation between conductivity and transmission matrix”. In: *Phys. Rev. B* 23 (12 June 1981), pp. 6851–6854. DOI: 10.1103/PhysRevB.23.6851.

[66] R. Landauer. “Conductance from transmission: common sense points”. In: *Phys. Scr.* 1992.T42 (1992), p. 110. DOI: 10.1088/0031-8949/1992/T42/020.

[67] E. V. Chulkov et al. “Electronic Excitations in Metals and at Metal Surfaces”. In: *Chem. Rev.* 106.10 (2006). PMID: 17031983, pp. 4160–4206. DOI: 10.1021/cr050166o.

[68] P. Hofmann et al. “Electron–phonon coupling at surfaces and interfaces”. In: *New J. Phys.* 11.12 (2009), p. 125005. DOI: 10.1088/1367-2630/11/12/125005.

[69] C. Heiliger et al. “Implementation of a nonequilibrium Green’s function method to calculate spin-transfer torque”. In: *J. Appl. Phys.* 103.7 (2008), 07A709. DOI: 10.1063/1.2835071.

[70] J. Pollmann and S. T. Pantelides. “Scattering-theoretic approach to the electronic structure of semiconductor surfaces: The (100) surface of tetrahedral semiconductors and SiO_2”. In: *Phys. Rev. B* 18 (10 Nov. 1978), pp. 5524–5544. DOI: 10.1103/PhysRevB.18.5524.

[71] J. B. Pendry, A. B. Pretre, and B. C. H. Krutzen. “Theory of the scanning tunnelling microscope”. In: *J. Phys.: Condens. Matter* 3.24 (1991), p. 4313.

[72] T. Frederiksen. “Inelastic electron transport in nanosystems”. MA thesis. Department of Micro and Nanotechnology, Technical University of Denmark, 2004.

[73] G. D. Mahan. *Many particle physics*. 3. ed. Physics of solids and liquids. New York [u.a.], 2000. ISBN: 978-1-4419-3339-3. DOI: 10.1007/978-1-4757-5714-9.

[74] A. B. Migdal. “Interaction between electrons and lattice vibrations in a normal metal”. In: *Sov. Phys. JETP* 7 (1958), pp. 996–1001.

[75] F. Giustino. “Electron-phonon interactions from first principles”. In: *Rev. Mod. Phys.* 89 (1 Feb. 2017), p. 015003. DOI: 10.1103/RevModPhys.89.015003.

[76] C. Jacoboni. *Theory of Electron Transport in Semiconductors*. Vol. 165. Springer Series in Solid-State Sciences. Berlin: Springer, 2010. DOI: 10.1007/978-3-642-10586-9.

[77] J. M. Luttinger. “Fermi Surface and Some Simple Equilibrium Properties of a System of Interacting Fermions”. In: *Phys. Rev.* 119 (4 Aug. 1960), pp. 1153–1163. DOI: 10.1103/PhysRev.119.1153.

[78] C. Gerthsen. *Gerthsen Physik*. Ed. by D. Meschede. 23., überarb. Aufl. Springer-Lehrbuch. Berlin, Heidelberg, 2006. ISBN: 9783540254218. DOI: 10.1007/3-540-29973-4.

[79] M. T. Dove. *Introduction to Lattice Dynamics*. Cambridge Topics in Mineral Physics and Chemistry. Cambridge University Press, 1993. DOI: 10.1017/CBO9780511619885.

[80] S. Ratnowsky. "Die Zustandsgleichung einatomiger fester Körper und die Quantentheorie". In: *Ann. Phys.* 343.8 (1912), pp. 637–648. ISSN: 1521-3889. DOI: 10.1002/andp.19123430807.

[81] W. Nolting. *Grundkurs Theoretische Physik 4/2: Thermodynamik*. 9. Auflage. Springer-Lehrbuch. Berlin, Heidelberg: Springer, 2016. ISBN: 978-3-662-49033-4. DOI: 10.1007/978-3-662-49033-4.

[82] S. Narasimhan and S. de Gironcoli. "Ab initio calculation of the thermal properties of Cu: Performance of the LDA and GGA". In: *Phys. Rev. B* 65 (6 Jan. 2002), p. 064302. DOI: 10.1103/PhysRevB.65.064302.

[83] F. C. Nix and D. MacNair. "The Thermal Expansion of Pure Metals: Copper, Gold, Aluminum, Nickel, and Iron". In: *Phys. Rev.* 60 (8 Oct. 1941), pp. 597–605. DOI: 10.1103/PhysRev.60.597.

[84] P. Debye. "Zur Theorie der spezifischen Wärmen". In: *Ann. Phys.* 344.14 (1912), pp. 789–839. ISSN: 1521-3889. DOI: 10.1002/andp.19123441404.

[85] Y. Wang et al. "First-Principles Theory of Quantum Well Resonance in Double Barrier Magnetic Tunnel Junctions". In: *Phys. Rev. Lett.* 97 (8 Aug. 2006), p. 087210. DOI: 10.1103/PhysRevLett.97.087210.

[86] H. Adenstedt. "Studien zur thermischen Ausdehnung fester Stoffe in tiefer Temperatur (Cu, Ni, Fe, Zinkblende, LiF, Kalkspat, Aragonit, NH4Cl)". In: *Ann. Phys.* 418.1 (1936), pp. 69–96. ISSN: 1521-3889. DOI: 10.1002/andp.19364180105.

[87] NIST/SEMATECH. *e-Handbook of Statistical Methods*. 2012. URL: http://itl.nist.gov/div898/handbook/pmd/section6/pmd641.htm (visited on 2017).

[88] P. Hidnert and G. Dickson. "Thermal expansion of some industrial copper alloys". In: *J. Res. Nat. Bur. Stand.* 31.2 (Aug. 1943), p. 77. DOI: 10.6028/jres.031.024.

[89] M. E. Straumanis and L. S. Yu. "Lattice parameters, densities, expansion coefficients and perfection of structure of Cu and of Cu–In α phase". In: *Acta Crystallogr. A* 25.6 (1969), pp. 676–682. ISSN: 1600-5724. DOI: 10.1107/S0567739469001549.

[90] A. K. Giri and G. B. Mitra. "Extrapolated values of lattice constants of some cubic metals at absolute zero". In: *J. Phys. D: Appl. Phys.* 18.7 (1985), p. L75.

[91] J. P. Perdew, K. Burke, and M. Ernzerhof. “Generalized Gradient Approximation Made Simple”. In: *Phys. Rev. Lett.* 77 (18 Oct. 1996), pp. 3865–3868. DOI: 10.1103/PhysRevLett.77.3865.

[92] N. Troullier and J. L. Martins. “Efficient pseudopotentials for plane-wave calculations”. In: *Phys. Rev. B* 43 (3 Jan. 1991), pp. 1993–2006. DOI: 10.1103/PhysRevB.43.1993.

[93] N. Marzari et al. “Thermal Contraction and Disordering of the Al(110) Surface”. In: *Phys. Rev. Lett.* 82 (16 Apr. 1999), pp. 3296–3299. DOI: 10.1103/PhysRevLett.82.3296.

[94] E. C. Svensson, B. N. Brockhouse, and J. M. Rowe. “Crystal Dynamics of Copper”. In: *Phys. Rev.* 155 (3 Mar. 1967), pp. 619–632. DOI: 10.1103/PhysRev.155.619.

[95] A. Dal Corso, S. Baroni, and R. Resta. “Density-functional theory of the dielectric constant: Gradient-corrected calculation for silicon”. In: *Phys. Rev. B* 49 (8 Feb. 1994), pp. 5323–5328. DOI: 10.1103/PhysRevB.49.5323.

[96] F. Favot and A. Dal Corso. “Phonon dispersions: Performance of the generalized gradient approximation”. In: *Phys. Rev. B* 60 (16 Oct. 1999), pp. 11427–11431. DOI: 10.1103/PhysRevB.60.11427.

[97] Quantum ESPRESSO. *PHonon User’s Guide (v. 6.1)*. Mar. 2017. URL: http://www.quantum-espresso.org/wp-content/uploads/Doc/ph_user_guide.pdf.

[98] J. P. Perdew et al. “Restoring the Density-Gradient Expansion for Exchange in Solids and Surfaces”. In: *Phys. Rev. Lett.* 100 (13 Apr. 2008), p. 136406. DOI: 10.1103/PhysRevLett.100.136406.

[99] W. M. Haynes. *CRC handbook of chemistry and physics : a ready-reference book of chemical and physical data*. 92. ed. Boca Raton, Fla. [u.a.]: CRC Press, 2011. ISBN: 1439855110.

[100] K. O. McLean. “Low temperature thermal expansion of copper, silver, gold and aluminum”. PhD thesis. Iowa State University of Science and Technology, 1969.

[101] A. J. C. Wilson. “The thermal expansion of aluminium from 0° to 650° C”. In: *P. Phys. Soc.* 53.3 (1941), p. 235. DOI: 10.1088/0959-5309/53/3/305.

[102] C. Hartwigsen, S. Goedecker, and J. Hutter. “Relativistic separable dual-space Gaussian pseudopotentials from H to Rn”. In: *Phys. Rev. B* 58 (7 Aug. 1998), pp. 3641–3662. DOI: 10.1103/PhysRevB.58.3641.

[103] S. Goedecker, M. Teter, and J. Hutter. “Separable dual-space Gaussian pseudopotentials”. In: *Phys. Rev. B* 54 (3 July 1996), pp. 1703–1710. DOI: 10.1103/PhysRevB.54.1703.

[104] J. P. Perdew and A. Zunger. “Self-interaction correction to density-functional approximations for many-electron systems”. In: *Phys. Rev. B* 23 (10 May 1981), pp. 5048–5079. DOI: 10.1103/PhysRevB.23.5048.

[105] M. Methfessel and A. T. Paxton. “High-precision sampling for Brillouin-zone integration in metals”. In: *Phys. Rev. B* 40 (6 Aug. 1989), pp. 3616–3621. DOI: 10.1103/PhysRevB.40.3616.

[106] J. R. Yates et al. “Spectral and Fermi surface properties from Wannier interpolation”. In: *Phys. Rev. B* 75 (19 May 2007), p. 195121. DOI: 10.1103/PhysRevB.75.195121.

[107] R. Stedman and G. Nilsson. “Dispersion Relations for Phonons in Aluminum at 80 and 300°K”. In: *Phys. Rev.* 145 (2 May 1966), pp. 492–500. DOI: 10.1103/PhysRev.145.492.

[108] M. Kresch et al. “Phonons in aluminum at high temperatures studied by inelastic neutron scattering”. In: *Phys. Rev. B* 77 (2 Jan. 2008), p. 024301. DOI: 10.1103/PhysRevB.77.024301.

[109] G. X. Miao et al. “Disturbance of Tunneling Coherence by Oxygen Vacancy in Epitaxial Fe/MgO/Fe Magnetic Tunnel Junctions”. In: *Phys. Rev. Lett.* 100 (24 June 2008), p. 246803. DOI: 10.1103/PhysRevLett.100.246803.

[110] C. Heiliger et al. “Influence of the interface structure on the bias dependence of tunneling magnetoresistance”. In: *Phys. Rev. B* 72 (18 Nov. 2005), p. 180406. DOI: 10.1103/PhysRevB.72.180406.

[111] C. Heiliger et al. “Interface structure and bias dependence of Fe/MgO/Fe tunnel junctions: Ab initio calculations”. In: *Phys. Rev. B* 73 (21 June 2006), p. 214441. DOI: 10.1103/PhysRevB.73.214441.

[112] M. Czerner. Private communication. 2017.

[113] H. L. Meyerheim et al. “Surface x-ray diffraction analysis of the MgO/Fe(001) interface: Evidence for an FeO layer”. In: *Phys. Rev. B* 65 (14 Apr. 2002), p. 144433. DOI: 10.1103/PhysRevB.65.144433.

[114] C. Heiliger. “Elektronentransport durch planare Tunnelkontakte: Eine *ab initio* Beschreibung”. PhD thesis. Naturwissenschaftlichen Fakultät II - Chemie und Physik, Martin-Luther-Universität Halle-Wittenberg, 2007.

[115] S. H. Vosko, L. Wilk, and M. Nusair. “Accurate spin-dependent electron liquid correlation energies for local spin density calculations: a critical analysis”. In: *Can. J. Phys.* 58.8 (1980), pp. 1200–1211. DOI: 10.1139/p80-159. eprint: https://doi.org/10.1139/p80-159.

[116] W. H. Butler et al. “Spin-dependent tunneling conductance of Fe|MgO|Fe sandwiches”. In: *Phys. Rev. B* 63 (5 Jan. 2001), p. 054416. DOI: 10.1103/PhysRevB.63.054416.

[117] C. Heiliger, P. Zahn, and I. Mertig. “Microscopic origin of magnetoresistance”. In: *Mater. Today* 9.11 (2006), pp. 46–54. ISSN: 1369-7021. DOI: https://doi.org/10.1016/S1369-7021(06)71694-7.

[118] C. Caroli et al. “A direct calculation of the tunnelling current: IV. Electron-phonon interaction effects”. In: *J. Phys. C: Solid State Phys.* 5.1 (1972), p. 21.

[119] P. Hyldgaard et al. “Resonant Tunneling with an Electron-Phonon Interaction”. In: *Ann. Phys.* 236.1 (1994), pp. 1–42. ISSN: 0003-4916. DOI: https://doi.org/10.1006/aphy.1994.1106.

[120] A. Fabian. Private communication. 2017.

[121] M. Abramowitz and I. A. Stegun. *Handbook of Mathematical Functions: With Formulas, Graphs, and Mathematical Tables*. Tenth Printing. Vol. 55. Applied Mathematics Series. National Bureau of Standards, 1964.

[122] A. R. Edmonds. *Angular Momentum in Quantum Mechanics*. Investigations in Physics. Princeton, NJ: Princeton University Press, 2016. ISBN: 9781400884186. DOI: 10.1515/9781400884186.

[123] P. Mavropoulos and N. Papanikolaou. “The Korringa-Kohn-Rostoker (KKR) Green Function Method I. Electronic Structure of Periodic Systems”. In: *Computational Nanoscience: Do It Yourself!* Ed. by J. Grotendorst, S. Blügel, and D. Marx. Vol. 31. NIC Series. Jülich: John von Neumann Institute for Computing, 2006.

List of Publications

[124] C. E. Mahr, M. Czerner, and C. Heiliger. “Implementation of a method for calculating temperature-dependent resistivities in the KKR formalism”. In: *Phys. Rev. B* 96 (16 Oct. 2017), p. 165121. DOI: 10.1103/PhysRevB.96.165121.

Acknowledgements

> As we express our gratitude, we must never forget that the highest appreciation is not to utter words, but to live by them.
>
> John F. Kennedy

I would like to express my very great appreciation to my advisor Prof. Dr. Christian Heiliger for allowing me to self-reliantly work on this interesting and challenging subject, thereby demonstrating considerable confidence in my capabilities. Simultaneously, his readiness for technical discussions made it feasible to profit from his outstanding intuition and vast knowledge regarding theoretical condensed matter physics and beyond. Besides, I am grateful for being given the facility to attend many (international) conferences.

I also wish to thank Prof. Dr. Simone Sanna for his interest in my work as well as for providing the second report on this thesis. Further, although not too long since he reinforced the solid state section of the theory department, I acknowledge numerous stimulating and intriguing conversations.

Moreover, my sincere thanks are extended to many former and present members of the Institut für Theoretische Physik and the I. Physikalische Institut for the welcoming atmosphere. I am particularly indepted to: Dr. Marcel Giar, not only for sharing his expertise regarding symmetry operations but also for a multitude of technical and non-technical exchanges; Dr. Michael Czerner for providing the Gießen KKR code as well as a solid introduction to its mode of operation; Dr. Christian Franz for his help in the initial stage of this work, especially for commenting on implementational details of the NEGF formalism in the Gießen KKR code; Dr. Stefano Mattiello for frequent inspiring mathematical discussions; Dr. Andreas Rühl and the IPI band for many harmonic distractions.

I further appreciate the proficient management of the required computing facilities by the HPC administration team (Dr. Michael Czerner, Dr. Michael Feldmann and Dr. Marcel Giar), as well as the smooth handling of all the bureaucratic necessities by the administrative-technical staff of both the Institut für Theoretische Physik and the I. Physikalische Institut.

Finally, I am exceedingly grateful to my parents and brother for everlasting support, both emotional and technical. Your constant and candid encouragement are the foundations for the completion of this work.

Eidesstattliche Erklärung

Gemäß § 17 Absatz 2 Punkt 2 der Promotionsordnung der Naturwissenschaftlichen Fachbereiche der Justus-Liebig-Universität Gießen in der Fassung vom 21.01.2016

Ich erkläre:

Ich habe die vorgelegte Dissertation selbstständig und ohne unerlaubte fremde Hilfe und nur mit den Hilfen angefertigt, die ich in der Dissertation angegeben habe. Alle Textstellen, die wörtlich oder sinngemäß aus veröffentlichten Schriften entnommen sind, und alle Angaben, die auf mündlichen Auskünften beruhen, sind als solche kenntlich gemacht. Ich stimme einer evtl. Überprüfung meiner Dissertation durch eine Antiplagiat-Software zu. Bei den von mir durchgeführten und in der Dissertation erwähnten Untersuchungen habe ich die Grundsätze guter wissenschaftlicher Praxis, wie sie in der „Satzung der Justus-Liebig-Universität Gießen zur Sicherung guter wissenschaftlicher Praxis“ niedergelegt sind, eingehalten.

Gießen, den 16.2.2018

Carsten E. Mahr